Composites Science and Technology 70 (2010) 1080–1088

Contents lists available at ScienceDirect

Composites Science and Technology

journal homepage: www.elsevier.com/locate/compscitech

Dielectric properties of chiral honeycombs – Modelling and experiment

Pawel Kopyt [a,*], Radu Damian [b], Malgorzata Celuch [c], Romeo Ciobanu [b]

[a] Institute of Radioelectronics, Warsaw University of Technology, ul. Nowowiejska 15/19, 00-665 Warsaw, Poland
[b] Technical University of Iasi, Facultatea de Electronica si Telecomunicatii, Bd. Carol I nr. 11, Iasi 700506, Romania
[c] QWED Sp. z o.o., ul. Nowowiejska 28/32, 02-010 Warsaw, Poland

ARTICLE INFO

Article history:
Received 12 November 2008
Received in revised form 17 August 2009
Accepted 21 August 2009
Available online 19 September 2009

Keywords:
A. Smart materials
B. Electrical properties
Hexa-chiral honeycomb

ABSTRACT

Electromagnetic properties of mechanically chiral honeycomb structures are investigated. In extension to previous works on the subject, rigorous analysis is performed above the quasi-static frequency range. Theoretical considerations and full wave 3D electromagnetic simulations are conducted to prove that, for the honeycombs of interest, higher order harmonics due to structure periodicity are attenuated away from the panel surface at frequencies up to several GHz, which covers a number of popular ISM bands. As a consequence, only individual plane TEM waves are observable at practical locations of transmitters and receivers away from the panel. Under the same conditions, it is demonstrated that the structural chirality does not translate into chiral electromagnetic behaviour. In other words, orthogonal modes of the honeycomb scenarios are linearly polarised, and transformation of the electromagnetic energy into heat occurs purely as a result of classical conductivity or loss tangent, which are low for the low-density panels made of low-loss dielectric cores. This indicates that EMC or shielding characteristics can only be designed either by utilizing the phenomenon of wave reflections, or by equipping the panels with additional foils on surfaces or absorbing foams in air volumes. While precise measurements of final-sized honeycomb panels remain as a challenging task for further work, preliminary experiments have been performed showing good agreement with theoretical and computed predictions.

1. Introduction

Honeycomb cores have become a widespread structural feature in aerospace, naval, and packaging applications. Regular centresymmetric hexagonal honeycombs behave mechanically with a positive Poisson's ratio characteristic – they contract laterally when pulled along one direction. Of special interest are, however, auxetic honeycombs, which expand in all directions when pulled in only one. The family of auxetic honeycombs includes re-entrant centresymmetric structures [1] as well as chiral structures, proposed for the first time by Wojciechowski and Branka [2] and, as structural concept, by Prall and Lakes [3]. Chiral honeycombs will be a focus of this paper. By definition, an object is *chiral* if it cannot be brought into congruence with its mirror image by translation or rotation. The implications of chirality in terms of mechanical properties of chiral honeycombs have been investigated in the literature. It has been shown that they feature enhanced compressive strength capabilities [4] and shear stiffness compared to classical centresymmetric honeycomb configurations for the same relative density [5]. The auxetic behaviour also leads to a sinclastic curvature feature, which is extremely useful in manufacturing curved sandwich shells in radome applications [6,7].

Nowadays, multi functionality is a keyword for design engineers. Of particular interest are innovative devices that incorporate pre-defined mechanical and electromagnetic properties. They allow reducing numbers of components, and hence weight and energy consumption. Such multifunctional designs with honeycombs require that their electromagnetic properties be understood in as much depth as the mechanical properties are. To this end, dielectric properties of both re-entrant [8,9] and chiral [10] honeycombs have been previously addressed in the literature, using analytical Hashin–Shriktman models [8–10] and numerical quasi-static finite-difference solutions [10]. The underlying assumption in these works has been that, from the viewpoint of electromagnetic properties, the inhomogeneous honeycomb panels can be approximated by artificially homogenised dielectrics. While this assumption is natural in the DC limit considered therein, its extension to higher frequencies, and to the ISM bands in particular, may arise controversies. This restricts the reliability of the developed results for practical microwave and EMC designs. Furthermore, the surrogate models have been assumed in-plane isotropic in [8,9]; in [10], the in-plane anisotropy has been allowed for, but the two differentiated solutions have been stiffly set as the vertical and horizontal electric fields with reference to Fig. 1a. To be assured that the calculated effective permittivities remain (strictly or approximately) valid at higher frequencies, it needs to be shown that the two linearly polarised waves remain eigenmodes of the

* Corresponding author. Tel.: +48 22 234 58 29.
E-mail address: pkopyt@elka.pw.edu.pl (P. Kopyt).

0266-3538/$ - see front matter © 2009 Elsevier Ltd. All rights reserved.
doi:10.1016/j.compscitech.2009.08.017

(a)

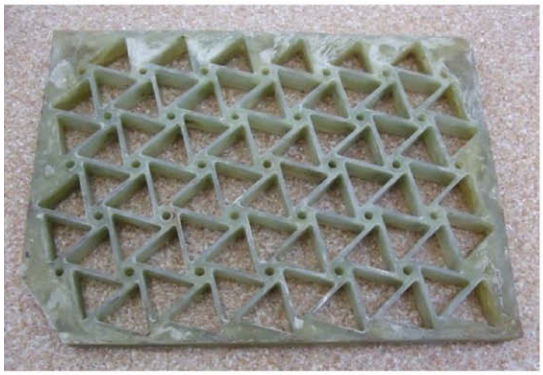

(b)

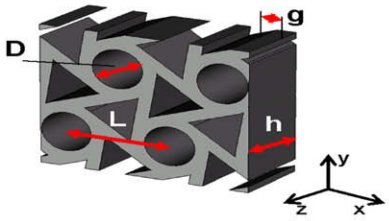

Parameter	Sample 1	Sample 2
D	11.98	7.64
h	19.75	26.73
L	24.72	52.18
g	3.3	3.37
ε_r	2.5	5.23
tgδ	0	0.021 (@100MHz)

Fig. 1. Chiral structures considered: (a) photography of panel "Sample 2" and (b) dimensions of both considered panels.

mechanically chiral structures. Note that if electromagnetic chirality occurs, the eigenmodes become circularly polarised [11].

The above assumptions of effective homogeneity and linearly polarised eigenmodes will be re-visited in the present paper by means of field-theoretical considerations and full wave three-dimensional (3D) numerical electromagnetic analysis. For increased confidence, two commercial electromagnetic software packages will be independently used by the two groups involved in this work: CST Microwave Studio [12] at the Technical University IASI, and QuickWave-3D [13] at the Warsaw University of Technology and QWED. A major result, with respect to the previous quasi-static considerations [8–10], consists in deriving a frequency limit up to which chiral honeycombs can be approximated by artificial homogenised dielectrics. It will also be shown that, up to the above frequency limit, no electromagnetic chirality effects are observed in the structurally chiral honeycomb panels. Finally, the simulated results are confirmed by laboratory measurements. These results enhance the reliability of the previously provided quasi-static permittivity calculations, extend them to higher frequencies over several ISM bands, and hence create a sound basis for further designs of chiral honeycombs of pre-defined microwave characteristics.

2. Two structures considered and theoretical considerations

Two chiral structures have been considered in this work. Both panels are hexa-chiral honeycombs consisting of equally spaced cylinders connected to six neighbours with ligaments. The two structures differ in terms of permittivity of the core material as well as the dimensions of their geometrical features. These basic differences further differentiate their behaviour as a function of frequency and, in particular, they affect the threshold frequency above which a given structure cannot be considered as a homogeneous dielectric, as will be demonstrated further. The panel "Sample 1" has been made of low-permittivity polymer with low structural density, while "Sample 2" (shown in Fig. 1a) is based on a higher-permittivity fiber-reinforced polymer of higher structural density. Both panels have been manufactured by Italcompany in the framework of the CHISMACOMB project. The dimensions and the core material EM-properties of the two structures are presented in Fig. 1b.

Two structural characteristics of the panels are visible in Fig. 1: they are *periodic* with overall spatial period L, and they are geometrically *chiral* in the sense explained in Section 1. From the electromagnetic viewpoint, structural *periodicity* is known to lead to higher space harmonics or diffraction rays, which require different methodologies of analysis and design than the simpler case of homogenised panels. Electromagnetic *chirality* is also a phenomenon explored in the literature, entailing that fundamental modes of the structure are circularly polarised waves. Before embarking on the numerical and experimental study, we shall consider whether these phenomena should be accounted for in the case of chiral honeycombs of interest herein.

Consider a plane wave incident onto a periodic panel of period L (as e.g. in Fig. 1) at angle θ_{in} defined with respect to the normal to the slab surface. Except for the fundamental ray at θ_{in}, dictated by Snell's law, the reflected and transmitted fields also comprise an infinite series of higher order harmonics due to structure periodicity, at angles θ_m, $m = 1, 2, \ldots$, derived from Floquet theorem [14–16]:

$$\beta_0 \sin(\theta_m) = \beta_0 \sin(\theta_{in}) \pm \frac{2m\pi}{L} \tag{1}$$

where β_0 is phase constant in free space. Each of these higher rays propagates away from the periodic surface with perpendicular component of the phase constant $\beta_{m\perp}$ given by:

$$\beta_{m\perp} = \beta_0 \cos(\theta_m) \tag{2}$$

where $\cos(\theta_m)$ is formally defined through the trigonometric identity:

$$\cos(\theta_m) = \pm\sqrt{1 - \sin^2(\theta_m)} \tag{3}$$

Re-writing Eq. (1) as:

$$\sin(\theta_m) = \sin(\theta_{in}) \pm \frac{m\lambda}{L} = \sin(\theta_{in}) \pm \frac{mc}{fL} \tag{4}$$

where λ is free space wavelength and c is the speed of light, one realises that higher harmonics have imaginary perpendicular phase constant. This entails that they are generated at the periodic surface to satisfy the boundary conditions, but attenuated away from the slab. In the case of normal incidence and low frequencies such that $\lambda > L$, only the fundamental ray propagates with real phase shift in the perpendicular direction, and is therefore detectable away from the panel. For oblique incidence, the frequency condition relaxes

to $\lambda > 2L$. The homogenisation limit for periodic structures often formulated by the rule-of-thumb [17]:

$$L < 0.25\lambda \tag{5}$$

is therefore conservative. It ensures that all higher harmonics are effectively attenuated away from the honeycomb and only a plane TEM wave at Snell's angle exists at practical transmitter/receiver locations.

Consider now the issue of electromagnetic chirality. Chiral materials are understood as bi-isotropic ones [11]:

$$\begin{aligned} \boldsymbol{D} &= \varepsilon_c \boldsymbol{E} + \mathrm{j}\xi_c \boldsymbol{B} \\ \boldsymbol{H} &= \mathrm{j}\xi_c \boldsymbol{E} + \boldsymbol{B}/\mu_c \end{aligned} \tag{6}$$

where ε_c and μ_c represent equivalents of the classical permittivity and permeability, and ξ_c the chirality admittance, which is a measure of the handedness of the medium; bold italics denote vector variables, italics – scalar variables, and j is the imaginary unit.

If a linearly polarised plane wave is incident into a chiral medium, it decomposes into two circularly polarised modes propagating with different wavelengths and undergoing different levels of attenuation. Full wave numerical solutions of the following section show that this is not the case for the structurally chiral honeycombs.

3. Numerical models and simulation results

The complexity of the analysed structures makes the analysis of their electromagnetic properties with analytic methods a task of prohibitive complexity. For this reason a numerical approach has been chosen to theoretically investigate the presented structures as a function of incident wave frequency. In order to streamline the research, two commercial EM analysis packages have been selected: Microwave Studio by CST [12], and QuickWave-3D by QWED [13]. Both tools are based on the finite differences time domain (FDTD) method, which is particularly well suited for analysis of EM problems in a wide frequency band. The FDTD kernels of Microwave Studio and QuickWave-3D have reached maturity long ago and their validation is not a subject of the present paper. On the other hand, there are conceptual differences between Microwave Studio and QuickWave-3D at the stages of numerical mesh generation, modelling of input/output ports, and extraction of frequency domain scattering parameters. It is therefore relevant and appropriate to apply the two tools in order to ensure that the computational models of honeycomb structures are constructed and meshed correctly. Moreover, cross-validation of the results obtained by the two research groups working independently and using different software packages is a safeguard against human mistakes. In all simulations, normal incidence of a plane wave is considered.

3.1. QuickWave-3D models

Since the panels are periodic structures, for a complete analysis of their behaviour only one period needs to be modelled and discretised. Such an approach radically reduces computer resources required to complete an analysis as well as greatly increases the computational speed due to smaller size of the problem as compared to modelling larger panels. Perfect electric conductor (PEC) conditions are set along vertical boundaries in Fig. 2 and perfect magnetic conductors (PMC) along the horizontal ones. Such boundary conditions are natural for the normally incident plane wave of horizontal polarisation. If higher harmonics due to structural periodicity are excited, they will be supported as in a rectangular waveguide.

The discretised models of both structures prepared in the QuickWave-3D environment are presented in Fig. 2. For the *S*-parameter analysis of the finite thickness panel, the input and output ports have been placed in a distance of 15 mm from the structure; in case of propagation constant and the wave impedance extraction, the reference plane has been placed along the front side of the panel. The uniform discretisation assumed in both cases has been selected so that the size of one cell is smaller than one tenth of the wavelength at the highest analysed frequency (15 GHz) in the base medium of "Sample 2" panel. This is well in excess to the practical requirements as the base medium takes up only a small fraction of the panel volume. However, it ensures good resolution of the geometry and additionally suppresses the numerical dispersion error. Taking into account the limited size of the analysed structures, this meshing still leads to short computation times within a minute.

3.2. Microwave Studio models

The Microwave Studio model has been constructed according to the guidelines for convergence/computation speed/accuracy compromise presented in [12]. A convergence study has been performed with the frequency domain solver used to collect reference results. This approach allowed arriving at discretisation, which ensures reasonable accuracy of the time-domain solver while radically reducing the computation time (5 min per one simulation versus over 2 days in case of the frequency domain solver).

In the model employed in the *S*-parameter analysis, the input port was placed at a distance equal to the minimum between the 8th part of the wavelength and five mesh lines from the structure, the second (output) wave port is added only when losses inside the structure were taken into account.

4. Simulation results

First, the interaction between a plane wave and an infinitely large sheet of auxetic material was investigated. Proper boundary

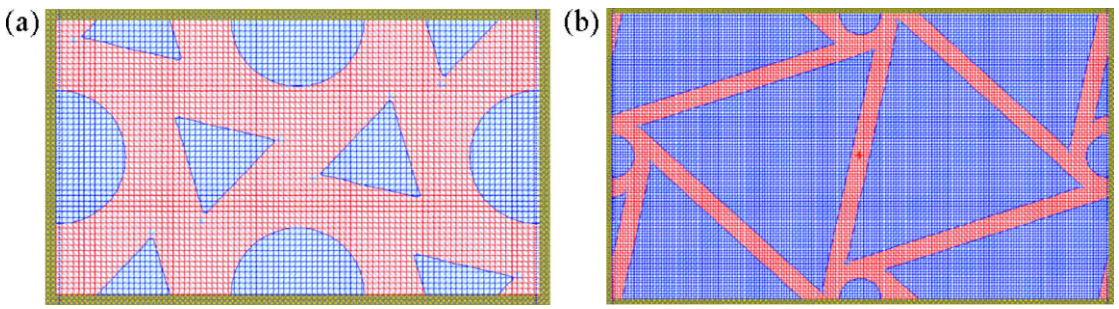

Fig. 2. Models of the panels in QuickWave-3D: (a) one period of the panel "Sample 1" and (b) one period of the panel "Sample 2".

conditions were applied at walls parallel to the x-axis (electric walls), and walls parallel to the y-axis (magnetic wall). In case of the Microwave Studio model preparation, the report [17] has been used as a reference. For both computational environments (Microwave Studio and QuickWave-3D) the EM-fields inside the structure have been inspected, as shown in Figs. 5–7.

The two numerical models have been employed to perform parametric studies needed for an investigation into the effects resulting from modifying selected dimensions of the panel. The results obtained in all cases have been shown in Fig. 3. In case of panel "Sample 1" the panel thickness (h) and the ligament thickness (g) have been selected. As shown, a very good agreement has been achieved between the Microwave Studio and QuickWave-3D based models, which cross-validates performed calculations. The obtained S_{11} characteristics suggest that the panel acts like a sheet of homogeneous medium exhibiting properties of a half-wavelength transformer. In other words, it acts like a dielectric layer of permittivity chosen so that a wave of wavelength twice longer than the layer thickness does not reflect from the panel, but all the wave's energy passes through it. Only at higher frequencies this behaviour is obscured by effects resulting from the panel inhomogeneity, as expected based on Eq. (4). Particularly at lower frequencies it is clear that the effective permittivity of the panel (treated like a homogeneous structure) depends strongly on its geometrical features, or structural density. This explains the obtained results. The half-wavelength transformer behaviour occurs at different frequencies when the ligament thickness (and effective permittivity) is changed. The same effect is visible when the panel thickness is modified. Although in this case its effective permittivity remains fixed, the transformer thickness changes detunning the effect to different frequencies.

In case of the panel "Sample 2" only the panel thickness has been considered in the investigation. Due to the large inhomogeneity of this structure resulting from the higher permittivity of the base medium, the reflection curves are much more difficult to interpretate as compared to the "Sample 1" panel. Based on the curves shown in Fig. 4a and b, it becomes obvious that a more in-depth analysis of the auxetic medium itself is required in order to investigate the nature of the effects occurring at larger frequencies and to verify that they have a source in high inhomogeneity of the structure, and not in its chirality in the electromagnetic sense as presented in Section 1. Also in this case the agreement between results obtained with two different computational tools indicates correctness of the prepared models and is a sign that the analysis

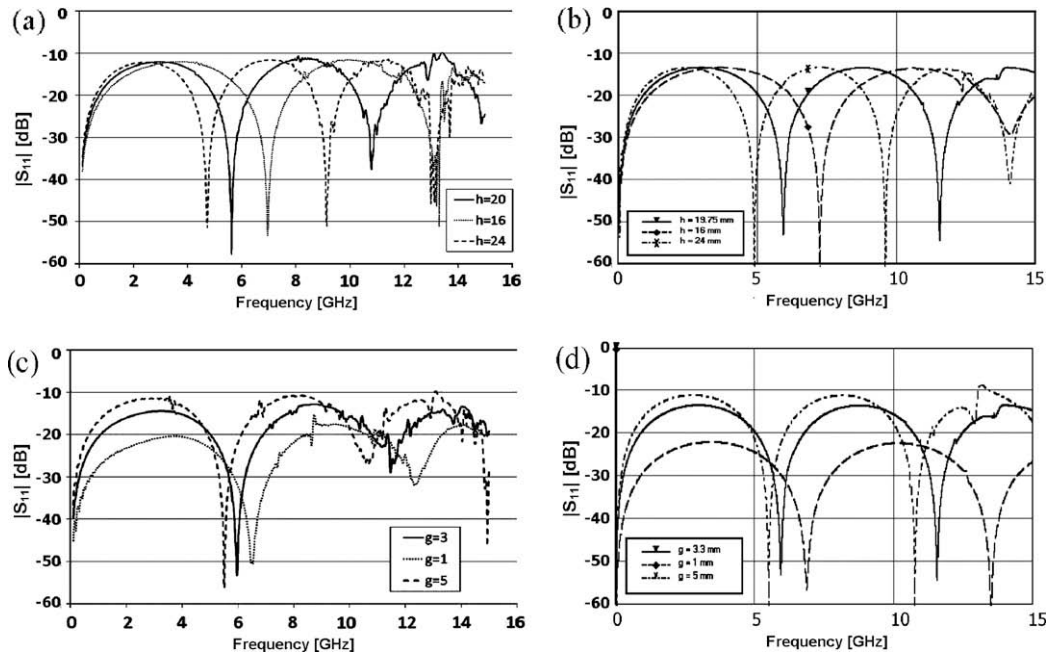

Fig. 3. EM wave reflections (the S_{11} coefficient) from the panel "Sample 1" obtained with the Microwave Studio (a, c) and QucikWave-3D (b, d) numerical models: (a, b) for varying panel thickness and (c, d) for varying ligament thickness.

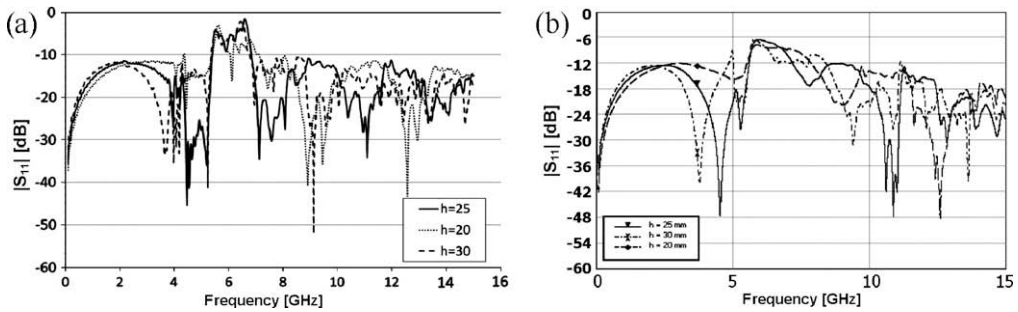

Fig. 4. EM wave reflections (the S_{11} coefficient) from the panel "Sample 2" obtained for varying panel thickness: (a) using the Microwave Studio model and (b) using the QucikWave-3D model.

presented further in this section using only the QuickWave-3D model is clear of numerics-related errors.

In order to closer investigate the electromagnetic effects occurring in the two presented panels, the amplitudes of the electric (E) and magnetic (H) fields have been obtained using the QuickWave-3D model. For each structure, two sinusoidal excitations have been considered based on the previous results. A low frequency (1 GHz) lies in the band where the panels exhibit properties of a homogeneous structure while at a high frequency (7.5 GHz) it is expected that the inhomogeneity of the sheets will become visible. The obtained distributions have been shown in Figs. 5–8. As expected, at lower frequency both panels behave as if made of a homogeneous material, with a proper TEM wave propagating through the structures. Although the E_y-field amplitude does not remain constant across the panel cross-section, it is only a result of changes in the permittivity values. The H_x-field amplitude distribution proves that the propagating wave is plane. Additionally, no longitudinal field components have been excited (not shown). The situation changes at the higher frequency, where not only the TEM wave propagates in the panels, but also higher modes are excited changing the magnetic field distribution. As expected, this effect becomes much more pronounced in case of the panel "Sample 2", which agrees with the observations made while analysing the reflection curves. The existence of the higher modes in the structure clearly shows that at higher frequencies the medium can no longer be treated as a homogeneous one.

The qualitative observations made based on the EM-fields distributions presented previously can be quantitatively confirmed through the powerful system of S-parameter extraction implemented in QuickWave-3D after [18]. The panel is analysed as it is, and also as a homogeneous medium in a broader frequency band. Such an approach concentrates on the medium properties in order to verify the requirement (5). For a TEM wave propagating through a homogenous medium the following condition is fulfilled:

$$\gamma Z = j\omega\mu_0, \tag{7}$$

where γ is the propagation constant of EM wave in the medium, Z is the wave impedance (equal to the medium intrinsic impedance for the TEM wave), ω is angular frequency of the wave, while μ_0 is permeability of vacuum.

Checking the validity of Eq. (7) for a given scenario allows establishing at which frequencies the medium is still effectively homogeneous and the EM energy propagates in it as a TEM wave.

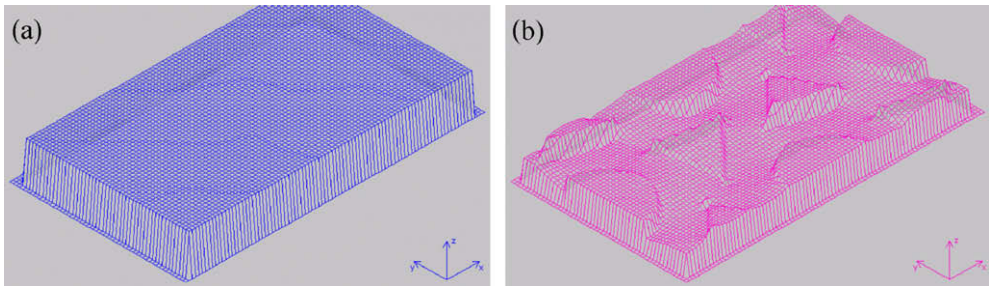

Fig. 5. EM-field distribution in the *XY* cross-sections through the panel "Sample 1" in the middle of its height at 1 GHz: (a) H_x-field amplitude distribution and (b) E_y-field amplitude distribution.

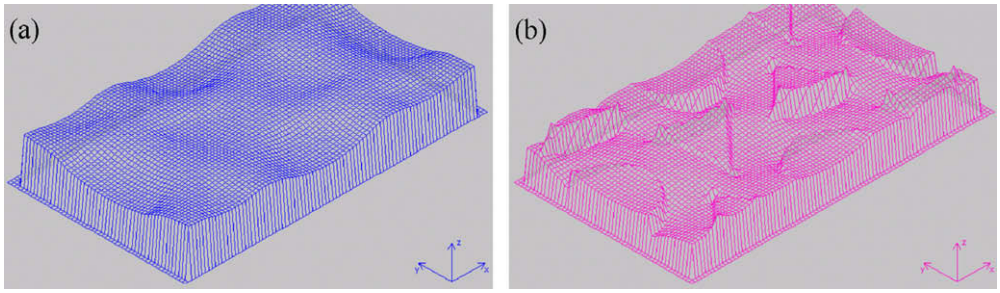

Fig. 6. EM-field distribution in the *XY* cross-sections through the panel "Sample 1" in the middle of its height at 7.5 GHz: (a) H_x-field amplitude distribution and (b) E_y-field amplitude distribution.

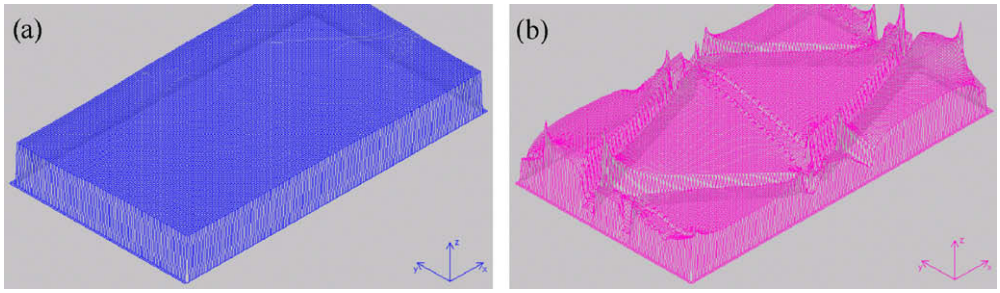

Fig. 7. EM-field distribution in the *XY* cross-sections through the panel "Sample 2" in the middle of its height at 1 GHz: (a) H_x-field amplitude distribution and (b) E_y-field amplitude distribution.

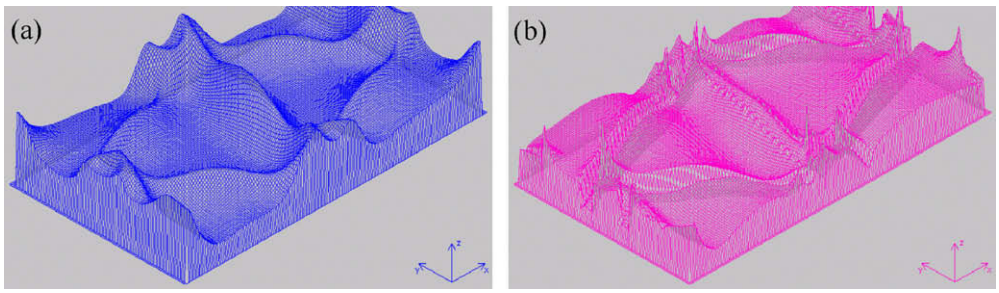

Fig. 8. EM-field distribution in the *XY* cross-sections through the panel "Sample 2" in the middle of its height at 7.5 GHz: (a) H_x-field amplitude distribution and (b) E_y-field amplitude distribution.

Using the QuickWave-3D model of the two panels, the propagation constant and medium impedance have been calculated in a broad frequency band. The curves resulting from multiplying of these numerically-obtained data have been shown in Fig. 9. As a reference, the $j\omega\mu_0$ line has been added in order to better show the frequency band where both panels are still homogeneous. The results confirm the previous observations. The frequency band where the panel "Sample 1" remains homogeneous is wider than a corresponding band for the panel "Sample 2". It has been shown, however, that for frequencies higher than 5 GHz the homogeneity of both panels slowly degradates. Power balance relation after [18] has also been extracted, giving a flat unity over the frequency band ensuring homogenised behaviour. This confirms that a linearly polarised wave remains an eigenmode, and the only propagating wave, of the structurally periodic and chiral panel.

Using the data presented in Fig. 9 one can verify the condition (5) calculated based on the structure dimensions shown in Fig. 1 together with effective permitivitties of the panels in the quasi-static case (1.8 and 1.6 respectively). In case of the panel "Sample 1", the threshold frequency is 2.3 GHz, while for the panel "Sample 2" this value is 1.1 GHz. Thus, it seems that the condition is a very conservative estimate, and can be successfully relaxed by the factor of 2. However, as shown, it provides a valuable and easy-to-obtain measure of homogeneity of a given medium.

To conclude the research into EM-properties of the hexa-chiral panel treated as homogeneous structure, its effective permittivity and the loss tangent has been extracted based on the amplitude and phase of the transmission coefficient S_{21} curve. To this end, the wave propagation in the panel medium has been analysed. The effective permittivity of the panel "Sample 2" has been shown in Fig. 10a and b shows the loss tangent obtained for the same structure. The effective permittivity is a well-defined parameter only for the TEM propagation. As already shown, for higher frequencies also higher modes can be excited in the structure, which makes the use of the effective permittivity term inappropriate. For this reason the frequency band of interest has been in this case limited to 4 GHz only.

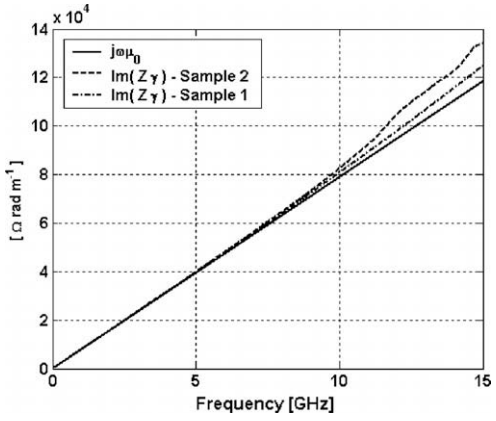

Fig. 9. Results of the homogeneity test for both panels based on Eq. (1).

The extraction process in which EM-properties of the panel medium have been obtained, has been verified in a simple numerical experiment. First, the transmission coefficient of the panel "Sample 2" has been calculated using the QuickWave-3D model where the input and output ports are located in a distance from the panel itself. Next, a similar 3-layer system has been built, but the panel has been replaced by a solid block made of medium of properties chosen using the curves shown in Fig. 10a and b, while maintaining the original thickness. As a working frequency 1 GHz has been selected leading to the following properties of the dielectric block: $\varepsilon_r = 1.60$, and $\sigma = 7 \times 10^{-4}$. The resulting curves have been presented in Fig. 11a and b shows the error between the two S_{21} curves in the vicinity of 1 GHz.

As shown, at the frequency at which the EM-properties of the solid block have been calculated, the two curves are well matched. In order to obtain a similar match at different frequencies, the solid block permittivity and its electric losses must be recalculated accordingly. The results further confirm that the panel medium can be treated as homogeneous under the condition that the working frequency is low enough. However, at frequencies above the TEM threshold, no EM-properties of the solid block can be found.

We can conclude that hexa-chiral panel for frequencies ensuring pure TEM wave propagation behaves as a homogenous dielectric, with its effective electrical permittivity being a function of frequency as shown in Fig. 10a. Thus, different methods to increase the microwave shielding capability must be applied in order to obtain an EMC capable material. In this respect, insertion of FSS or inclusion of the panels in Salisbury screen configuration could seem to be viable possibilities. For the measurement section of this paper we will focus on a simpler configuration, which consists in the deposition of two aluminum foils on both sides of the panel. The selected method has the advantage to have a minimal influence over the mechanical properties of the panel (which are a key element in the CHISMACOMB Project).

5. Transmission measurements

Available measurement equipment limits our measurement set-up. The coaxial holder method (a small sample of the material inserted in a waveguide) is potentially very accurate and less susceptible to measurement environment influences but the dimensional characteristics of our samples make this method impossible to use. Namely, at high frequencies, the waveguide and sample dimensions should be extremely low compared to the physical cell size of the chiral panel we would test. A WR 770 waveguide would be necessary, and even then the very low frequency bandwidth of such a device will render measurements

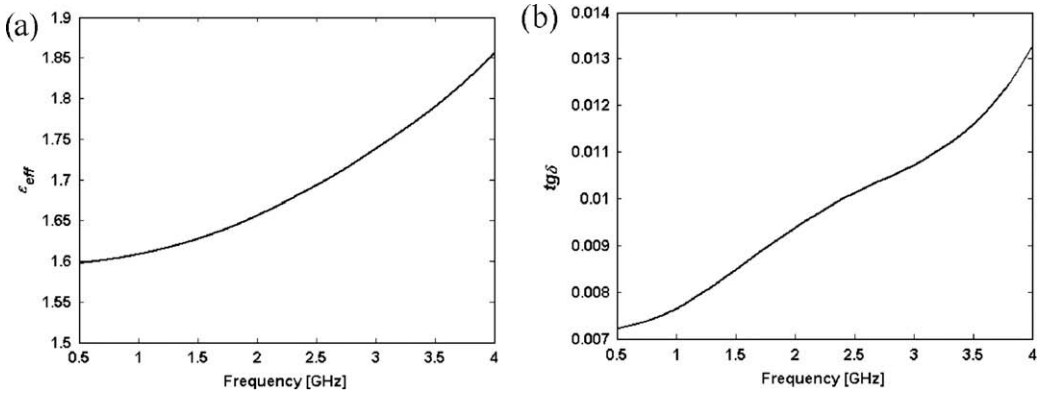

Fig. 10. The EM-properties of panel "Sample 2" treated as a homogeneous structure calculated for the normal incidence scenario: (a) effective permittivity and (b) loss tangent.

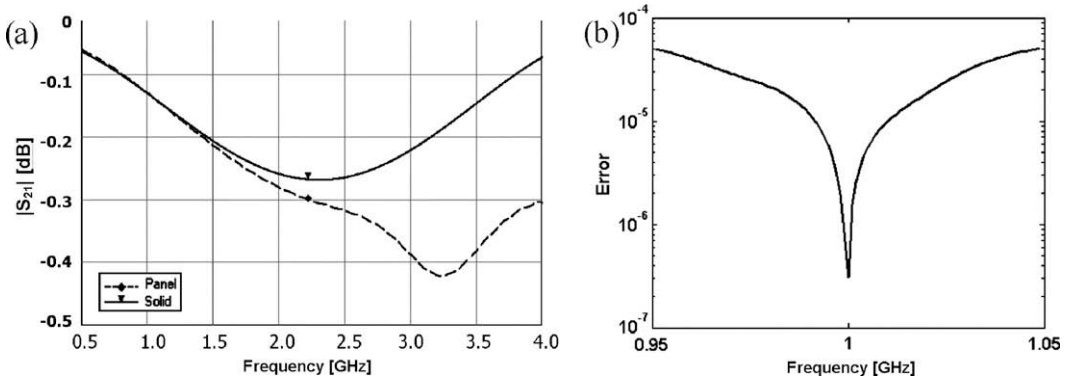

Fig. 11. The transmission coefficient of two 3-layer systems built using either the panel "Sample 2" or a solid block with matched EM-properties: (a) the S_{21} amplitude of the two systems and (b) error between the two curves in the vicinity of working frequency.

useless. For these reasons, free space transmission measurement method (Fig. 12a) has been selected. Measurements were performed with the panel "Sample 2" placed between the transmitting and receiving antennae. The equipment used includes: Agilent E8257 PSG Analog Signal Generator (frequency domain: 250 kHz to 40 GHz), Agilent E7405A EMC spectrum analyzer, (frequency domain: 9 kHz to 26.5 GHz), ETS Lindgren 3115 Horn antennas, (frequency domain: 1–18 GHz).

Errors due to diffractions are inevitable in this case because the size of the manufactured prototypes is only 37 × 28 cm. In order to minimize them, the antennas should face each other and the distance between them should not be large in order to ensure that the transmitted signals pass through the sample. However this would require that a "near field" measurement set-up and instruments are employed. This led to a non-ideal placement of the antennas facing each other at a distance of 23 cm, as a compromise between the two conflicting conditions. This setting ensures that more than half of the emitter power passes through the sample (HPM-half power beam width of the antennas being available in the datasheets for computations) while minimizing near field

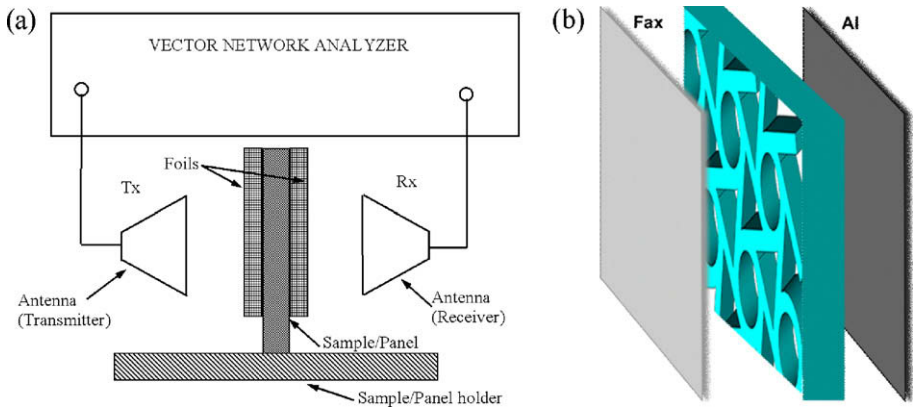

Fig. 12. (a) Free-space transmission measurement method and (b) Salisbury Screen with chiral core.

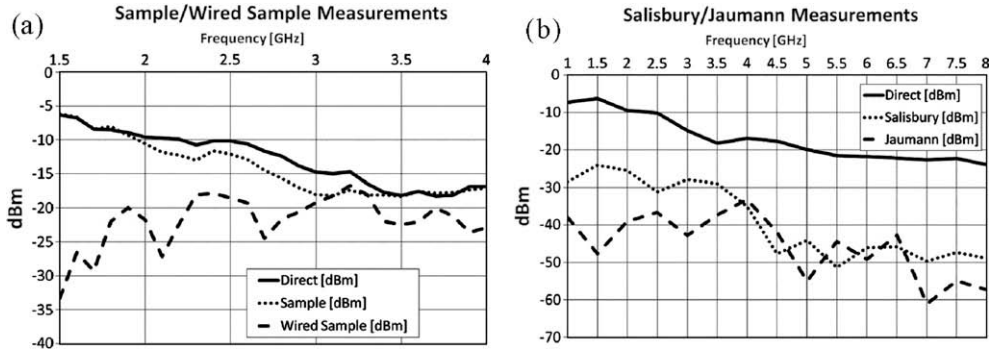

Fig. 13. Measured transmission through: (a) panel "Sample 2" (simple and with metallic insertions) and (b) Salisbury/Jaumann layers configuration with panel "Sample 2".

measurement errors. The frequency band had to be limited to 1.5 GHz due to large wavelength (longer than 20 cm) of such signals, which would increase the errors.

In order to eliminate the measurement uncertainty, for each frequency point, two distinct measurement were made: the reference measurement (without the sample), and the actual measurement with the sample placed between the antennas. The final measurement result is the difference between the two measured transmission values, with an interpretation of the attenuation induced by the measured sample or the electromagnetic shielding capability of the sample.

The measurements were made in frequency band ranging from 1 GHz to 8.0 GHz with a 0.5 GHz resolution. Some of the measurements were made in the 1–4 GHz range with a 0.1 GHz resolution in order to identify details in the predicted frequency range of the applications for the panel. In both cases we expected that the results in the 1–1.5 GHz range will be influenced in a slight manner (few dB range however) by the frequency domain of the horn antennas and by near field measurement errors.

The transmitted signal was measured for the panel "Sample 2". The results shown in Fig. 13a indicate that the losses introduced into the system by the panel are quite low. The simulation results presented in Fig. 11 suggest that the losses should not be greater than 0.5 dB. The measurements show slightly larger losses in the vicinity of 3 GHz, but it must be born in mind that two factors coincide at this range. First, the measurement accuracy offered by the measurement system is not high enough to accurately measure very low losses, which is the case. Second, the simulations have predicted that the losses of the panel are highest close to 3 GHz.

A second version of panel "Sample 2", with exactly the same dimensions, but with a flexible printed circuit board (PCB) inserted in all the ligaments was measured. The flexible PCB consists of 5 parallel copper wires. The results in Fig. 13a show the positive effect of the metallic insertions: a supplemental 5–27 dB attenuation is observed in the 1.5–2.5 GHz range. Since the primary goal of this paper was to analyse the chirality of panels, no attempt was made to model also a panel with lossy inserts. The experiment was meant only to confirm the expectations that such insertions are effective means of increasing EM losses of a panel.

In order to implement an effective shielding solution with the hexa-chiral panel, structural microwave absorbents were made, connecting the panel in a Salisbury screen configuration represented exploded in Fig. 12b with an aluminum foil (facing the receiver antenna) and a resistive sheet glued to the simple panel. Next a Jaumann Layers configuration (a supplemental chiral panel/resistive sheet glued on the Salisbury screen towards the emitter antenna) was implemented. Measurements results in Fig. 13b emphasize the improvement introduced, and validate the use of the hexa-chiral panel as an effective microwave absorbent.

6. Conclusions

Field-theoretical considerations and full wave 3D electromagnetic analysis of chiral honeycombs have been performed. It has been theoretically predicted that higher order harmonics due to structure periodicity are attenuated away from the panel surface at frequencies up to several GHz. This has been qualitatively confirmed by Microwave Studio [12] and QuickWave-3D [13] simulations showing that the supported fields are sections of a plane wave, and that the reflection coefficient minima follow the classical half-wave transformer characteristics of homogenised panels. At higher frequencies, the fields visibly degenerate from the TEM type and longitudinal components are induced. A powerful system of *S*-parameter extraction implemented in QuickWave-3D after [18] further allows extracting complex propagation constant and wave impedance as a function of frequency. By considering a product of these two curves, the homogenised nature of the panels is quantitatively confirmed and a frequency limit thereto is demonstrated. Power balance calculated as input and output ports in the above frequency range, also produced by the system of [18], validates that all injected energy remains confined not only to the TEM wave, but also to a single linear polarisation. This proves that structural chirality of the investigated honeycombs does not induce electromagnetic chirality effects, similarly as it does not affect the elastic tensor modulus [3]. This parallel between the electromagnetic and mechanical properties has not been revealed in previous studies.

Preliminary laboratory measurements confirm the analytical and numerical predictions. In particular, the considered honeycombs exhibit small material losses, and hence their shielding characteristics are essentially due to frequency-dependent reflection properties of layered structures. Modified composites that would feature enhanced absorption without deteriorating mechanical properties of the honeycombs are therefore desirable.

Foils applied on honeycomb surfaces are shown to serve this goal, while the use of absorbing foams in air volumes will be explored in future work.

References

[1] Scarpa F, Panayiotou P, Tomlinson G. Numerical and experimental uniaxial loading on in-plane auxetic honeycombs. J Strain Anal 2000;35(5):383–8.
[2] Wojciechowski KW, Branka AC. Negative Poisson's ratio in isotropic solids. Phys Rev A 1989;40(12):7222–5.
[3] Prall D, Lakes RS. Properties of a chiral honeycomb with a Poisson's ratio – 1. Int J Mech Sci 1996(39):305–14.
[4] Spadoni A, Ruzzene M, Scarpa F. Global and local linear buckling behaviour of chiral cellular structure. Phys Status Solidi B 2005;242(3):695–709.
[5] Paulac A, Scarpa F, Perrott D, Yates J. Transverse shear strength of chiral cellular core. In: Proceedings of ICEM12, Bari, Italy, 29 August–2 September 2004. p. 49–57.
[6] Evans KE. Design of doubly curved sandwich panels with honeycomb cores. Comput Struct 1991;17(2):95–111.

[7] Scarpa F, Burriesci G, Smith FC, Chambers B. Mechanical and electromagnetic behaviour of auxetic honeycomb structures. Aeronaut J 2003(2774):175–83.
[8] Smith FC, Scarpa F, Chambers B. Electromagnetic properties of re-entrant dielectric honeycombs. IEEE Microw Opt Technol Lett 2000;10(11):451–3.
[9] Smith FC, Scarpa F. Design of honeycomb-like composites for electromagnetic and structural applications. IEE Proc Sci Meas Technol 2004;151(1):9–15.
[10] Scarpa F, Lorato A, Celuch M, Wegrzyniak P, Rudnicki J, Smith C, et al. Quasi-static dielectric properties of negative Poisson's ratio haxa-chiral honeycombs. In: IEEE AP-S international symposium antennas propagation, Honolulu, US, June 2007.
[11] Kong JA. Theory of electromagnetic waves. New York: Wiley Interscience; 1975.
[12] CST Microwave Studio (1998–2008). CST GmbH. <http://www.cst.com>.
[13] QuickWave-3D (1997–2008). QWED Sp. z o.o. <http://www.qwed.com.pl>.
[14] Collin RE. Field theory of guided wave. New York: McGraw-Hill; 1960.
[15] Taflove A, Hagness S, editors. Computational electrodynamics: the finite difference time-domain method. Artech House; 2005.
[16] Celuch-Marcysiak M, Gwarek WK. Spatially looped algorithms for time-domain analysis of periodic structures. IEEE Trans Microw Theor Technol 1995;MTT-43(4):860–5.
[17] Caloz Ch, Itoh T. Electromagnetic meta materials: transmission line theory and microwave applications: the engineering approach. Hoboken, New Jersey: John Wiley & Sons, Inc.,; 2006.
[18] Gwarek WK, Celuch-Marcysiak M. Wide-band *S*-parameter extraction from FD–TD simulations for propagating and evanescent modes in inhomogeneous guides. IEEE Trans Microw Theor Technol 2003;51(8):1920–8.

Computer Standards & Interfaces 32 (2010) 101–109

Contents lists available at ScienceDirect

Computer Standards & Interfaces

journal homepage: www.elsevier.com/locate/csi

Electromagnetic characterization of chiral auxetic metamaterials for EMC applications

R. Ciobanu [a], R. Damian [a,*], I. Casian-Botez [b]

[a] Faculty of Electrical Engineering, Technical University of Iasi, Romania
[b] Faculty of Electronics and Telecommunications, Technical University of Iasi, Romania

ARTICLE INFO

Available online 22 November 2009

Keywords:
Metamaterials
Chiral
Honeycomb
Microwave absorption

ABSTRACT

A new class of auxetic materials, a hexachiral honeycomb structure with good mechanical properties, is investigated through computer simulation and measurement. The electromagnetic properties for shielding applications are taken into account. This new material shows some interesting EMC properties (e.g. −40 dB transmittance at 2.4 GHz) and promises better performance using different insertion techniques.

1. Introduction

In the past years, an increasing amount of effort has been invested in the development of new materials, with good mechanical properties, low weight and low cost. In particular auxetic materials benefit from their negative Poisson's ratio [1] and are investigated closely in the last decade [2–4]. In the same time, we witness an increase in the electromagnetic pollution of the spectrum especially in the free bands (2.4 GHz). Coding techniques have been developed to ensure the "peaceful" coexistence of multiple emitter/receiver pairs in the same frequency band. In some cases, these techniques are not sufficient, especially when good shielding for an enclosure is imperative (aeronautics [5], medicine etc.). A natural step forward is to investigate the electromagnetic properties of these materials, in order to provide good electromagnetic shielding.

Electromagnetic metamaterials are defined [6] as artificial effectively homogeneous electromagnetic structures with unusual properties not readily available in nature. An effectively homogeneous structure is a structure whose structural average cell size p is much smaller than the guided wavelength λ_g. ie. The average cell size should be at least smaller than a quarter of wavelength,

$$p < \frac{\lambda_g}{4}. \tag{1}$$

The condition (1) is known as the effective-homogeneity limit or effective-homogeneity condition, and ensures that refractive phenomena will dominate over scattering/diffraction phenomena when a wave propagates inside the medium.

The chiral panels under test are specific metamaterials. Chirality is defined by geometry [7]. An object is called chiral if it cannot be superimposed on its mirror image by translations and rotations. It's shown in [8–10] that in the isotropic composite chiral media consisting of chiral microstructures, the constitutive relations in the frequency domain valid for time harmonic electromagnetic fields can have the form:

$$\mathbf{D} = \varepsilon_c \mathbf{E} + j\xi_c H \tag{2}$$

$$\mathbf{H} = j\xi_c \mathbf{E} + \mathbf{B}/\mu_c \tag{3}$$

where ε_c and μ_c represent the permittivity and permeability, and ξ_c, the chirality admittance, which is a measure of the handedness of the medium.

2. Computer simulation

2.1. Test details

The structure used in tests was a fiber reinforced polymer [11] prototype, developed in the framework of the CHISMACOMB (CHIral SMArt honeyCOMB) FP6-EU-013641 project [12], by Italcompany (Fig. 1). The structure is a hexachiral honeycomb, each of the equally spaced cylinders being connected to his 6 neighbors by ligaments.

In order to limit the dimensions of the model, the periodicity of the structure has been investigated. While the intrinsic unit cell for this structure will contain only one cylinder and half of every surrounding ligament, numerical electromagnetic computation demands a rectangular unit cell. The rectangular unit cell is showed in Fig. 2, the length and width being equal to $2 \cdot L$(x direction) and $L \cdot \sqrt{3} \cdot$(y direction) respectively (where L is the cylinder separation). The typical dimensions used in tests are shown in Table 1.

* Corresponding author. Facultatea de Electronica si Telecomunicatii, Bd. Carol I nr.11, Iasi, 700506, Romania. Tel.: +40 232 213737x137; fax: +40 232 217720.
E-mail address: rdamian@etc.tuiasi.ro (R. Damian).

0920-5489/$ – see front matter © 2009 Elsevier B.V. All rights reserved.
doi:10.1016/j.csi.2009.11.004

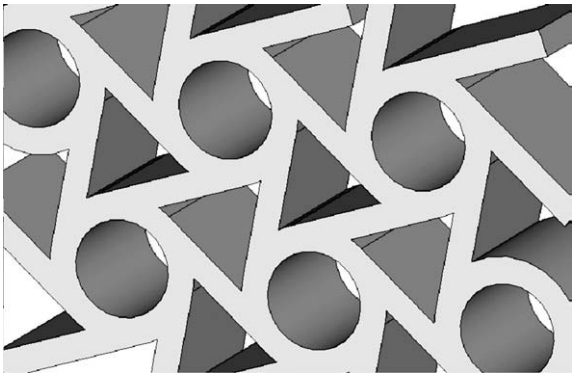

Fig. 1. Hexachiral honeycomb.

We investigate the interaction between a plane wave and an infinitely large sheet of auxetic material, at normal incidence. The boundary conditions are set to electric wall (x direction walls) and magnetic wall (y direction walls) in order to force the symmetry needed (plane wave) for the electromagnetic fields [13]. An input wave port is placed at some distance from the structure; the second (exit) wave port is added only when losses inside the structure are taken into account.

The results of the simulation show the S parameters for the structure. The typical shielding parameters reflectance, transmittance and absorption are related to the S parameters by the following equations [14].

$$R = |S_{11}|^2 \tag{4}$$

$$T = |S_{21}|^2 \tag{5}$$

$$A = 1 - R - T = 1 - |S_{11}|^2 - |S_{21}|^2 \tag{6}$$

2.2. Accuracy of the results

The software tool used for the electromagnetic simulation was CST Microwave Studio 2006, which is capable to perform both FDFD (frequency domain) and FDTD (time domain) simulations. In order to verify the boundary conditions setup a three layer Jaumann microwave absorber was investigated in the same test setup. The results in Fig. 3 were found to be identical to those mentioned in [15].

For the hexachiral structure under test, the auxetic layer is illuminated with a plane wave, coming from the z direction, with normal incidence to the material. The polarization of the plane wave in the material is imposed by the electric/magnetic wall boundary conditions, and for correct calculations we expect the electromagnetic fields inside the structure to follow the characteristics of the incident wave. As in Fig. 4, we find that inside the hexachiral honeycomb, the electric field will have only E_x component, whereas the magnetic field shows only H_y component.

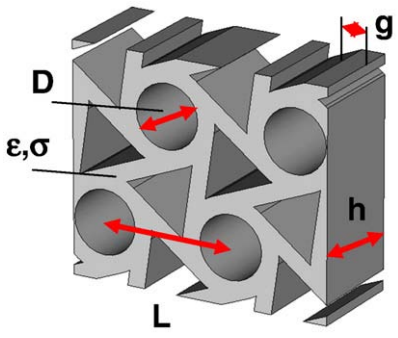

Fig. 2. Rectangular unit cell and notations used for dimensions.

Table 1
Typical dimensions.

Parameter	Value
D	18.58 mm
h	19.75 mm
L	24.72 mm
g	3.3 mm
ε	2.5 (4)
tan δ	0 (0.1–0.5)

The final test was the comparison between the FDTD and FDFD analysis results for the same structure. The two computation methods are not related, even the mesh is different in this case (hexahedral with Perfect Boundary Approximation® — PBA for FDTD and tetrahedral for the frequency domain solver). The results are found to be essentially the same (see Fig. 5).

The difference between the two curves is maximum ± 1 dB in the $1 \div 10$ GHz range, except the frequencies around the reflection annulment, where a slight variation of the zero's frequency is detected (0.1 GHz, meaning a 1.8% difference between the two minima) around 5.8 GHz. The two solvers are independent even if they belong to the same software suite, so we can estimate a ± 2 dB general error coupled with a ± 2% peak detection error for the rest of the simulations.

2.3. Convergence stability analysis

2.3.1. Frequency domain analysis

The CST Microwave Studio frequency domain solver solves the problem for a single frequency at a time, and for a number of adaptively chosen frequency samples in the course of a frequency sweep. For each frequency sample, the linear equation system will be solved by an iterative (e.g. conjugate gradient) or sparse direct solver.

Results obtained through frequency domain analysis are plotted in Fig. 6. Seven adaptive passes were performed, the number of mesh cells increasing from 2145 to 149,328. As we see, from the 5th pass, no noticeable difference between the results is found, so in this case we have a good convergence to a solution.

2.3.2. Time domain analysis

The CST Microwave Studio time domain solver calculates the development of fields through time at discrete locations and at discrete time samples. It calculates the transmission of energy between various ports and/or open space of the investigated structure.

The fields are calculated step by step through time by the so called “Leap Frog” updating scheme. It is proven that this method remains stable if the step width for the integration does not overcome a known limit. This value of the maximum usable time step is directly related to the minimum mesh step width used in the discretization of the structure. So, the denser the chosen grid, the smaller the usable time step width.

Results obtained through FDTD analysis are plotted in Fig. 7. Ten adaptive passes were performed, the number of mesh cells increasing from 2145 to 338,496. In this case, from the 5th pass, it is clear that a solution cannot be found, all values being annulled (up to a small value $\sim 10^{-5}$ which can be attributed to round off errors). This convergence problem was corrected in CST Microwave Studio 2006B (service pack 3) but at the time we wrote this paper CST Microwave Studio 2006 was used.

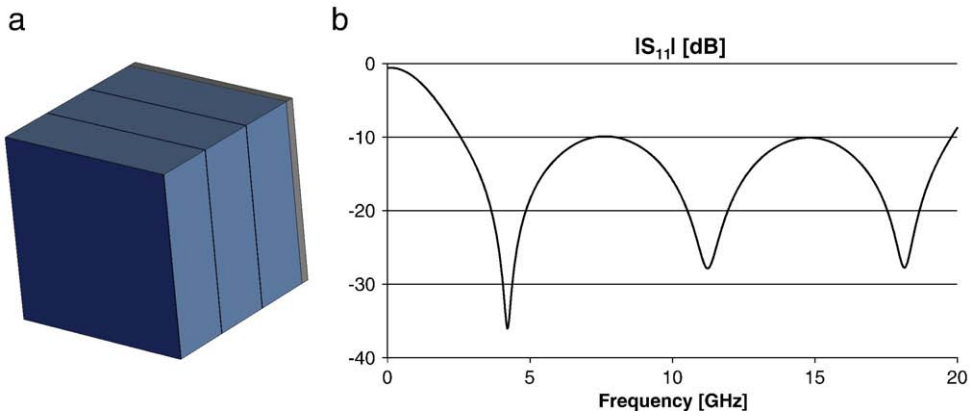

Fig. 3. Three layers Jaumann microwave absorber and results.

Both analyses (frequency and time domain) were performed with hexahedral meshing, the CST proprietary technology Perfect Boundary Approximation® (PBA) is used for the spatial discretization of the structure. The simulated structure and the electromagnetic fields are mapped to hexagonal mesh. PBA allows a very good approximation of even curved surfaces within the cubic mesh cells [16].

2.4. Computational efficiency

As Figs. 6 and 7 show, at a glance, the frequency domain solver offers better results so it would be the solver to choose in this case. However computational efficiency is to be taken into account in order to have real time solutions.

A first thing to consider is the time needed to perform the computations. Fig. 8 shows the time elapsed to the achievement of the solution. For the reference, all previous computations were made on an IBM compatible computer, with Intel Core2 E6400@2.13 GHz processor, 2 GB RAM, only one of the two separate processing cores being used by the solver.

The first thing to consider is the tremendous difference between the two solvers. The 7th pass frequency solver used 152,068 s (e.g. 42 h, 11 m, and 53 s) to achieve the solution whereas the 10th pass time domain solver only needed 91 s. When multiple analyses are to be performed (parametric studies in this paper involved more than 200 different analyses) the time consumed has a critical importance.

Another important parameter is the number of mesh cell used for the discretization of the structure. This number closely relates with the amount of memory used in computations. As mentioned before the number of mesh cells was 338,496 for the FDTD solver 10th pass, and only 149,328 for the FDFD solver 7th pass.

However it's not only the mesh cells number who decides the memory occupation. Every algorithm has its own memory consumption particularities. The time domain algorithm is more memory efficient (even at 2 times more mesh cells, less memory is used e.g. 97 MB vs. 865 MB).

2.5. Parametric analysis

Parametric studies investigated the effect of the dimensions (L, D, h, and g) and material properties (ε, σ, and tan δ). Figs. 9 and 10 show the influence of D, g, L, and h (in this order) for the lossless dielectric over the reflection coefficient (S_{11}), and Figs. 11 and 12 show the influence of ε, σ, and tan δ over reflection coefficient (S_{11}) or over the transmission coefficient (S_{21}) when losses are taken into account (σ and tan δ).

Analysis shows that the chiral structure has almost identical properties (Figs. 9–11) with an equivalent homogeneous dielectric layer, so the mechanical and thermal advantages provided by the structure do not affect the electromagnetic properties in the bandwidth considered (0.1–10 GHz).

An interesting conclusion is the almost undetectable influence of the cylinder diameter (D) and cylinder separation (L) over the shielding properties, meaning that those parameters can be chosen strictly from mechanical and thermal considerations. Other parameters offer the

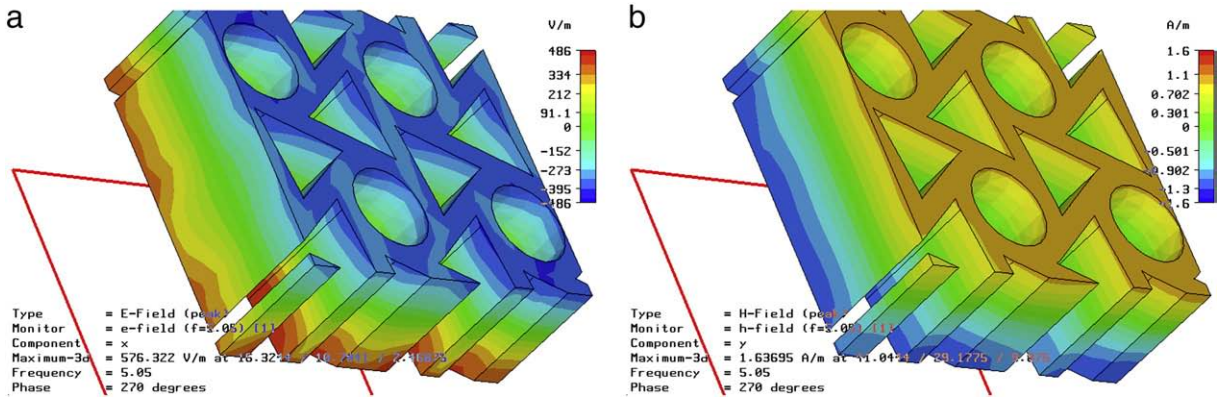

Fig. 4. E_x (left) and H_y (right) inside the structure.

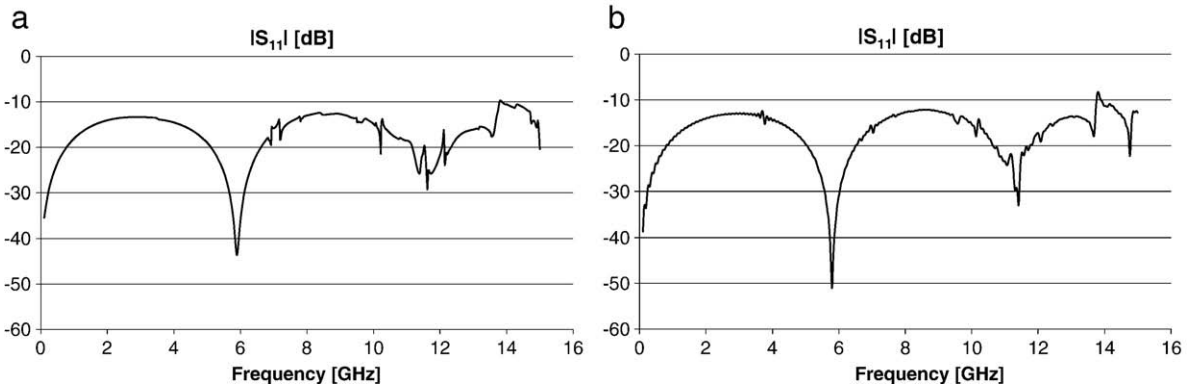

Fig. 5. S_{11} for the lossless structure by FDFD (left) and FDTD (right) computation.

expected results, e.g. lower transmission with greater losses (tan δ), increased ligament thickness (g) and the variation of the frequency of the reflection zeros with layer's height (h).

For a chiral layer (of thickness d), positioned on an ideally conducting surface, the reflection coefficient for normally incident plane waves is [7]:

$$R = \frac{\eta_M - \eta_0}{\eta_M + \eta_0} = \frac{Z_M - Z_0}{Z_M + Z_0} \tag{7}$$

where Z_M is the input impedance at the layer boundary (sometimes called the surface impedance), given by

$$Z_M = -j\sqrt{\frac{\mu_c}{\varepsilon_c}}\tan(d\omega\sqrt{\varepsilon_c\mu_c}). \tag{8}$$

In this equation ε_c and μ_c represent the usual permittivity and permeability in the formalism given by Eqs. (2) and (3). In Eq. (8) there is no dependence of the reflection coefficient on the chirality parameter, ξ_c so the results we obtain verify the existing theory. Only normal incidence on chiral media was considered, the case of oblique incidence [17] could show some influence of the microscopic structure, and must be studied further. The microscopic chirality of potential inclusions affects the values of the permittivity and permeability in Eq. (8), which then define the reflective properties, so the sparse structure of typical chiral materials offers good energy dissipation (always a "plus" for an energy absorber) and easy access for eventual FSS (Frequency Selective Surfaces) insertions inside the material in order to obtain better electromagnetic absorption. An analysis of the effective electromagnetic properties of other types of honeycomb composites is made in [18], as long as the effective-homogeneity condition (1) applies. However in [18] only the

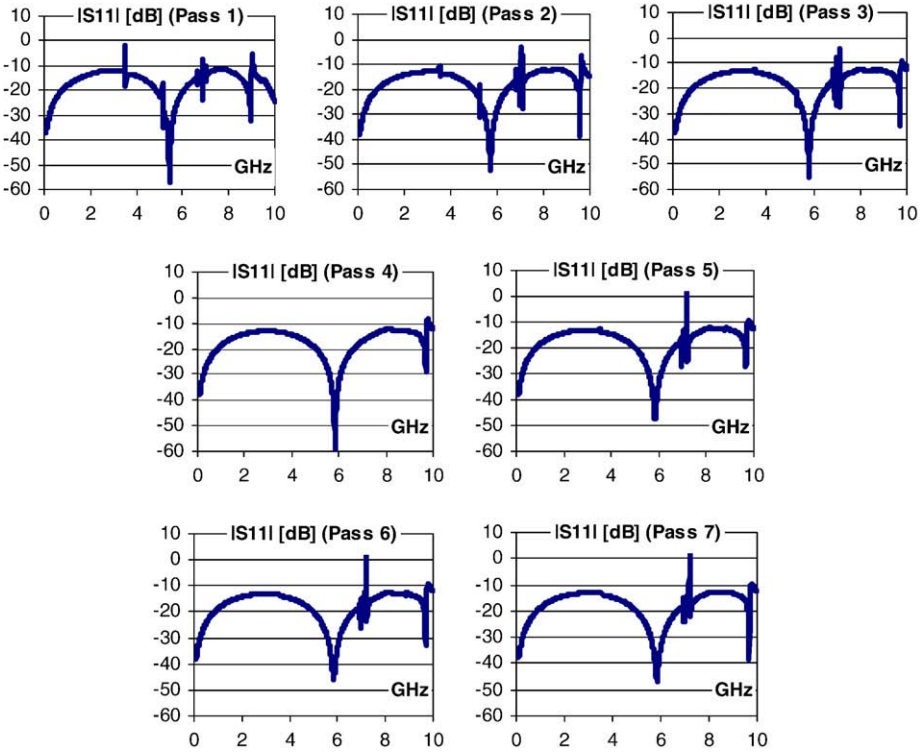

Fig. 6. $|S_{11}|$ versus frequency (passes 1 to 7, frequency domain analysis).

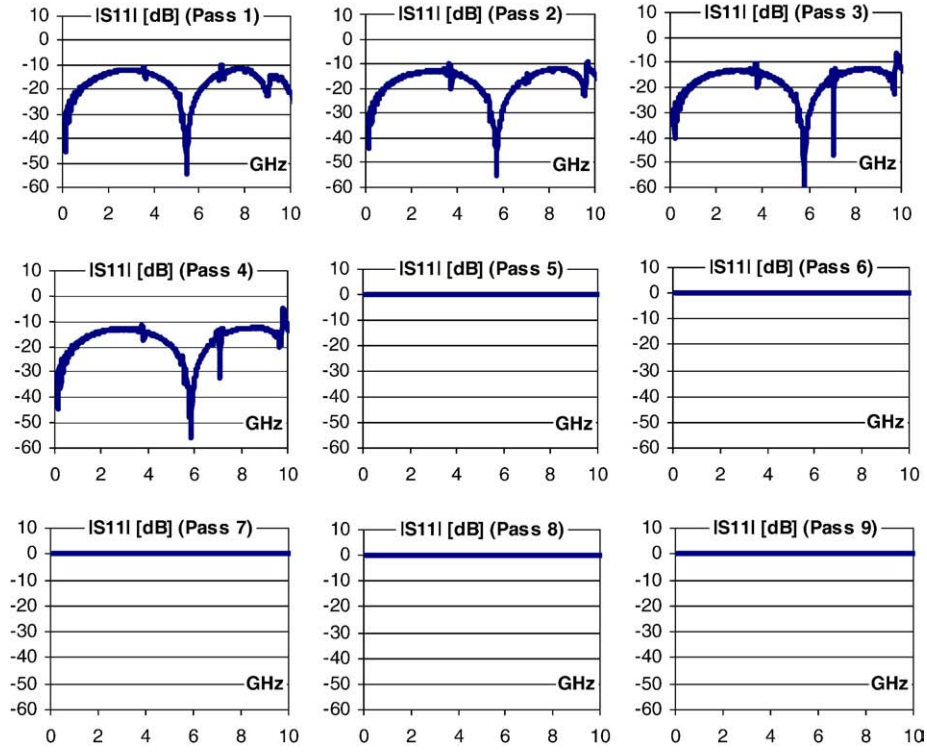

Fig. 7. $|S_{11}|$ versus frequency (passes 1 to 9, time domain analysis).

dependence of the effective electrical permittivity on the fill factor (density of the structure) was considered.

Figs. 9–11 show that for the lossless chiral layer we have a typical half-wave reflectionless slab [19]. We obtain zeroes for the reflection coefficient at the frequencies which verify the condition:

$$h = k \cdot \frac{\lambda_g}{2} = \frac{k}{2} \cdot \frac{c}{f\sqrt{\varepsilon_{eff}}} \tag{9}$$

where k must be an integer and λ_g is the guided wavelength, inside the equivalent homogeneous dielectric slab.

This behavior offers interesting electromagnetic applications, as radar invisibility or building wall transparency. As an example we can imagine a situation where for an internal wireless network we must minimize the multiple reflections which can occur inside the building.

Eq. (9) offers the possibility to use the results in Fig. 10 to investigate the variation of the effective electrical permittivity on the frequency. Every value for layer's height (h) generate at least two minima of the reflectivity in the bandwidth considered, corresponding to $k=1$, $k=2$ in Eq. (9). We can compute the effective electrical permittivity with Eq. (10).

$$\varepsilon_{eff}(f_{min,k}) = \left(\frac{k \cdot c}{2f_{min,k}} \cdot h\right)^2 \tag{10}$$

The effective electrical permittivity increases linearly with the frequency, as the electromagnetic field is confined inside the dielectric at higher frequency. The results in Fig. 10 on which Fig. 13 is based are obtained for $\varepsilon=2.5$ for the base material. In this case we find the effective permittivity ranging from 1.61 to 2.1, depending on the frequency. Also as the frequency increases we notice slight variations from the predicted linear increase, as the chirality of the structure becomes more and more evident.

The effects of the chirality appear as we increase the frequency, the electrical permittivity and the cylinder separation. In the typical situation (Table 1) Eq. (1) gives a frequency limit of about 2.37 GHz. Close inspection of the results (especially Fig. 11 where D and g

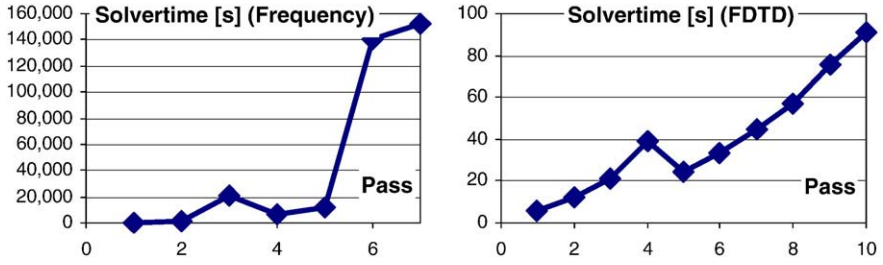

Fig. 8. Solver time versus passes — frequency (left) and time (right) domain solvers.

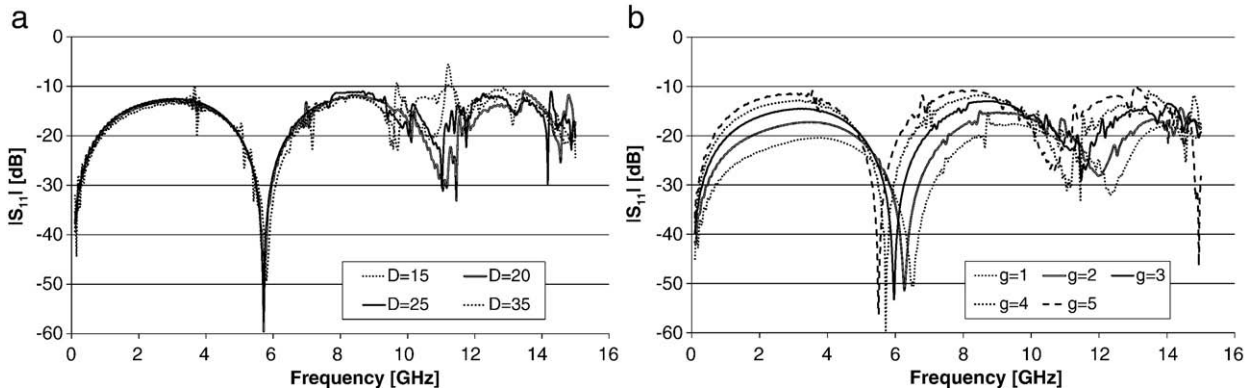

Fig. 9. Internal cylinder diameter (D — left) and ligament thickness (g — right) influence over S_{11}.

parameters have no influence over the chiral behavior) shows that obvious effects of the microscopic chiral structure are visible at 8 GHz.

Condition (1) can be expressed in terms of visible influence as:

$$L \cdot f \cdot \sqrt{\varepsilon_{\text{eff}}} \approx \frac{3c}{4}. \tag{11}$$

The other results verify this relationship. Increase of ε from 2.5 to 10 (Fig. 11a) lowers the frequency of appearance of chiral effects from 8 GHz to 4 GHz (the square root of the permittivity factor of 4). Increase of L to 40 mm (Fig. 10a) shows the same effect starting from 5 GHz.

We can conclude that regarding the hexachiral honeycomb, chirality influence becomes obvious when relation (11) applies, but while visible, this influence does not affect the macroscopic behavior of the panel under test. The hexachiral panel behaves as a homogeneous dielectric, with a different effective electrical permittivity (Fig. 13), thus different methods to increase the microwave shielding capability must be applied in order to obtain an EMC capable material. Insertion of FSS or inclusion of the panels in Salisbury screen configuration could offer this result. For the measurement section of this paper we will focus on a simpler configuration, which consists in the deposition of two aluminum foils on both sides of the panel. The selected method has the advantage to have a minimal influence over

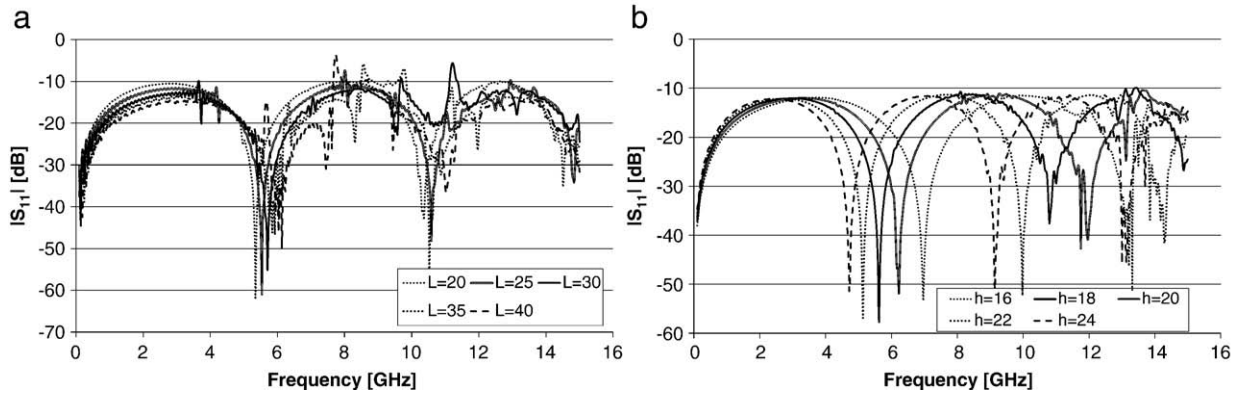

Fig. 10. Cylinder separation (L — left) and layers' height (h — right) influence over S_{11}.

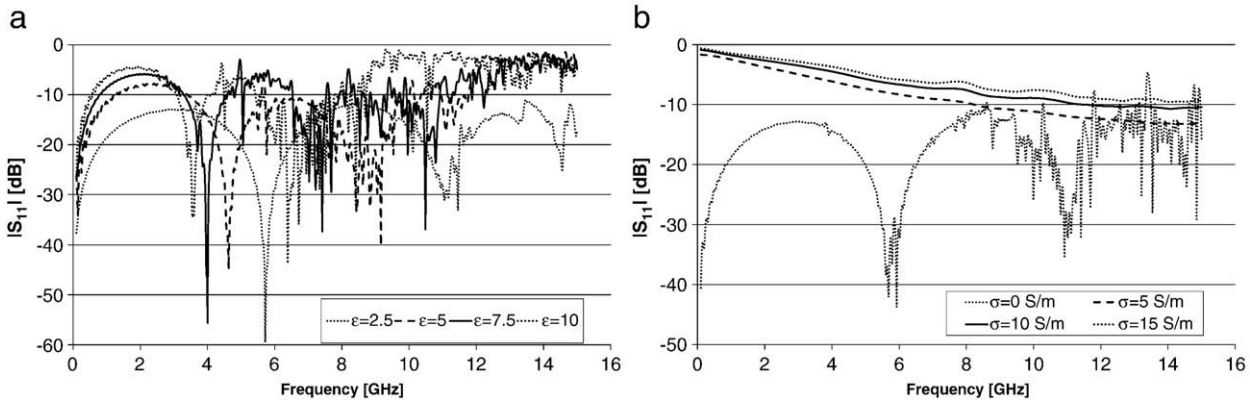

Fig. 11. Electrical permittivity (ε — left) and electric conductivity (σ — S/m — right) influence over S_{11}.

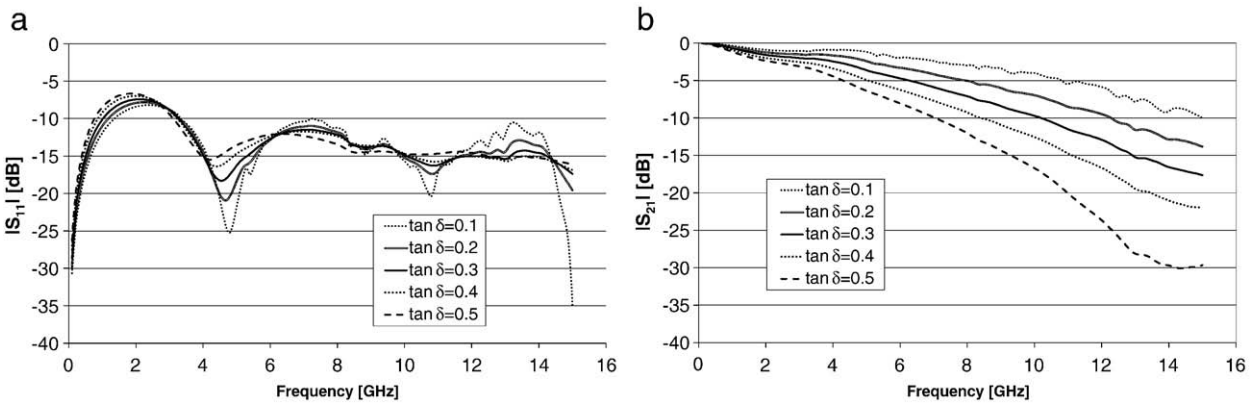

Fig. 12. Loss tangent (tan δ) influence over S_{11} (left) and S_{21} (right).

the mechanical properties of the panel (which are a key element in the CHISMACOMB Project [12]).

3. Measurements

3.1. Measurements detail

Measurements were performed using an Agilent E7405A EMC spectrum analyzer (frequency domain: 250 kHz to 40 GHz), Agilent E8257 PSG Analog Signal Generator (frequency domain: 9 kHz to 26.5 GHz), and two ETS Lindgren 3115 horn antennas (frequency domain: 1 GHz–18 GHz) in the free-space transmission measurement method (Fig. 14). Transmission simulations (Fig. 12) show that losses inserted by the intrinsic panel are in the 3–4 dB range (tan δ for the base material is around 0.01). So the intrinsic panel, equivalent from the macroscopic point of view with a homogeneous dielectric, is not suited alone for EMC applications.

In order to investigate possible microwave shielding applications, two 0.5 mm thick aluminum foils were placed on both side of the layer (Fig. 14), and the bandwidth investigated was around the free ISM band at 2.4 GHz (e.g. 1.5–3 GHz) in connection with wireless, Bluetooth or DECT telephony applications. Multiple measurements were performed with different power levels at the generator (0 dBm, −10 dBm, and −20 dBm) and were repeated seven times [20].

In order to eliminate the incertitude introduced by the quite irregular frequency characteristics of the antennas, for every frequency point, two distinct measurements were made: the first, or the reference measurement, without the probe inserted between antennas and the second, or the sample measurement, was repeated seven times with the corresponding measured sample between antennas. The value of interest will be the difference between the two measurements, as the supplemental attenuation induced by the measured sample, hence the electromagnetic shielding capability of the chiral layer with aluminum foils.

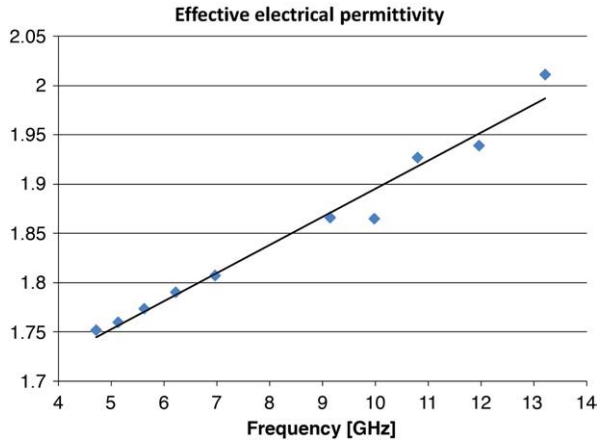

Fig. 13. Effective electrical permittivity.

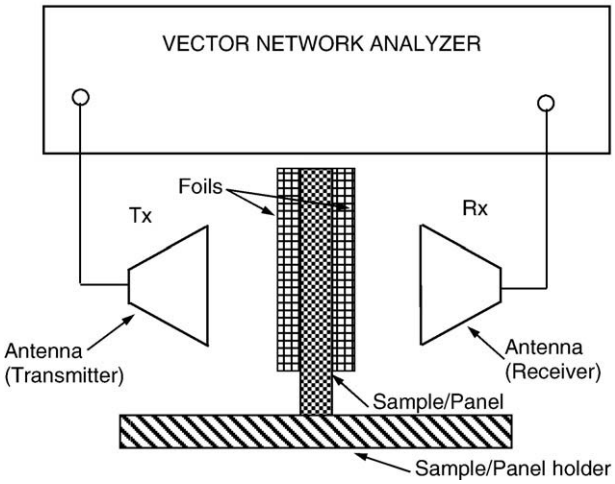

Fig. 14. Sample measurement technique.

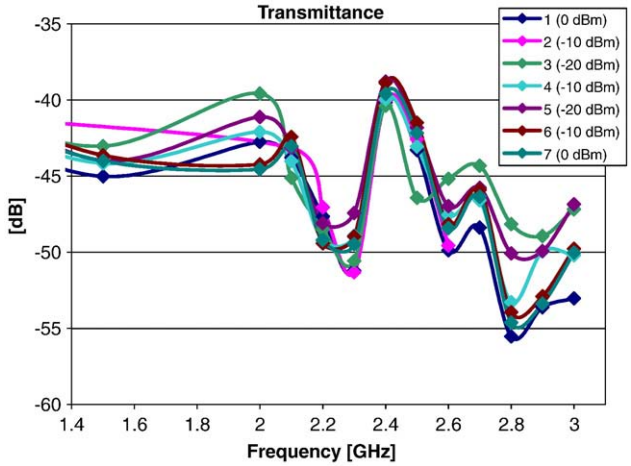

Fig. 15. Hexachiral structure transmittance.

Table 2
Measurement results and errors.

Frequency [GHz]	1.5	2	2.2	2.4	2.6	2.8	3
Transmittance [dB]	−43.97	−42.39	−48.45	−39.69	−47.96	−52.60	−49.51
Standard Deviation	0.65	1.89	0.90	0.63	1.60	2.87	2.27
Range [dB]	1.98	4.97	2.36	1.59	4.71	7.38	6.19
Meas. count	6	6	7	7	7	6	6

3.2. Measurement results

The transmittance computed from the measured transmitted power and the generator power level is plotted in Fig. 15. The measured values show good repetitive values. The transmittance at 2.4 GHz (the free bandwidth of interest) has an interesting value of −40 dB transmission (Fig. 15, Table 2) which denotes that the structure under test can clearly be used as a microwave absorber, this values being typical for a good microwave absorber [15].

Table 2 shows the statistical data for the measured values. Measurements below 1.5 GHz were omitted as the frequency range of the antennas makes them uncertain. Statistical analysis shows a measurement error ranging from 0.9 dB to 2.9 dB in higher frequencies. This precision is enough to characterize the shielding properties of the chiral panel between the two aluminum foils but certainly will not be sufficient to investigate the transmission characteristics of the simple panel (3–4 dB in the 1.5–3 GHz — Fig. 12). While better methods exists, as the coaxial holder method, which imply a sample inserted inside a waveguide, the geometrical size of the structure (mainly L) will impose a very large guide in order to include several cells. The limited bandwidth of such a waveguide (for example WR 770 in USA standard) will make any attempt to find accurate information useless.

4. Conclusions

The evaluation of the intrinsic electromagnetic properties of an auxetic material was made. We used CST Microwave Studio, for his capability to perform both frequency and time domain simulations. Particular boundary conditions (electric/magnetic walls) were used to force the electromagnetic field inside the structure to be the same as with an incident plane wave. The stability and efficiency analyses of both simulation methods were performed, showing the optimum compromise between speed and accuracy. More than 200 different structures were then analyzed in order to obtain a complete characterization of the intrinsic proprieties of the chiral metamaterial under test. The results show that the performance of the hexachiral structure is equivalent to a homogeneous dielectric layer, some of the properties being influenced by the specific geometry of the structure.

Measurements were performed in some typical microwave absorber configurations and the results show good electromagnetic shielding capacities. The same structure which offers good mechanical and thermal behaviors [21] gives access to some improvement techniques. This work will be followed by the investigation of the possibility to improve these electromagnetic properties through the use of insertions, metallization etc.

Acknowledgements

The authors gratefully acknowledge the support from the CHISMACOMB (CHIral SMArt honeyCOMB) FP6-EU-013641 project.

The authors wish to thank Mr. Tan Phu Vuong from “Laboratoire de Conception et d'Intégration des Systèmes”, ESISAR, Valence, France, for access to CST Microwave Studio 2006.

References

[1] J. Grima, Negative, negative and more negative: systems exhibiting negative Poisson's ratio, negative thermal expansion and/or negative compressibility, 4th International Workshop on Auxetics and Related Systems, Malta, 2007, p. 8.
[2] L.W. Li, D. You, M.-S. Leong, T.-S. Yeo, Electromagnetic scattering by multilayered chiral-media structures: a scattering-to-radiation transform, Journal of Electromagnetic Waves and Applications 14 (2000) 401–404.
[3] H. Ammari, M. Laouadi, J.-C. Nedelec, Low frequency behavior of solutions to electromagnetic scattering problems in chiral media, SIAM Journal of Applied Mathematics, Society for Industrial and Applied Mathematics 58 (3) (1998) 1022–1042.
[4] Rachid Oussaid, Brahim Haraoubia, Behavior of a chiral material in terms of a guided wave propagation, International Journal of Applied Electromagnetics and Mechanics 19 (2004) 631–635.
[5] D. Bornengo, F. Scarpa, C. Remillat, Evaluation of hexagonal chiral structure for morphing airfoil concept, Proceedings. IMechE, Part G: J. Aerospace Engineering, vol. 219, 2005, pp. 185–192.
[6] Christophe Caloz, Tatsuo Itoh, Electromagnetic Metamaterials: Transmission Line Theory and Microwave Applications: The Engineering Approach, John Wiley & Sons, Inc., Hoboken, New Jersey, 2006.
[7] Frederic Mariotte, Sergei A. Tretyakov, Bruno Sauviac, Modeling effective properties of chiral composites, IEEE Antennas and Propagation Magazine 38 (2) (April 1996) 22–32.
[8] Frederic Mariotte, Nader Engheta, Reflection and transmission of guided electromagnetic waves at an air–chiral interface and at a chiral slab in a parallel-plate waveguide, IEEE Transactions on Microwave Theory and Techniques 41 (11) (November 1993) 1895–1906.
[9] P. Pelet, N. Engheta, The theory of chirowaveguides, IEEE Transactions on Antennas and Propagation 38 (1) (January 1990) 90–98.
[10] M. Oksanen, P. Koivisto, S. Tretyakov, Vector circuit method applied for chiral slab waveguides, Journal of Lightwave Technology 10 (2) (February 1992) 150–155.
[11] Iqbal Ahmed Khany, S.C. Raghavendray, A.B. Kulkarni, Polyester-based chiral materials for microwave absorption applications, International Journal of Electronics 90 (3) (2003) 159–166.
[12] CHISMACOMB, A FP6 Specific Target Research Project, http://www.chismacomb.eu/, 2006.
[13] CST GmbH, Application Note, Photonic Crystal Simulation, Article ID: 296, 2007 — http://www.cst.com.
[14] Y.K. Hong, C.Y. Lee, C.K. Jeong, D.E. Lee, K. Kim, J. Joo, Method and apparatus to measure electromagnetic interference shielding efficiency and its shielding characteristics in broadband frequency ranges, Review of Scientific Instruments 74 (2) (February 2003) 1098–1102.
[15] Paul Saville; Trisha Huber; Darren Makeiff — Fabrication of Organic Radar Absorbing Materials Defence R&D Canada — Atlantic, Technical Report DRDC Atlantic TR 2005-124, May 2005.
[16] CST of America, A software suite with total synergy, Microwave Journal 49 (1) (2006).
[17] Raymond Redheffer, The dependence of reflection on incidence angle, Ire Transactions on Microwave Theory and Techniques (October 1959) 423–429.
[18] Martin Johansson, Christopher L. Holloway, Edward F. Kuester, Effective electromagnetic properties of honeycomb composites, and hollow-pyramidal and alternating-wedge absorbers, IEEE Transactions on Antennas and Propagation 53 (2) (February 2005).
[19] Sophocles J. Orfanidis — Electromagnetic Waves and Antennas, online book, ch 5, pp. 160–166, http://www.ece.rutgers.edu/~orfanidi/ewa/, 2008.
[20] G. Busse, A.F. Jacob, Enhancing the range of waveguide measurement setups for chiral media by step discontinuities, International Journal of Applied Electromagnetics and Mechanics 9 (1998) 115–121.
[21] M.R. Hassan, F. Scarpa, M. Ruzzene, N.A. Mohammedd, Smart shape memory alloy chiral honeycomb, Materials Science and Engineering A 481−482 (2008) 654–657.

Romeo-Cristian Ciobanu was born in Piatra-Neamt, Romania, in 1961. He received a Ph.D degree in Electrical Engineering from the University Politehnica of Bucharest and a Ph.D degree in Chemistry from the Technical University of Iasi.
He is currently a Professor at the Technical University of Iasi, Electrical Engineering Department. His research focuses on Industrial Diagnosis, Dielectric Measurements, Quality and Maintenance, Composite Technologies.

Radu-Florin Damian was born in Vaslui, Romania, in 1972. He received the M.Sc. and Ph.D. degree in electronic engineering from the Technical University of Iasi.
He is currently senior lecturer of microwave engineering and optoelectronics at the Technical University of Iasi, Electronics and Telecommunications Department. His research focuses on numerical electromagnetics and optoelectronics.

Irinel Casian-Botez was born in Iasi, Romania, in 1955. He received the M.Sc. degree in microwave engineering from the INP Toulouse, France, in 1992, and Ph.D. degree in electronic engineering from the Technical University of Iasi.
He spent one year with ENSEEIHT Toulouse, where he was involved in the field of time domain electromagnetics. He is currently a Professor of microwave engineering at the Technical University of Iasi. His research concerns electromagnetics and nanoelectronics.

Rom J Leg Med [23] 211-216 [2015]
DOI: 10.4323/rjlm.2015.211

Study on the relationship between the concentration of ethanol in the blood, urine and the vitreous humour

Beatrice Gabriela Ioan[1], Victor Jitaru[2], Radu Damian[3,], Simona Irina Damian[4]*

Abstract: Ethanol (ethilic alcohol) is widely available, being the most commonly used drug worldwide and often involved in forensic cases. It therefore becomes essential to analyze and correctly interprete the blood alcohol concentration (BAC) in samples collected during autopsy. The purpose of our study was to establish a relationship between the concentration of ethanol in vitreous humor, urine and blood, which should lead to a more accurate assessment of the BAC, in cases where direct measurement is difficult because of putrefaction, severe trauma, embalming etc. The study was conducted at the Institute of Forensic Medicine Iasi between December 2010 and August 2012 on a total of 202 forensic cases in which samples of blood, urine and vitreous humor were collected for toxicological examination. We found a strong correlation between the concentration of ethanol in blood and vitreous humor and a weaker correlation between the concentration of ethanol in blood and urine. We also identified a method for calculation of blood alcohol concentration at the time of death from blood alcohol concentration at the time of autopsy.

Key Words: ethilic alcohol, blood, vitreous humour, urine, autopsy.

Determining the cause of death in forensic practice is one of the most important and difficult task of a forensic pathologist. The toxicological exam from the proper collection of samples, to analyzing and correctly interpreting them often plays an important role in this process, given that the toxic substances may determine or favour death.

Ethanol, the psychoactive constituent of alcoholic beverages, is widely available, being the most commonly used drug worldwide and often involved in forensic cases. It therefore becomes essential to analyze and correctly interprete the blood alcohol concentration (BAC) in samples collected during autopsy. The challenge is all the more important as the interpretation of postmortem BAC may come across difficulties due to lack of homogeneity in blood samples, bacterial postmortem alcohol production, diffusion of alcohol from stomach contents or contaminated airways. Also, post-mortem BAC can be influenced by changes in hematocrit due to refill volume replacement therapy by administering blood products, volume expander or other resuscitation maneuvers which may result in dilution of intravascular concentration of alcohol.

The ingested alcohol is rapidly absorbed in the digestive tract, with varying rates at different levels. Because ethanol is soluble in water, its concentration in

1) Associate Professor, forensic pathologist, "Grigore T. Popa" University of Medicine and Pharmacy, Institute of Legal Medicine, Iasi, Romania
2) Forensic Pathologist, Institute of Legal Medicine, Iasi, Romania
3) Lecturer, Gheorghe Asachi Technic University, Iasi, Romania
** Corresponding author: Email: rdamian@etti.tuiasi.ro*
4) Lecturer, forensic pathologist, "Grigore T. Popa" University of Medicine and Pharmacy, Institute of Legal Medicine, Iasi, Romania

different compartments of the body directly correlates with the water content of each tissue or fluid. Therefore, biological products with a high content of water, such as blood, urine and the vitreous humor have much higher concentrations of ethanol versus parenchymal organs (eg. liver). For this reason, the literature recommends routine collection of blood, urine and vitreous humor samples in order to perform the toxicological examination.

Blood is the "golden" biological product for the determination of post-mortem alcohol concentration because it directly correlates with the degree of intoxication achieved during life and thus with the triggered pathophysiological effects.

Urine is the second important biological product in post-mortem toxicological analysis, being the main route of elimination of toxics. However, urine alcohol concentration (UAC) is correlated with the intravascular level of ethanol only if urine is formed after the ingestion of ethanol. The alcohol concentration in urine is generally smaller than that in the blood until the BAC peaks (absorption phase), later becoming bigger as the BAC decreases (excretion phase). The ratio between the concentration of ethanol in blood and in urine varies in a very wide range, between 0.21 and 2.66 [1], with an average accepted value of 1.28. In fact, UAC reflects an average of BAC for as long as it was produced, and this average is influenced by many factors. Under these conditions, an independent value of UAC may not reflect or predict the BAC, but, in conjunction with the value of BAC, it may point to the alcohol metabolizing phase in the body. But the level of UAC may as well be influenced by decay. Although, in general, it is considered that the urine is less likely to be influenced by the effects of postmortem production of alcohol than blood, there are studies indicating that large amounts of alcohol can be produced when glucose (in persons suffering from diabetis) and a microorganism (Candida albicans) are found in the urine.

Vitreous humor is one of the biological products most widely used in forensic toxicology. The vitreous is particularly useful in cases where the body is severely damaged, affected by putrefaction or where the toxicological exam is done after embalming the body and BAC determination becomes irrelevant. The isolated location of the eyeball makes the vitreous humor not be exposed to bacterial contamination and alcohol diffusion from gastric and pulmonary levels. The intact eyeball is relatively avascular and isolated from other tissues and fluids, so that vitreous humor is a sterile product, useful for quantitative determinations. The level of alcohol in the vitreous humor (VAC) is not influenced by the formation of alcohol during putrefaction and the electrolyte and metabolites concentrations of drugs in this environment remain stable post-mortem for a longer period of time than in blood. Due to these features, the quantitative determination of VAC is an excellent way to interpret the value of alcohol, as a measure of quality control. Given the high concentration of vitreous water, the concentration of ethanol in this environment is proportionally higher than in blood, when they are in balance, the report referred to in the literature is VAC / BAC = 1.2: 1 [2- 4]. The balance between the BAC and VAC is about 1-2 hours delayed. The VAC thus gives us an opportunity to look back and provide information on the BAC about 1-2 h before the time of death. In the phase of absorption, the VAC is lower than BAC. If the person stops drinking alcohol, the blood alcohol level will continue to rise as absorption continues, then it is kept in plateau for a while and then it decreases. The alcohol in vitreous humor, which is metabolized more slowly than in blood, continues to grow when the intravascular alcohol remains in plateau. Subsequently, this also reaches a maximum which lasts for a certain period, followed by decrease. When balancing the concentrations, the VAC is higher than BAC due to more elevated water level. The ratio 1.2: 1 between the two concentrations remains constant as the VAC and the BAC decrease simultaneously.

OBJECTIVES

The purpose of this study was to establish a relationship between the concentration of ethanol in vitreous humor, urine and blood, which should lead to a more accurate assessment of the BAC, in cases where its direct measurement is difficult because of putrefaction, severe trauma, embalming etc.

We also followed if the official method of alcohol dosage in Romania (Cordebard) can be applied for qualitative and quantitative analysis of alcohol in the vitreous in order for these determinations to be available (from technical and financial perspective) to all forensic services in the country.

MATERIAL AND METHOD

The study was conducted at the Institute of Forensic Medicine Iasi between December 2010 and August 2012 on a total of 202 forensic cases in which samples of blood, urine and vitreous humor were collected for toxicological examination. Also, demographic data regarding the victim (age, sex), postmortem interval (PMI) and the time of death were collected. In the event that there was a previous hospitalization period, it was intended that this period be less than 24 hours.

Blood samples were collected before opening the body, mainly from the peripheral vessels (femoral vein - of choice) so as to avoid possible artifacts caused by contamination of the blood with peritoneal fluid, gastric contents etc. as a consequence of portmortem increase of biological membranes and vascular walls permeability. This was possible in 188 cases; in 14 cases liver blood was collected.

Table 1. Study group: demographic caracteristics of the victims and harvested samples

N (total number of cases)	202
Period	December 2010- August 2012
Age	49,9 ±17,4 years (average ± SD) 51/ 20-61 years (average / maximum interval of incidence)
Gender	163 men 39 women
Blood samples	188 –femoral blood 14 – liver
Alternative harvesting	86 – vitreous humour 39 – urine
Post mortem interval (PMI)	9-96 h 24 /23,25-24 h (average / maximum interval of incidence)

Table 2. Weather data (temperature and humidity) according to METAR system and meteorologic stations Adamachi and Miroslava- March 2012

Parameters	Weather station/ Decade	Average METAR (LRIA)	Adamachi	Miroslava
Average temperature [°C]	1-10	-1.9	-1.8	-1.3
	11-20	5.2	5.8	4.0
	21-30	9.1	8.8	9.2
	Month	4.3	4.4	4.1
Relative humidity [%]	1-10	78	73	78
	11-20	72	63	72
	21-30	63	59	64
	Month	71	65	71

Urine samples were collected in 39 cases, directly from the bladder through an incision.

Vitreous humor was collected in 86 cases, by puncturing the external angle of both eyeballs with a thin needle [5-8].

Of the 86 cases in which the vitreous humor harvesting succeeded, 1 case was excluded because the value of the BAC was zero; of the 39 cases in which urine was collected, 3 were excluded as the BAC was also zero.

The study group consisted of 163 men and 39 women, with an age average of 49.9 ± 17.4 years (Table 1).

The samples were analyzed by Cordebard method (modified by D. Banciu and I. Droc). This method is based on the oxidation of ethanol which was isolated by distillation to the acetic acid with a nitrochromic mixture (composed of an aqueous solution of potassium dichromate and nitric acid), followed by iodometric re-titration of the dichromate excess (with the potassium iodide solution 2% freshly prepared).

To reduce the risk of errors, equal amounts of each sample were used for toxicological analysis.

The effects of environmental conditions on the concentration of ethanol in various fluids were studied using weather reports in METAR format. This type of report is used by pilots prior to takeoff and by meteorologists to obtain weather forecasts. Information (including the setting of hourly temperature, humidity, atmospheric pressure, rainfall, dew point and other parameters) was collected from publicly available data of Iasi International Airport (International Civil Aviation Organization - LRIA) located 8 km NE of the city centre (27°38'E longitude, latitude 47°10'N, altitude 102 m).

Analysis of the raw data from METAR system was preferred over data from other weather stations as they mostly present aggregated data. METAR data validation was performed by comparison with data from two other weather stations in the surroundings of Iasi (Adamachi and Miroslava). Relatively constant values were seen in all 3 recording points (i.e. March 2012 - Table 2).

The data obtained was analyzed with the SPSS system, version 19. The linear regression allowed us to identify the parameters that influence the BAC. In view of the statistical analysis the cases in which toxicology results were negative were eliminated.

RESULTS AND DISCUSSION

The statistical analysis revealed a strong correlation between the concentration of ethanol in urine and vitreous humor and blood.

In the relation UAC-BAC, the Pearson correlation coefficient is r = 0.905 (36 cases - Fig. 1), while, in the relation VAC-BAC, this coefficient is r = 0.887 (85 cases - Fig. 2).

The VAC-BAC ratio on the 85 cases in which both blood and vitreous humor were collected, was 1.21 (SD 0.98) with an average of 1.11.

During data analysis, two extreme values were observed in which, most likely, the BAC value was very low, possibly mistaken. By excluding these two cases, the average relation VAC / BAC became 1.07 (SD 0.299), with the same average value of 1.11 (Table 3).

Our results can be placed within the limits of the ratio VAC/ BAC identified by other studies quoted in the literature. In one of the largest studies on this topic (706

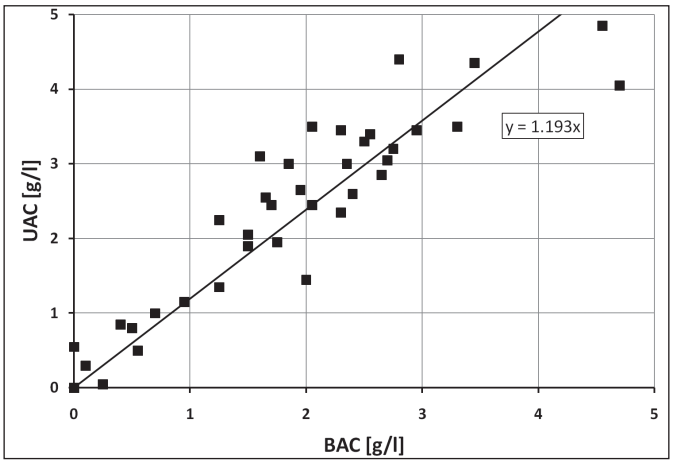

Figure 1. Correlation UAC[g/l] - BAC[g/l].

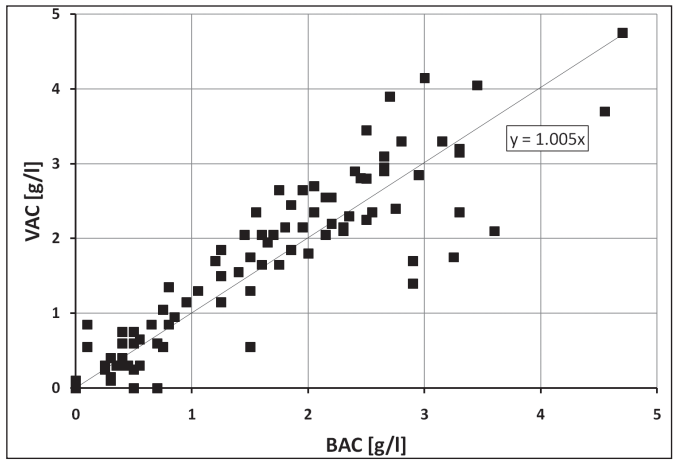

Figure 2. Correlation VAC[g/l] - BAC[g/l].

Table 3. VAC/BAC ratio on 85 cases and 83 cases respectively.

Test	Average (*Median*)	SD	*2.5th/97.5th reference limits*
All data (85 cases)	1.21 (1.113)	0.98	0.50/1.63
83 cases (2 cases excluded)	1.07 (1.107)	0.30	0.50/1.51

forensic cases), Jones and Holmgren have identified an average VAC/ BAC of 1.19, with a standard deviation of 0.285 [9]. DiMaio [2] and Molina [4] identified a VAC/ BAC ratio of 1.2, while Spitz [3] provides values ranging between 1.12 and 1.2. Coe and Sherman placed this report between 0.9 and 1.38, with an average of 1.2. Other studies provide larger intervals, such as 0.71 to 3.71, with an average of 1.29 [10]. The literature review by Kugelber [11] in 2007 mentioned an average reference interval for the VAC / BAC ratio of 1.15-1.20.

Obtaining a VAC/ BAC ratio within the limits provided by the literature allows us to consider that the Cordebard method can be applied in VAC determination; we must mention that for a correct determination of BAC and VAC equal amounts of the two specimens must be analyzed.

In the current forensic practice, it is necessary to identify a method of calculating BAC from alternative biological sample in cases where blood samples are not available or are corrupted by postmortem processes, trauma, or embalming [12, 13].

Data analysis by linear regression allowed the examination of the influence of two types of parameters on the concentration of alcohol in blood, urine and vitreous humor:

- Individual parameters: age, postmortem interval (PMI), blood collection site, sex.

- Environmental factors: temperature (minimum value, maximum, average- measured in degrees Celsius), atmospheric pressure (average values measured in mmHg), dew point average (measured in degrees Celsius), average relative humidity, average rainfall, apparent temperature (temperature-humidity index- THI based on the relationships identified by Carl Schoen [14]). Only those values (minimum, maximum and/ or average) within the postmortem interval registered for each case (in order to have a correct reference of postmortem processes) were considered and included in the statistical processing.

In the 85 cases where it was possible to determine the alcohol concentration in both blood and vitreous humor, there was a strong dependence of VAC to BAC ($p < 0.000001$) and a moderate dependence of BAC to PMI ($p = 0.011$). For all other parameters, individual or environmental, statistical significance was much lower, which is why they were not taken into account for further analysis. Applying linear regression, using the selected parameters, the following formula is obtained:

VAC [g/ l] = 0.901 • BAC [g/ l] - 0.0105 • PMI [h] + 0.5585 (1)

with $p < 0.000001$ (BAC), $p = 0.011$ (PMI), $p = 0.0004$ (constant); Linear model $R2 = 0.815$.

Analysis of the alcohol concentration in the vitreous humor and urine (36 cases) showed a strong dependence of the VAC to UAC ($p < 0.00001$) and a moderate dependence of the VAC to the average postmortem temperature ($p = 0.016$), maximum postmortem temperature ($p = 0.014$) and the mean postmortem atmospheric pressure ($p = 0.005$). All other parameters, including PMI had a lower significance. Applying linear regression using the selected parameters, the following formula resulted:

VAC[g/l] = 0.795•UAC[g/l] + 0.108•Taverage[°C] – 0.094•Tmax[°C] + 0.046•Paverage[mmHg] 34.479 (2)

with p < 0.00001 (UAC), p = 0.016 (Taverage), p = 0.014 (Tmax), p = 0.005 (Paverage), p = 0.006 (constant). Linear model R2 = 0.839.

Equation 2 identified by us to calculate the VAC from UAC and environmental factors (temperature and atmospheric pressure), was developed from a small number of cases, suggesting the need to extend the research on a larger number of cases. Also, the use of environmental factors should be approached cautiously, since outdoor weather data do not always correspond to the environment where the body is placed till the autopsy is performed.

Inverse linear regression allowed the identification of the following relationship between BAC, VAC and PMI:

BAC[g/l] = 0.903•VAC[g/l] + 0.0084•PMI [h] – 0.150 (3)

In the above relation, the p constant is not statistically significant (p = 0.357) leading to a high degree of uncertainty regarding the results and influencing the possible use of the PMI (statistically significant p = 0.042) to estimate the overall effect the PMI on the BAC (with an increase of 0.0084 g/hour).

The relationship between the BAC, UAC, temperature and pressure obtained by the linear regression is:

BAC[g/l] = 0.856•UAC[g/l] + 0.054•T[°C] – 0.031 • Tmax [°C] + 0.024•Paverage[mmHg] – 18.110 (4)

Linear regression in the above equation denotes the same influence of the atmospheric pressure and temperature on the urinary excretion process; only the UAC (p <0.00001) and the temperature (p = 0.021) coefficients are significant, others are borderline insignificant (p= 0,084-0,087).

In most cases, the calculation of the VAC from UAC and/ or BAC is not necessary because the reference in terms of somatic and psychological effects of the ethanol is the BAC [15, 16]. However, as showed above, the accurate assessment of the postmortem BAC is sometimes difficult because of the influence of various factors [17-19].

Literature states [11] that the advantage of the VAC over the BAC is the fact that the vitreous is less exposed to bacterial contamination, especially in cases where the body was subjected to processes of decomposition or severe traumatic injuries.

Studies in the literature correlate mainly VAC with BAC, but also UAC with BAC, based on the results of toxicological analysis performed at the time of autopsy which allows approximation with some margin of error, the value of the alcohol at the time of death which is relevant from the forensic perspective [5]. However, in some cases vitreous humor can not be analyzed (such as trauma to the eyes, degradation of the eye due to putrefaction, etc.).

If these situations overlap the possible elements of influencing the real value of the BAC (e.g. decomposition, severe trauma, embalming), toxicology has limited value because the possible changes of the BAC due to the previously mentioned factors can not be verified.

For these situations in which the vitreous humor can not be collected and the BAC is suspected to be altered by factors that acted postmortem on the body we propose the application of the equation 1 identified in this study for estimating the VAC at the time of death based on the BAC at the time of autopsy and the postmortem interval. Considering that the concentration of the ethanol in the vitreous humor is constant, we estimate this value as the one at the time of death or about 1-2 hours prior to death. Further, considering the VAC as a descriptor of the BAC at the time of death, by applying the theoretical VAC/ BAC ratio we obtain the following relationship:

VAC [g/l]= (1,12-1,2)*BAC0[g/l].

By applying this ratio in equation 1 we can estimate the blood alcohol concentration at the time of death as being included in the range:

0,0804*BAC1-0,009*PMI (h)+0,498 / 0,75*BAC1-0,008*PMI (h)+0,465 (5)

where BAC1 is the value of the blood alcohol concentration at the time of autopsy.

Assuming constant VAC (equation 5), according to the equations (1) and (2) we can estimate the influence of various parameters on the concentration of ethanol (Table 4). The last column shows conditions (individual

Table 4. The influence of the measured parameters on BAC and UAC .

Measured parameters	Influence factors	The sense of influence	Amount	Circumstances of validity
BAC [g/l]	Postmortem interval	increase	+ 0.012 g/l/h	PMI = 26.9 ± 13.1 h
UAC [g/l]	Average temperature*	decrease	- 0.136 g/l/ °C	$T_{average}$ = 10.7 ± 11.8 °C
	Maximum temperature*	increase	+ 0.118 g/l/ °C	T_{max} = 17.4 ± 13.5 °C
	Average atmospheric pressure*	decrease	- 0.058 g/l/mmHg	$P_{average}$ = 764.2 ± 5.7 mmHg

*in PMI

and environmental) in which measurements were made and represents the limit of validity of the detected influences.

CONCLUSIONS

Our study demonstrated a strong correlation between the concentration of ethanol in blood, urine and vitreous humor. VAC correlates with BAC stronger than UAC.

The VAC/ BAC ratio determined in our study using the Cordebard method for determining the concentration of ethanol in blood and vitreous humor falls within the ranges provided in the literature. This allows us to conclude that the Cordebard method (cheap and accessible) can be applied to determine the VAC, a proper comparison between BAC and VAC requiring the analysis of equal amounts of biological samples.

Also, our study allowed the identification of a method for calculation of BAC at the time of death from BAC at the time of autopsy. This method could be useful in situations where BAC is suspected of distortion due to postmortem factors (decomposition, severe trauma, embalming) and the vitreous humor can not be collected.

In line with similar studies in the literature our study suports the idea that harvesting as many biological samples as possible is mandatory for a good quality toxicological analysis and for a proper interpretation of its results.

References

1. Kaye S, Cardona E. Errors of converting a urine alcohol value into a blood alcohol level. The Am J of Clin Pathol. 1969 Nov; 52(5):577-584.
2. DiMaio VJ, DiMaio D. Forensic Pathology 2nd ed: CRC Press LLC; 2001.
3. Spitz WU, Spitz DJ. Spitz and Fisher's Medicolegal Investigation of Death 4th ed: Charles C Thomas Publisher LTD; 2006.
4. Molina DK. Handbook of Forensic Toxicology For Medical Examiners: CRC Press; 2010.
5. Papierz P, Berent J, Markuszewski L, Szram S. A comparative study of the ethyl alcohol concentration in vitreous humor in relation to ethyl alcohol concentration in blood and urine. Problems of Forensic Sciences. 2004; LVIII: 34–44.
6. Finkbeiner WE, Ursell PC, Davis RL. Autopsy Pathology A Manual and Atlas 2nd ed: Saunders; 2009.
7. Waters BL. Handbook of Autopsy Practice 4th ed: Humana Press; 2009.
8. Knight B, Saukko P. Knight's Forensic Pathology 3rd ed: Edward Arnold LTD; 2004.
9. Jones A, Holmgren P. Uncertainty in estimating blood ethanol concentrations by analysis of vitreous humour. J Clin Pathol. 2001 Sept; 54(9): 699–702.
10. Chao TC, Lo DS. Relationship between postmortem blood and vitreous humor ethanol levels. Am J Forensic Med Pathol. 1993 Dec; 14(4): 303-308.
11. Kugelberg FC, Jones AW. Interpreting results of ethanol analysis in postmortem specimens: a review of the literature. Forensic Sci Int. 2007 Jan; 165(1): 10-29.
12. Kala M, Chudzikiewicz E. Influence of Post-Mortem Changes in Biological Material on Interpretation of Toxicological Analysis Results. Problems of Forensic Sciences. 2003; 54: 32-59.
13. Payne-James J, Byard R, Corey T, Henderson C. Encyclopedia Of Forensic And Legal Medicine. Hardbound; 2005.
14. Schoen C. A New Empirical Model of the Temperature–Humidity Index. J. Appl. Meteor. 2005 Sept; 44(9): 1414-1420.
15. Jones AW. Reference limits for urine/blood ratios of ethanol in two successive voids from drinking drivers. J Anal Toxicol. 2002 Sep; 26(6): 333-339.
16. Honey D, Caylor C, Luthi R, Kerrigan S. Comparative alcohol concentrations in blood and vitreous fluid with illustrative case studies. J Anal Toxicol. 2005 Jul-Aug; 29(5): 365-369.
17. Pounder D. Dead sober or dead drunk?. BMJ. 1998 Jan; 316(7125): 87.
18. Athanaselis S, Stefanidou M, Koutselinis A. Interpretation of postmortem alcohol concentrations. Forensic Sci Int. 2005 May; 149(2-3): 289-291.
19. Sylvester PA, Wong NA, Warren BF, Ranson DL. Unacceptably high site variability in postmortem blood alcohol analysis. J Clin Pathol. 1998 March; 51(3): 250–252.

Rom J Leg Med 15 (3) 229–233 (2007)

Procesarea asistată de calculator a recalculării alcoolemiei

Simona Irina Damian[1], L. V. Constantin[2], R. F. Damian[3]

Abstract: Computer aided processing of the blood alcohol level back calculation. The back calculation of the blood alcohol concentration (BAC) is complicated enough to suggest computer aided processing. Often in a single case the calculus must be repeated numerous times, for multiple declarations, or for multiple variations of some parameters (in the case of uncertainty in the placement of the computed BAC in relation with the legal limit).

A computer software is presented that makes automatic processing of the data based on classical or improved pharmacological modeling, the results being printed on screen or as a standard report on paper.

First the Widmark equation is used for BAC computation: $C=A/rG-\beta t$ where A is the amount of alcohol consumed [grams], r is the Widmark factor, G is the body weight [kg], β is the rate at which BAC falls [grams/l/h].

The value of the Widmark factor permits the computation of the total body water (TBW) and depends primarily on the sex, height and age of the subject. Multiple statistical determination of the factor were performed over time, in this paper we show typical values and variations mentioned by different references (Widmark, Dubovski) and also different results for the alcohol elimination rate (Widmark, Alha, Dubovski, Schwietzer). The Body Mass Index (BMI - Forrest) and age (Watson) are taken into account, as is the chemical analysis error. The original computer software is presented, showing its performances (especially the possibility to take into account multiple parameters: absorption rate, elimination rate, stomach content), better conditions for fast legal answers being obtained.

Keywords: Computer software, Blood alcohol concentration, Widmark

Procedura de calculare a alcoolemiei este suficient de laborioasă pentru a sugera procesarea automatizată, cu ajutorul calculatorului. Deseori, pentru un singur caz, calculul trebuie facut pentru multiple variante de consum declarat, sau trebuie repetat pentru parametrii extremi (în cazul incertitudinii plasării punctelor de interes în raport cu limita legală). De asemenea anumiți parametri care nu întotdeauna sunt cunoscuți din datele de anchetă (cum ar fi de exemplu starea de plenitudine a stomacului subiectului) influențează destul de mult, uneori chiar decisiv, rezultatele finale.

Sunt de interes dar greu de realizat fără ajutorul procesării computerizate, şi anumite prelucrări statistice relativ la erorile acceptate ale măsurătorilor chimice ale alcoolemiei sau relativ la abaterea acceptată prin reglementări față de limita legală.

1) Asist. Univ. Dr., Universitatea de Medicină şi Farmacie Gr. T. Popa, medic specialist medicină legală IML Iaşi
2) chimist principal IML Iaşi
3) S.C. RF Technologies S.R.L. Iaşi, cercetător ştiințific dr. ing. Universitatea Tehnică Gh. Asachi Iaşi, http://www.rftech.ro, contact: office@rftech.ro

Metodă de lucru

Calculul retroactiv al alcoolemiei se bazează pe utilizarea modelului farmaco-cinetic de ordinul I [1],[2] care presupune o rată constantă de absorbție în timp a alcoolului şi o rată constantă de eliminiare prin metabolizare. Relația de calcul a variției in timp a alcoolemiei în sânge este cunoscută sub numele de relația Widmark, folosită în acest scop in majoritatea țărilor lumii [3].

În faza de absorbție se presupune o creştere constantă în timp a alcoolemiei spre valoarea maximă, perioada de absorbție fiind cuprinsă între 30 min. şi 2-3 ore, depinzând în special de ingestia simultană sau anterioară a hranei [4].

În faza de eliminare se utilizează relația Widmark de variație în timp a concentrației de alcool în sânge:

$$C = \frac{A}{r \cdot G} - b \cdot t \qquad (1)$$

unde A este cantitatea de alcool pur consumată (g), r este factorul Widmark, G este greutatea corporală, β este rata individuală de eliminare a alcoolului (g‰/h).

Valorile factorului Widmark (care oferă conținutul de apă al corpului uman) depind în primul rând de sexul subiectului [5], înălțime, vârstă, etc. şi au existat diferite măsurători statistice pentru determinarea sa. Astfel autorii indică valorile tipice şi variațiile:

- Widmark: 0.68 (0.51÷0.85) – bărbați, 0.55 (0.44÷0.66) – femei
- Dubovski: 0.73 (0.60÷0.87) – bărbați, 0.66 (0.54÷0.85) – femei.

Pentru rata de eliminare a alcoolului valorile obținute sunt următoarele:

- Widmark: 0.15 (0.10÷0.24) g/l/h
- Alha: 0.13 (0.07÷0.24) g/l/h
- Dubovski: 0.14 (0.06÷0.22) g/l/h
- Schwietzer: 0.20 (0.10÷0.30) g/l/h

Factorul Widmark depinde în primul rând de conținutul de grăsime al corpului uman, ca atare are variații semnificative cu sexul (lucru luat în considerare de valorile amintite), dar depinde puternic şi de constituția corporală a subiectului (care se poate aprecia utilizând indicele de masă corporală – Body Mass Index: $BMI = \frac{G}{H^2}$) . Acest lucru este luat în considerare de Forrest [6] care oferă o posibilitate de determinare a factorului Widmark plecând de la dimensiunile de gabarit ale subiectului. Relațiile stabilite de Forrest nu iau în considerare însă efectul vârstei subiectului care are totuşi un efect important, mai ales în cazul bărbaților, la care cantitatea de grăsime din organism creşte cu vârsta, la aceeaşi conformație corporală. Aceste efecte sunt luate în considerare în relațiile determinate de Watson [7].

Rata de eliminare poate fi determinată precis dacă se pot realiza două măsurători sanguine distanțate cu o perioadă de cel puțin o oră. Dacă aceste măsurători nu există sau dacă se situează pe panta ascendentă a alcoolemiei se folosesc valorile tipice ale ratei de eliminare.

$$b = \frac{C(t_2) - C(t_1)}{t_2 - t_1} \qquad (2)$$

Rezultate

Un program de calcul a fost realizat pentru efectuarea calculelor prezentate anterior şi a afişării rezultatelor. Interfața prietenoasă vine în ajutorul utilizatorului pentru introducerea datelor subiectului, datelor de anchetă şi testare sanguină, a listei de consum (fig. 1). Se obține foarte rapid variația în timp a concentrației de alcool în sânge a subiectului cu evidențierea punctelor importante (fig. 2).

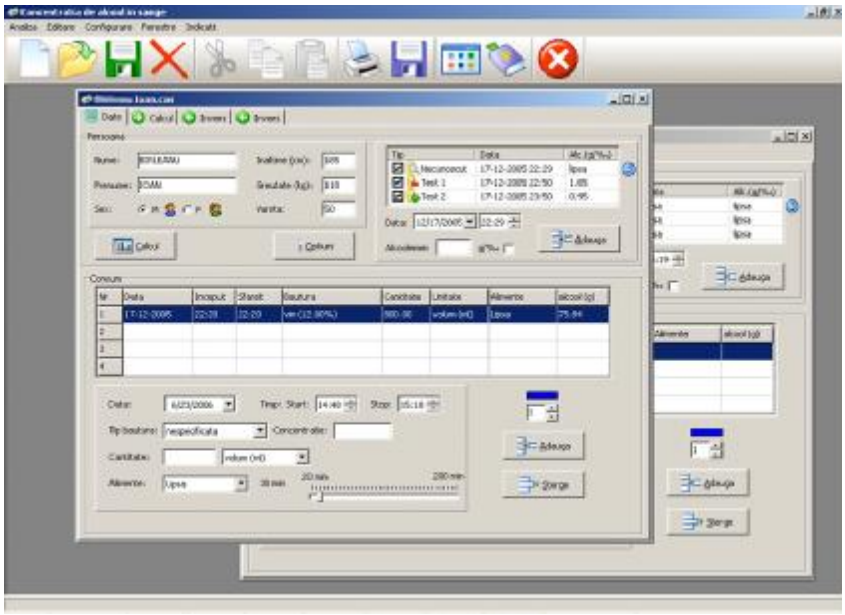

Fig. 1 Interfața de introducere a datelor

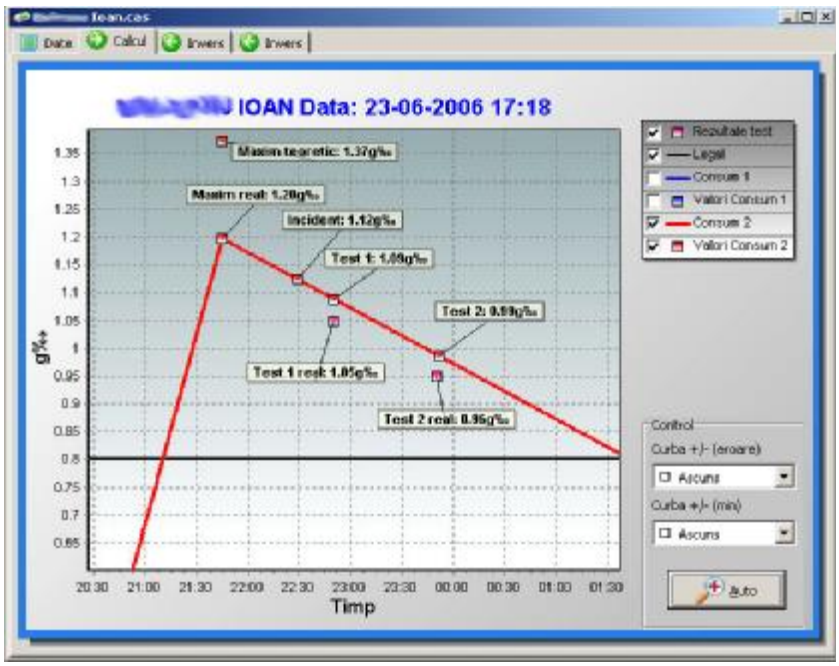

Fig. 2 Trasarea curbei de variație în timp a alcoolemiei

Pentru uşurarea obţinerii concluziilor, programul permite calculul simultan şi comparaţia între mai multe variante de consum, de asemenea compararea cu valoarea limită legală (fig. 3) dar şi reprezentarea variaţiilor tipice utilizate în metoda de determinare (factorul de veridicitate de ±20%, variaţia plenitudinii stomacului, etc) – fig.4.

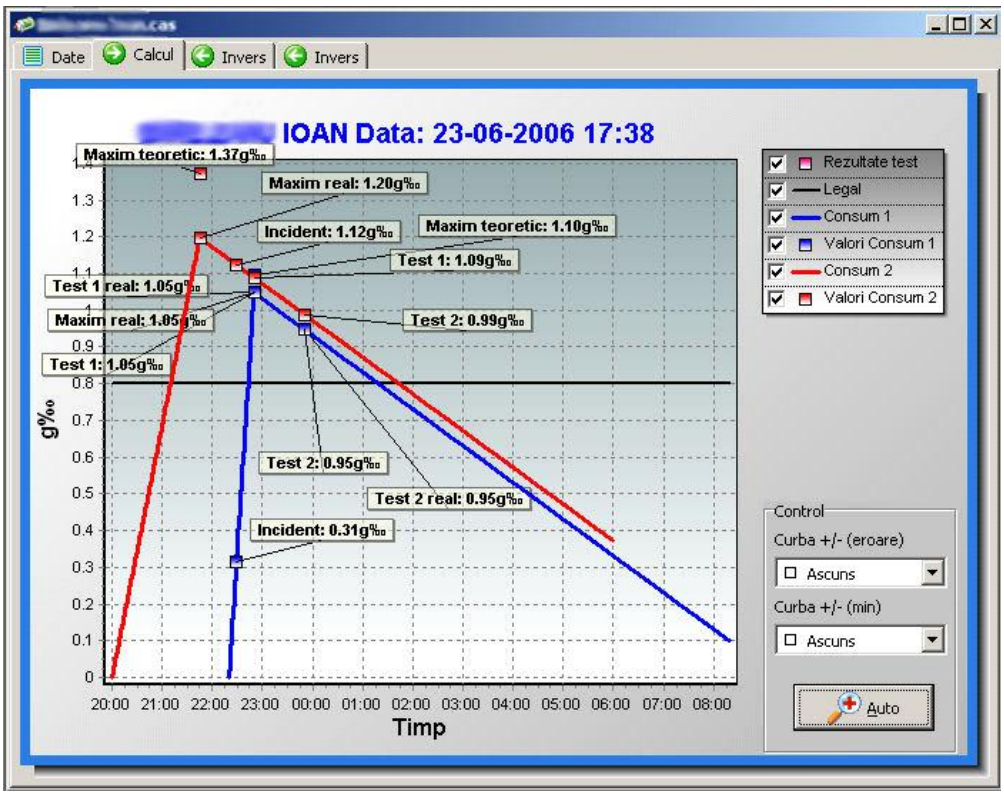

Fig. 3 Comparaţie între diverse declaraţii de consum

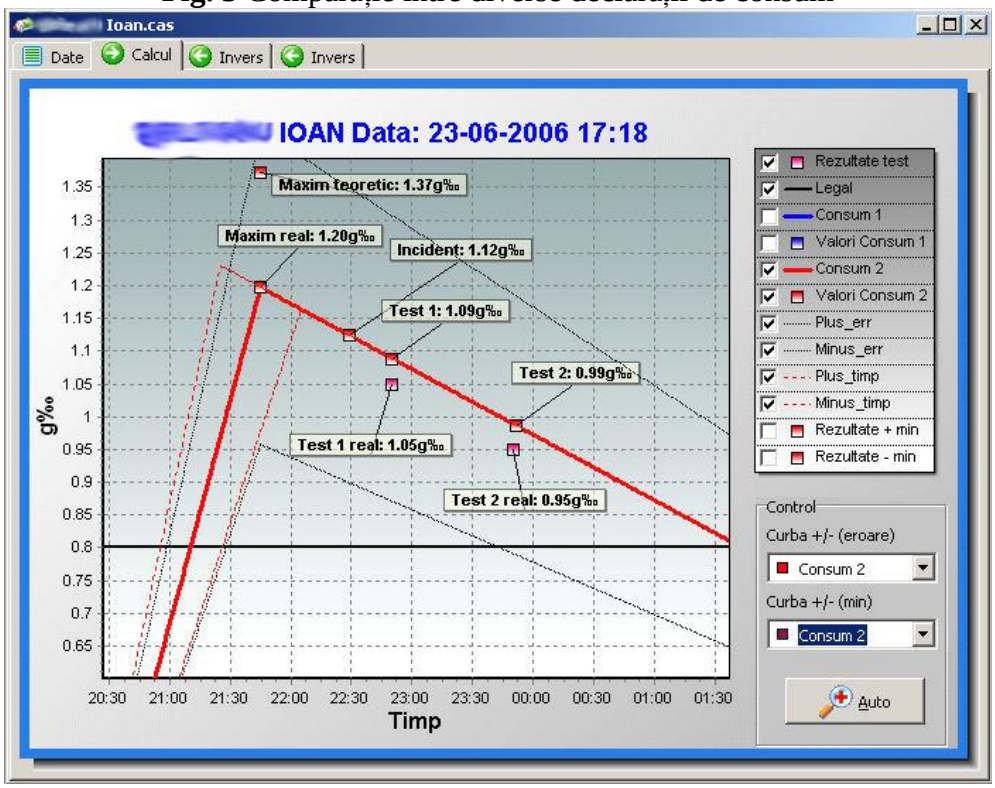

Fig. 4 Evidenţierea abaterilor maxime posibile

Concluzii

Se prezintă un program de calcul care preia o mare parte din dificultatea realizării analizelor multiple pentru recalcularea alcoolemiei, permițând realizarea comodă, şi mai ales rapidă, a tuturor calculelor prezentate.

Abaterea maximă posibilă e reprezentabilă pentru diverşi parametri variabili: rată de absorbție, de eliminare, conținutul stomacului, erorile măsurătorilor chimice etc. fiind realizate astfel condiții mai bune de interpretare legală rapidă a rezultatelor, micşorând probabilitatea de apariție a unor expertize afectate de abaterile diverşilor parametri.

Bibliografie

1. J. Siegel G. Knupfer P. Saukko, Encyclopedia of Forensic Sciences, 2000, Elsevier, 74-126
2. E. Hodgson, A textbook of modern toxicology, 2004 by John Wiley & Sons, 80-85
3. U.S. Department of Transportation, National Highway Traffic Safety Administration, Computing a BAC Estimate, 1994.
4. K. Millar R.H. Hammersley F. Finnigan, Reduction of alcohol-induced performance impairment by prior ingestion of food, British Journal of Psychology (1992), 83, 261-278.
5. W. Gubala D. Zuba, Gender differences in the pharmacokinetics of ethanol in saliva and blood after oral ingestion, Pol. J. Pharmacol., 2003, 55, 639-644
6. A. D. Barbour, Simplified Estimation of Widmark "r" Values by the Method of Forrest, Science & Justice 2001; 41(1): 53-54
7. B. M. Kapur, Cbac: Computerised blood alcohol concentration - a computer model as a clinical and an educational tool, Ann. Biochim. Clin. Qué. 30(2):36-39, 1991.

EFFICIENCY AND CONVERGENCE OF THE WAVE CONCEPT ITERATIVE PROCEDURE

Radu-Florin Damian
Irinel Casian Botez
Facultatea de Electronica
Technical University Iasi, Romania
Bd. Carol I, nr. 11, Iasi, 700506
E-mail: rdamian@etc.tuiasi.ro

Romeo-Cristian Ciobanu

Facultatea de Electrotehnica
Technical University Iasi, Romania
Bd. Dimitrie Mangeron, nr. 51- 53
Iasi, 700050, Romania

KEYWORDS

Wave Concept Iterative Procedure, iterative methods

ABSTRACT

In some electromagnetic iterative methods, the convergence to the solution is slow and the stable solution is not always found. The present paper describes three methods used to improve the speed and the stability of the convergence process for the Wave Concept Iterative Procedure (WCIP). Two of these methods are not directly related to the electromagnetic fields computation and can be used in other iterative computing procedures as well.

I. INTRODUCTION

In (Azizi et al. 1995; Azizi et al. 1996) the Fast Wave Concept Iterative Process (FWCIP) is introduced. It relies on the definition of transverse waves based on the tangential electric and magnetic fields on some active surface. The same (essentially) method is denoted in literature as FWCIP (Azizi et al. 1995), Transverse Wave Formulation - TWF (Wane et al. 2005) and more recently Wave Concept Iterative Procedure - WCIP (Baudrand et al. 2007, Raveu et. al 2007).

WCIP compares favorably (Wane and Bajon 2006) with other commercially available software regarding the precision and promises better performance in computation efficiency in structures with very different layer heights.

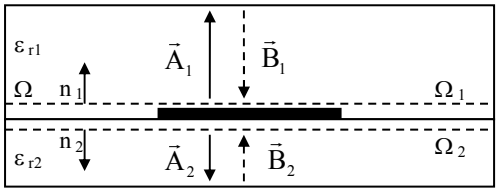

Figure 1: Wave Concept Iterative Procedure Definitions

Let Ω be a discontinuity plane inside a metallic box (figure 1). The regions on both sides are filled with homogenous dielectric. The two regions are designated as region 1 (ε_{r1}, h_1, etc.) and region 2 (ε_{r2}, h_2, etc.).

Let Ω_i be a surface infinitely close to Ω in region i, n_i the unit vector normal to Ω and directed into region i, i = 1 or 2.

We define the transverse incident and reflected wave in Ω_i (1):

$$\vec{A} = \frac{1}{2\sqrt{Z_{0i}}}\left(\vec{E} + Z_{0i}\vec{J}\right), \vec{B} = \frac{1}{2\sqrt{Z_{0i}}}\left(\vec{E} - Z_{0i}\vec{J}\right) \quad (1)$$

The waves are subject to constraints imposed by the discontinuity (2) and by the reflection over the metallic walls of the box (3).

$$\vec{A} = \hat{\Gamma}_{\Omega}\vec{B} + \vec{A}_0 \quad (2)$$

$$\vec{B} = \hat{\Gamma}\vec{A} \quad (3)$$

A_0 is the incident wave generated by the source in the two regions and $\hat{\Gamma}_{\Omega}, \hat{\Gamma}$ denotes the reflection operator on the discontinuity surface Ω and on the metallic walls respectively. The WCIP method solves (2) (3) by an iterative procedure. In (4), (5) *k* denotes the current iteration and the starting conditions are imposed by the source (6).

$$\vec{A}^{(k+1)} = \hat{\Gamma}_{\Omega}\vec{B}^{(k)} + \vec{A}_0 \quad (4)$$

$$\vec{B}^{(k)} = \hat{\Gamma}\vec{A}^{(k)} \quad (5)$$

$$\vec{A}^{(0)} = \vec{A}_0 \quad (6)$$

Equation (2) is applied in the space domain, while (3) is easily implemented in the modal domain, so a fast modal transform (FMT), based on FFT (N'gongo and Baudrand 1999), can be developed in order to go from (4) to (5) and vice versa through the iterative procedure.

While this method found its best applications in the analysis of microwave multilayer structures (Akatimagool et al. 2001, Wane et al. 2005, Wane and Bajon 2006), it has been also successfully applied to cylinders (Raveu et al. 2004) and photonics (Azizi et al. 2008)

The WCIP has some convergence problems, even in simplest structures. In the following example, we show the results found for a microstrip transmission line, extending from one side of the box to another. The box

Proceedings 23rd European Conference on Modelling and Simulation ©ECMS Javier Otamendi, Andrzej Bargiela, José Luis Montes, Luis Miguel Doncel Pedrera (Editors)
ISBN: 978-0-9553018-8-9 / ISBN: 978-0-9553018-9-6 (CD)

is rectangular (a by b), divided by a uniform grid in 32 by 32 pixels. The dimensions are: a = 17mm; b = 17mm; $\varepsilon_{r1} = 1$; $h_1 = 1000$mm; $\varepsilon_{r2} = 10$; $h_2 = 1.5$mm. The line is 2 pixels wide (1.06mm) (figure 1) and of course short-circuited at the end by the box, so purely imaginary impedance is expected. The convergence is verified by plotting the impedance value on the source surface (figure 2).

Figure 2 show that 150 iterations are required to obtain the "convergence" but some big enough oscillations still remain, for the real part around 0, for the imaginary part around -170Ω. These curves show that a real convergence is not reached in 400 iterations and will not be reached, even with more iterations, thus the used algorithm suffers from certain instability. Figure 3 shows the computed fields on the discontinuity plane. The shape of the y direction current J_y clearly shows the instability. Investigation of other fields through the iterations shows little variation in shape and values.

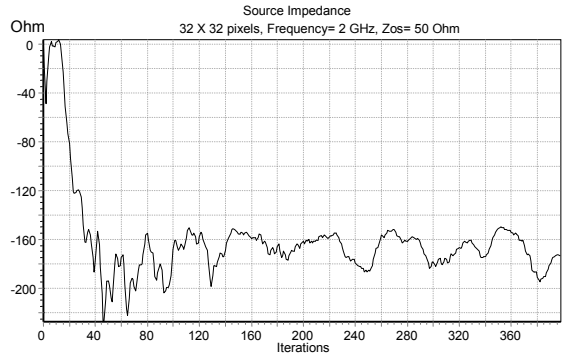

Figure 2: Input Impedance - Convergence Analysis

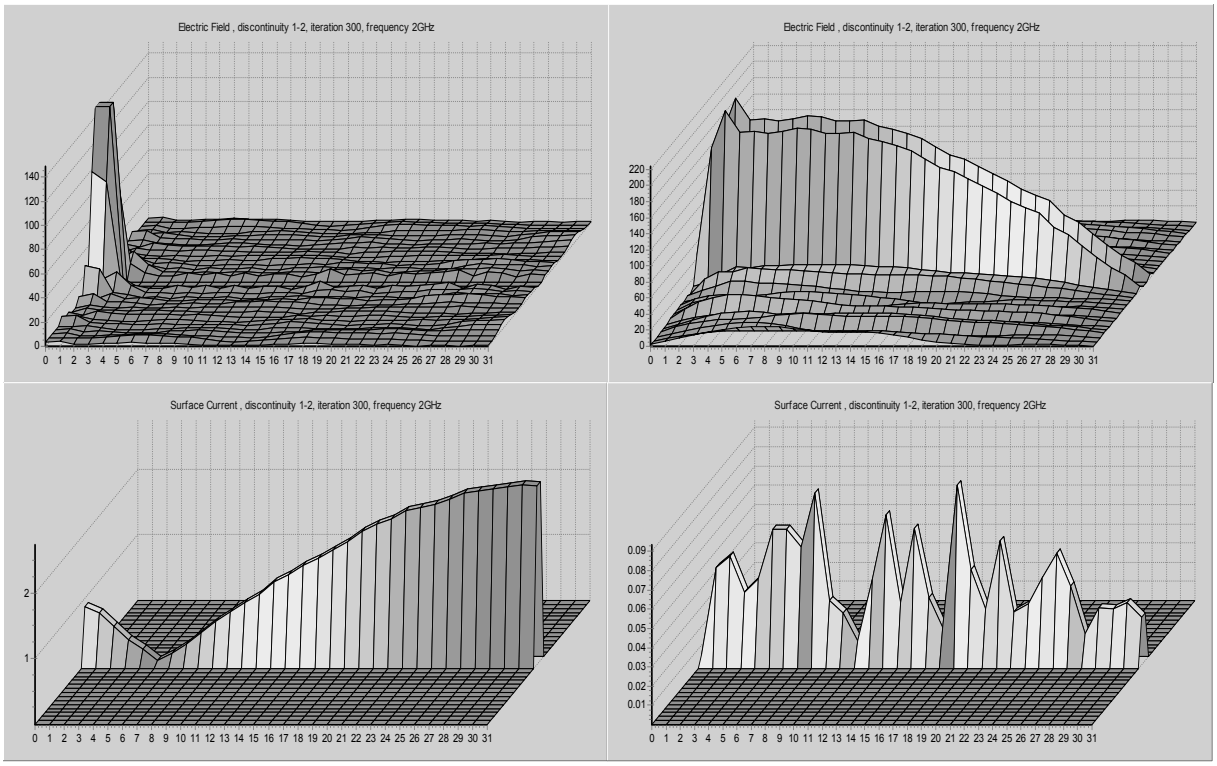

Figure 3: Original WCIP fields: E_x, E_y (up), J_x, J_y (down)

II. ITERATIVE PROCEDURE IMPROVEMENT TECHNIQUES

We will model the WCIP iterative numerical problem as a discrete in time system. We have an input (the source) and an output: the variation in "time" (read iterations) of the desired quantities (field values, impedances etc.). We will be able to use systems theory in order to insure the WCIP convergence (discrete in time system stability) as in (Smith 1999). As shown in figure 4 we obtain a feedback discrete system, which, as is well known, might have in some cases stability problems.

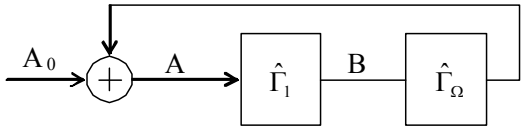

Figure 4: Iterative Procedure as a Feedback Discrete System

Source modification technique

A step variation source as in (6) will excite high "frequency" oscillations in the solution. A source with a slow variation in time (measured in iterations) will

eventually solve the instability problem, thus offering the desired convergence. From spectral windowing techniques (Nuttall 1981; Lyons 1998), we choose a Blackman-Harris window for its reduced high frequencies contents, decreasing the amplitude of the oscillations.

$$\vec{A}_0^{(k)} = \begin{cases} \left[a_0 + a_1 \cos\left(\frac{\pi k}{k_0}\right) + a_2 \cos\left(\frac{2\pi k}{k_0}\right) + \right. \\ \left. \quad + a_3 \cos\left(\frac{3\pi k}{k_0}\right) \right] \cdot \vec{A}_0; & k \le k_0 \\ \vec{A}_0; & k > k_0 \end{cases} \tag{7}$$

$$\begin{cases} a_0 = 0.3558;\ a_1 = -0.4874; \\ a_2 = 0.1442;\ a_3 = -0.0126; \end{cases} \tag{8}$$

As in (7) with optimal parameters in (8), we increase the source gradually for k_0 iterations before reaching the desired value A_0. Figure 5 shows the results. In both cases, the final value is almost the same, and we decrease the oscillations. The effect is more obvious for larger k_0 (b) with the expense of the convergence rate. Larger k_0 means lower high frequency content in the source, which implies as we see lower oscillations in the response.

Figure 6 shows the fields on the discontinuity plane. The amplitude of the tangential line current is the smallest, so where only noise (oscillations) appeared before in figure 3 now we have a distinct (modal) shape in figure 6. The tangential current in the line is very small but not zero, as we defined the unknown fields in the middle of the pixel. A closer inspection of all the fields show "cleaner" shapes for all the other fields (longitudinal electric field shown in figure 6): the smaller oscillations in the convergence curve imply smaller oscillations in all the field values.

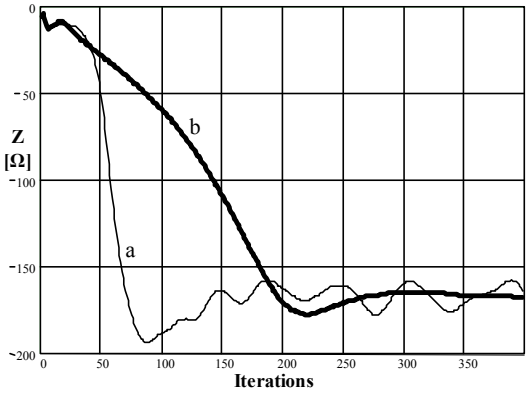

Figure 5: Blackman-Harris Source
a) $k_0 = 50$; b) $k_0 = 200$

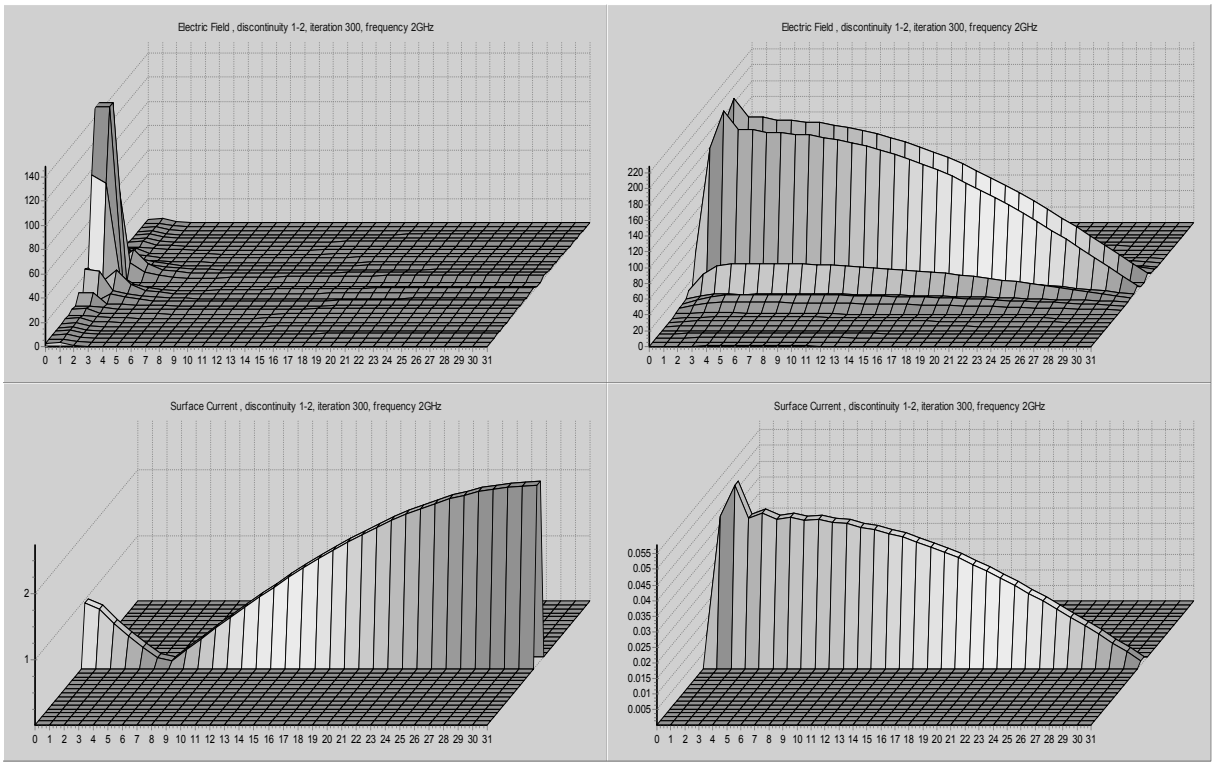

Figure 6: Blackmann-Harris Source/Modified Structure Fields: E_x, E_y (up), J_x, J_y (down).

Structure modification technique

Another approach is to modify the surface reflection operator. In (4) the surface reflection takes different values for the metal, dielectric and surface impedance. To ensure a smoother convergence we will try to make a soft transition between the different materials, at least until the field reaches a "good enough" value, after

which we can return to the physics related surface reflection in order to obtain the correct solution.

We will adopt definition (9) for the surface reflection operator:

$$\hat{\Gamma}_{\Omega}^{(S)} = \alpha(k)\cdot\hat{\Gamma}_{\Omega}^{(S)} + [1-\alpha(k)]\cdot\frac{\hat{\Gamma}_{\Omega}^{(M)} + \hat{\Gamma}_{\Omega}^{(D)}}{2} \qquad (9)$$

The transition function α will increase gradually from 0 to 1 in k_0 iterations in order to obtain a smooth transition. $\hat{\Gamma}_{\Omega}^{(S)}$ (S - denotes the surface type: D=dielectric, M=metal, Z=surface impedance) will gradually change from the first iterations when we have a homogenous discontinuity (no transition between materials), to the correct values for the surface reflection in k_0 iterations. Various functions can be used but the experience shows that a suitable function must raise fast enough after k=0 in order to improve the convergence rate and also to have a slow variation when approaching k_0 to prevent oscillations. We use function (10) with different values for n to obtain fast convergence and low oscillations.

$$\alpha(k) = \begin{cases} 1-\left(1-\dfrac{k}{k_0}\right)^n & k \le k_0 \\ 1 & k > k_0 \end{cases} \qquad (10)$$

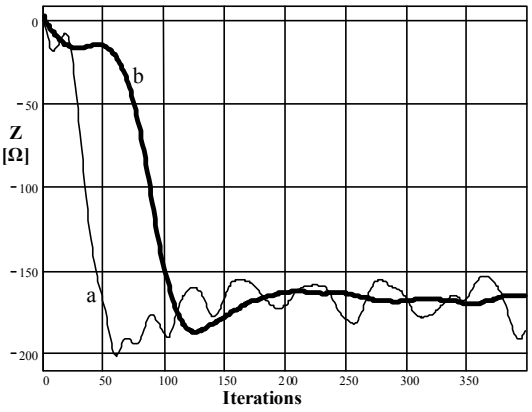

Figure 7: Modified Surface Reflection, n = 8. a) k_0 = 50; b) k_0 = 200

Figure 7 shows the results obtained for the same test structure, using the transition function (10) for n = 8. The final fields are identical to those in figure 6 and will not be plotted again. The conclusions are similar to those from the Blackman-Harris source: larger k_0 decrease the oscillations but increase the convergence time while the n parameter has an opposite effect.

III. MODIFIED WAVE DEFINITION

In the previous section, we investigated two methods that can be used in any iterative procedure to improve the convergence, but those methods, while offering a better convergence and a better field solution, only lowers the intrinsic instability of the WCIP method.

Some changes are to be made inside the method itself. In WCIP many of the concepts are physics related and cannot be changed. The only place where we imposed some of the parameters is the definition of the waves where we chose a space domain definition (1). The value of the impedance was chosen equal to that of the corresponding medium (11).

$$Z_{0i} = \sqrt{\frac{\mu_0}{\varepsilon_i}}\ ,\ \forall i = 1,2 \qquad (11)$$

This value is not imposed by any physical constraints so in principle it can be changed. This approach has not shown an improvement in the convergence procedure so it seems that the only adjustable parameter will not give us the means to stabilize the system.

Modal domain definition of the waves

We will try to define the waves in the modal domain. For every region, we state the modal decomposition:

$$\begin{cases} A_{mn} = \dfrac{1}{2\sqrt{Z_{0mn}}}\left(V_{mn} + Z_{0mn}\cdot I_{mn}\right) \\ B_{mn} = \dfrac{1}{2\sqrt{Z_{0mn}}}\left(V_{mn} - Z_{0mn}\cdot I_{mn}\right) \end{cases} \qquad (12)$$

$$\begin{cases} \vec{A} = \sum_{mn} A_{mn} f_{mn}\ ; \quad \vec{B} = \sum_{mn} B_{mn} f_{mn} \\ \vec{E} = \sum_{mn} V_{mn} f_{mn}\ ; \quad \vec{J} = \sum_{mn} I_{mn} f_{mn} \end{cases} \qquad (13)$$

where: $i = \overline{1,M}\ ; j = \overline{1,N}\ ; M = 2^m\ ; N = 2^n$ and Z_0 becomes a matrix resulting in a different impedance value for every spatial mode: Z_{0mn}.

As seen from (4) the surface reflection operator needed in order to apply WCIP is localized so cannot be conceived in modal domain and its value relies on a constant value of the impedance. As a first impression, definitions (12)-(13) are not possible. We can yet find a method to decouple the modes. First, we write the iterative procedure from (4)-(6):

$$\vec{A}^{(k+1)} = \hat{\Gamma}_{\Omega}\cdot FMT^{-1}\left(\hat{\Gamma}\cdot FMT\left(\vec{A}^{(k)}\right)\right) + \vec{A}_0 \qquad (14)$$

The surface reflection operator takes different values depending on the surface type.

$$\hat{\Gamma}_{\Omega}(x,y) = H_M(x,y)\cdot\hat{\Gamma}_{\Omega}^{(M)} + H_D(x,y)\cdot\hat{\Gamma}_{\Omega}^{(D)} + H_Z(x,y)\cdot\hat{\Gamma}_{\Omega}^{(Z)} \qquad (15)$$

$$H_M(x,y) = \begin{cases} 1 & \text{on the metal} \\ 0 & \text{elsewhere} \end{cases} \qquad (16)$$

In the same way as in (16) we define the localization function for the dielectric and for the lossy dielectric.

We can see that the spatial variables x and y appear only in the localization functions and not in the specific surface operator. Thus, we can move these operators inside the Inverse FMT, in fact moving the surface reflection in the modal domain.

$$\vec{A}^{(k+1)} = H_M(x,y)\cdot \vec{A}_M^{(k)} + H_D(x,y)\cdot \vec{A}_D^{(k)} + H_Z(x,y)\cdot \vec{A}_Z^{(k)} + \vec{A}_0 \quad (17)$$

$$\vec{A}_M^{(k)} = \hat{\Gamma}_\Omega^{(M)}\cdot FMT^{-1}\left(\hat{\Gamma}\cdot FMT\left(\vec{A}^{(k)}\right)\right) \quad (18)$$

$$\vec{A}_D^{(k)} = \hat{\Gamma}_\Omega^{(D)}\cdot FMT^{-1}\left(\hat{\Gamma}\cdot FMT\left(\vec{A}^{(k)}\right)\right) \quad (19)$$

$$\vec{A}_Z^{(k)} = \hat{\Gamma}_\Omega^{(Z)}\cdot FMT^{-1}\left(\hat{\Gamma}\cdot FMT\left(\vec{A}^{(k)}\right)\right) \quad (20)$$

We find every particular solution (18)-(20) with the hypothesis that the discontinuity plane is homogenous: all metallic (18) or all dielectric (19) or all lossy dielectric (20). Then we find the correct solution (17) choosing for every pixel in the grid the corresponding value.

This method allows now the existence of 2×M×N parameters which we can modify in order to improve the convergence speed and the stability of the solution. Some tests have been carried out to prove the validity of the theory and the method works fine for Z_{0mn} defined as in (11). We obtain exactly the same results as before.

Edge effect

We must find the right strategy to define the spatial mode impedance Z_{0mn} . Figure 2 show the existence of some instability that we believe to be connected to the spatial distribution of the electromagnetic fields, especially in the vicinity of the metal - dielectric transition (Wane et al. 2005).

It is probably necessary to explain the above statement. Let us look to the field distributions found by the "classic" WCIP method. The structure is the same microstrip line used before, placed in the middle of the box, along the x axis. The frequency is set to 5GHz. The line being only 2 pixels wide we expect only longitudinal current to exist on the line. Even incomplete as stated before and with errors, WCIP offers still the "good" shape of the fields (Edwards 1992; Gupta et al. 1996). As in figure 8 only E_y and J_x have considerable values, while E_x and J_y are small and "noisy", and appear as an influence of the source (which creates x direction fields) and mainly due to method errors (the lack of the convergence).

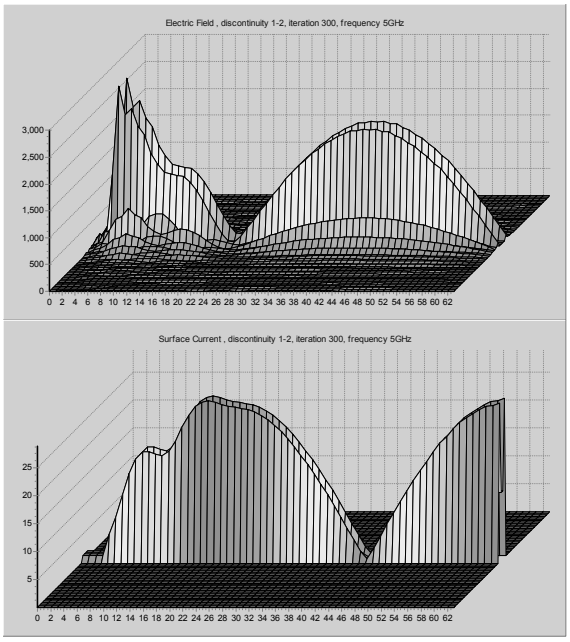

Figure 8: Transversal Field (E_y) and Longitudinal Surface Current (J_x)

Figure 8 shows two interesting facts. First, the E_y and J_x fields seem connected and in antiphase. We will investigate this connection later. Second and more important, both E_y and J_x , and consequently the waves A_x, A_y, B_x, B_y (as E_x and J_y can be neglected) have some major step discontinuities when going through a dielectric-metal discontinuity. These step discontinuities will not be accurately modeled by complex exponentials (as in the Fourier transform or even in the general TE/TM modes theory). It is our belief that this fact generates the instability of the WCIP method.

Let us consider a dielectric-metal interface along the x-axis as in figure 9. We consider a metallic sheet, occupying the x>0 semi plane in the xOy plane. The sheet height will be considered to be 0 (dz→0) for the case of the ideal planar circuit, and the width of the sheet analyzed will be decreased (dy→0) for the investigation of the edge effect (distribution of the fields around the Ox axis).

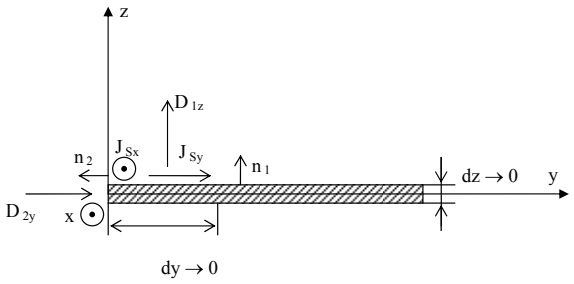

Figure 9: Edge Effect on an X Axis Discontinuity

On the metal-dielectric interface, the fields are described by:

$$\vec{n}\cdot\vec{D}=\rho_S\,;\ \vec{n}\cdot\vec{B}=0\,;\ \vec{n}\times\vec{E}=0\,;\ \vec{n}\times\vec{H}=\vec{J}_S \quad (21)$$

We apply (21) on two dielectric-metal interfaces, denoted by the normal vectors n_1 and n_2.

$$D_{1z}=\rho_{S1}\,;H_{1z}=0\,;E_{1x}=E_{1y}=0\,;$$
$$H_{1y}=-J_{S1x}\,;H_{1x}=J_{S1y} \quad (22)$$

If we consider the edge effect, we apply (22) in the proximity of the interface ($dy\to 0$) so the normal surface current (J_{Sy}) becomes 0, the surface current distribution changes to a linear distribution and, correspondingly, the surface charge density transforms into a linear charge density, along the edge: ρ_x.

Therefore, for $x \cong 0$; $x > 0$, the following apply:

$$\begin{aligned}&E_{1x}=E_{1y}=H_{1z}=H_{1x}=0\\&D_{1z}=\rho_x\cdot\delta(y);H_{1y}=-J_{S1x}\end{aligned} \quad (23)$$

For the second interface, we find in the same way for $x \cong 0$; $x < 0$:

$$\begin{aligned}&E_{2x}=E_{2z}=H_{2z}=H_{2y}=0\\&D_{2y}=-\rho_x\cdot\delta(z);H_{2z}=-J_{S2x}\end{aligned} \quad (24)$$

We must find the connection between the linear current density J_{Lx} and the linear charge density ρ_x. To achieve this we will consider an elementary volume on the interface between the metal and the dielectric like in figure 10.

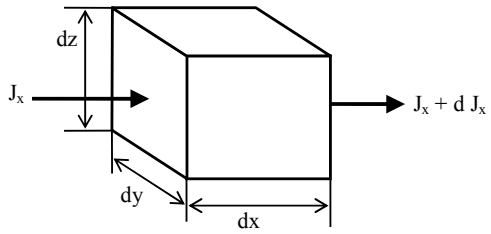

Figure 10: Charge Conservation in an Elementary Volume.

The calculus of the charge conservation in the elementary volume and equations (23) and (24) offer the connection between the fields existing in each side of the x-axis metal-dielectric interface:

$$\frac{\partial J_x}{\partial x}=-j\omega\varepsilon\cdot E_y \quad (25)$$

Correspondingly, for the dielectric-metal interface along the y-axis we obtain:

$$\frac{\partial J_y}{\partial y}=-j\omega\varepsilon\cdot E_x \quad (26)$$

Redefinition of the waves

From (25) and (26) we can see that there is a definition of the wave functions that will allow a smooth transition over the metal-dielectric interfaces. In the space domain this definition will be:

$$\vec{A}=\vec{E}-\frac{1}{j\omega\varepsilon}\cdot[R]\cdot\nabla\vec{J} \quad (27)$$

$$\vec{B}=\vec{E}+\frac{1}{j\omega\varepsilon}\cdot[R]\cdot\nabla\vec{J} \quad (28)$$

where [R] is a rotation operator that interchanges the x and y components of a vector (29).

$$[R]=\begin{bmatrix}0 & 1\\ 1 & 0\end{bmatrix} \quad (29)$$

Definitions (27) and (28) allow the extraction of the electric field, but the surface current can be obtained only by integration of the divergence operator. Like in section 2 we will try to define the waves in the modal domain. Some problems arise and must be solved.

First, the x and y components of a vector have different basis functions. In all the methods described above, x and y where independent directions and where treated separately the only connection between the two directions was made through a separation transform $\tilde{K}$ but after the modal decomposition. Definitions (27) and (28) rely upon a mixture between x and y components and we must find a way to do this before the modal decomposition.

Both x and y components of $\nabla\vec{J}$ have a harmonic surface decomposition after the basis functions $h_{mn}=\sin\frac{m\pi x}{a}\cdot\sin\frac{n\pi y}{b}$ and cannot be added with E_x and E_y maintaining the possibility of the modal decomposition after the basis functions (30). In order to preserve the classic definition of the TE/TM modal decomposition we define the waves in the modal domain as in (31).

$$\begin{cases}f_{mn}=\cos\frac{m\pi x}{a}\cdot\sin\frac{n\pi y}{b};(x\ direction)\\ g_{mn}=\sin\frac{m\pi x}{a}\cdot\cos\frac{n\pi y}{b};(y\ direction)\end{cases} \quad (30)$$

$$\begin{cases}A_x=E_x+\hat{Z}_0^x\cdot\sum_{mn}\langle J_y,g_{mn}\rangle\cdot\langle f_{mn}|\\ A_y=E_y+\hat{Z}_0^y\cdot\sum_{mn}\langle J_x,f_{mn}\rangle\cdot\langle g_{mn}|\end{cases} \quad (31)$$

In fact, in (31) an intermediary function with no physical correspondent is defined and the surface current is replaced by a composition of the modal amplitudes by a rotated modal basis. Equations (31) do not accurately apply (25) and (26) but with the appropriate choice of the impedance coefficients, we

can make the transition over different materials as smooth as possible.

We apply (31) with the following impedance coefficients:

$$Z_{mn}^{x} = -\frac{n\pi}{j\omega\varepsilon \cdot b}, \quad Z_{mn}^{y} = -\frac{m\pi}{j\omega\varepsilon \cdot a} \qquad (32)$$

The convergence plot for the same structure as in section 1 is in figure 11. This time the input impedance computed from the redefined waves (31) loses its physical sense as we perform the inversion of these definitions only at the end of the iterative procedure, but it is an accurate description of the convergence towards the solution.

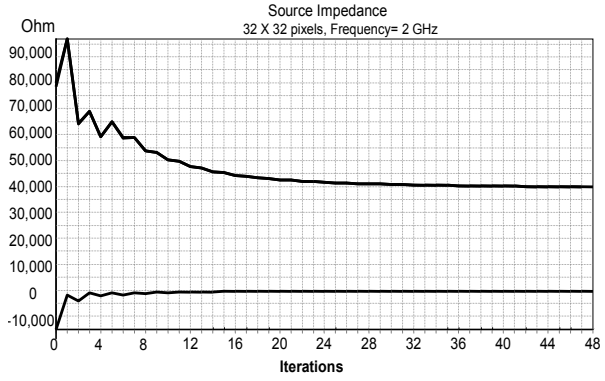

Figure 11: Convergence Analysis - New Definition

IV. CONCLUSIONS

We present in this work three methods used to improve the convergence efficiency in WCIP. All computations were performed using custom software developped in our laboratory in C++ and visual Windows technology.

Section II introduces two generally available methods, appropriate for almost any iterative methods. Analogy with a discrete in time feedback system allows altering temporarily the energy source and/or the structure itself in order to achieve better convergence. We obtain more accurate and faster results in term of field distributions. Relative improvement in speed is between 2 and 3 depending on the parameters of the alteration, with the added benefit of the improved solution.

Section III offers a particular method in the case of the WCIP. We obtain a very good behavior of the iterative procedure. The new definition of the waves reaches a stable solution in around 30 iterations as opposed to 150 iterations in figure 2 and without the oscillations showing the lack of convergence of the classic method.

This work is still in progress. Alternate definitions of the impedance matrices in (31) are investigated, in order to provide a smooth transition of the waves over the metal/dielectric edge.

REFERENCES

Akatimagool, S.; Bajon, D.; Baudrand, H. 2001. “Analysis of multi-layer integrated inductors with wave concept iterative procedure (WCIP)”, IEEE MTT-S International Microwave Symposium Digest, 2001, Volume 3, 1941 - 1944

Azizi M.; Boussouis M.; Aubert H. and Baudrand H. 1996. “A three dimensional analysis of planar discontinuities by an iterative method”, Microwave and Optical Technology Letters, Vol. 13, No. 6, 1996, 372-376.

Azizi, M.; Sboui, N.; Choubani, F.; Gharsallah, A. 2008. “A novel design of photonic band gap by F.W.C.I.P method”, 2nd International Conference on Signals, Circuits and Systems, SCS 2008 Tunis 7-9 Nov. 2008

Azizi. M., Aubert H. and Baudrand H. 1995. “A new iterative method for scattering problems”, 1995 European Microwave Conference Proceedings, Vol.1, pp. 255-258.

Baudrand, H.; Raveu, N.; Sboui, N.; Fontgalland, G. 2007. “Applications of multiscale waves concept iterative procedure”, IEEE MTT-S International Microwave and Optoelectronics Conference, IMOC 2007, 748 - 752

Edwards T.C. 1992. “Foundations for Microstrip Circuit Design”, John Wiley & Sons Inc., 1992, ISBN 0-471-93062-8.

Gupta K.C.; Bahl I.; Bhartia P; Garg R. 1996. “Microstrip Lines and Slotlines” 2nd ed., Artech House, 1996, ISBN 0-89006-766-X.

Lyons R. 1998. “Windowing Functions Improve FFT Results, Part I”, Test & Measurement World, June 1998, 37-44

N'gongo, R.S.; Baudrand, H. 1999. “A new approach for microstrip active antennas using modal F.F.T-algorithm”, Antennas and Propagation Society International Symposium, 1999. IEEE, Volume 3, 11-16 July 1999, 1700 - 1703

Nuttall A. 1981. “Some Windows with Very Good Sidelobe Behavior” IEEE Transactions on Acoustics, Speech, and Signal Processing, Vol. ASSP-29, No. 1, February 1981.

Raveu, N.; Pigaglio, O.; Prigent, G.; Baudrand, H. 2007. “Improvement in the wave concept iterative procedure through spectral connection”, 2007. European Microwave Conference, 28 - 31

Raveu, N.; Vuong, T.P.; Terrasse, I.; Piau, G.-P.; Fontgalland, G.; Baudrand, H. 2004. “Wave concept iterative procedure applied to cylinders”, IEE Proceedings on Microwaves, Antennas and Propagation Volume 151, Issue 5, 409 - 416

Smith S.W. 1999. “The Scientist and Engineer's Guide to Digital Signal Processing”, 2nd ed., California Technical Publishing, 1999.

Wane, S.; Bajon, D. 2006. “Full-Wave Analysis of Inhomogeneous Deep-Trench Isolation Patterning for Substrate Coupling Reduction and Q-Factor Improvement”, IEEE Transactions on Microwave Theory and Techniques, Volume 54, Issue 12, Part 2, 4397 - 4411

Wane, S.; Bajon, D.; Baudrand, H.; Gamand, P. 2005. “A new full-wave hybrid differential-integral approach for the investigation of multilayer structures including nonuniformly doped diffusions”, IEEE Transactions on Microwave Theory and Techniques, Volume 53, Issue 1, 200 - 214

INVESTIGATION OF THE HEXACHIRAL HONEYCOMB EMC PROPERTIES BY FULL WAVE ELECTROMAGNETIC SIMULATION

Romeo-Cristian Ciobanu
Cristina Schreiner
Dept. of Electrical Measurements and Materials
Technical University Iasi, Romania
Iasi, 700050, Romania
E-mail: rciobanu@ee.tuiasi.ro

Radu-Florin Damian
Dept. of Telecommunications
Technical University Iasi, Romania
Iasi, 700506, Romania
E-mail: rdamian@etc.tuiasi.ro

KEYWORDS

Hexachiral honeycomb, Full wave electromagnetic, CST Microwave Studio

ABSTRACT

A hexachiral honeycomb structure with good mechanical properties, is investigated through full wave electromagnetic simulation. This new material shows some interesting EMC properties and promises better performance using different insertion techniques. The effect of the electromagnetic chirality is investigated. Design maps and thermal computations are derived.

I. INTRODUCTION

In the past years, an increasing amount of effort has been invested in the development of new materials, with good mechanical properties, low weight and low cost. In particular auxetic materials benefit from their negative Poisson's ratio (Grima 2007) and are investigated closely in the last decade (Li et al. 2000, Ammari et al. 1998, Oussaid R. and Haraoubia B. 2004). In the same time, we witness an increased utilization of the RF spectrum, especially in the free bands (2.4GHz). Coding techniques have been developed to ensure the "peaceful" coexistence of multiple emitter/receiver pairs in the same frequency band. In some cases, these techniques are not sufficient, especially when good shielding for an enclosure is imperative (aeronautics - Bornengo D. et al. 2005, medicine etc.). A natural step forward is to investigate the electromagnetic properties of these materials, in order to provide good electromagnetic shielding.

Electromagnetic metamaterials are defined as artificial effectively homogeneous electromagnetic structures with unusual properties not readily available in nature. An effectively homogeneous structure is a structure whose structural average cell size L is much smaller than the guided wavelength λ_g. i.e. the average cell size should be at least smaller than a quarter of wavelength (Caloz and Itoh 2006),

$$L < \frac{\lambda_g}{4} \tag{1}$$

The condition (1) is known as the effective-homogeneity limit or effective-homogeneity condition, and ensures that refractive phenomena will dominate over scattering/diffraction phenomena when a wave propagates inside the medium. In the present application, the frequency range of interest (1 to 15GHz) implies a guided waveguide between 10 mm and 150 mm, and we expect the chirality defined by geometry to play an electromagnetic role, depending on the cell size, especially at higher frequencies (7 to 15 GHz).

Depending on the method used for defining the magnetoelectric dyadics, there are multiple constitutive relations in extensive use for chiral mediums: Drude-Born-Fedorov (Athanasiadis and Costakis 2000, Oksanen et al. 1992) Post (Jaggard et al. 1988), Tellegen (Qiu et al. 2007). Equivalence between these relations can be obtained (Liu and Li 1999) by substitution in Maxwell's equations.

Widely used are Post constitutive relations in the frequency domain, valid for time harmonic electromagnetic fields: Eqs. (2), (3).

$$\mathbf{D} = \varepsilon_c \mathbf{E} + j\xi_c \mathbf{B} \tag{2}$$

$$\mathbf{H} = j\xi_c \mathbf{E} + \mathbf{B}/\mu_c \tag{3}$$

where ε_c and μ_c represent an equivalent of the permittivity and permeability, ξ_c the chirality admittance, which is a measure of the handedness of the medium and j is the imaginary unit.

II. SIMULATION SETUP

The structure used in tests was a fiber reinforced polymer prototype, developed in the framework of the CHISMACOMB (CHIral SMArt honeyCOMB) FP6-EU-013641 project (Chismacomb 2008), by Italcompany (figure 1). The structure is a hexachiral honeycomb, each of the equally spaced cylinders being connected to his 6 neighbors by ligaments and is based on the idea found in (Prall and Lakes 1997) which is a simplification of a two-dimensional molecular model studied earlier (Wojciechowski 1989).

Proceedings 23rd European Conference on Modelling and Simulation ©ECMS Javier Otamendi, Andrzej Bargiela, José Luis Montes, Luis Miguel Doncel Pedrera (Editors)
ISBN: 978-0-9553018-8-9 / ISBN: 978-0-9553018-9-6 (CD)

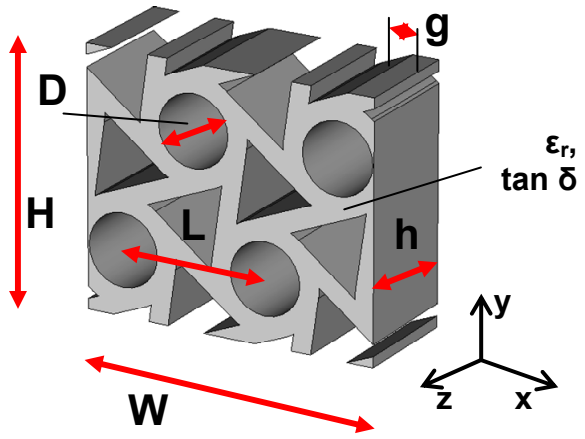

Figure 1: Rectangular Unit Cell.

The interaction between a plane wave and an infinitely large sheet of auxetic material at normal incidence was investigated. The boundary conditions were set to electric wall (both walls on x directions) and magnetic wall (y direction walls). An input wave port was placed at a distance equal to the minimum between the 8th part of the wavelength and 5 mesh lines from the structure, the second (exit) wave port is added only when losses inside the structure were taken into account.

In order to limit the model's dimensions, the periodicity of the structure was investigated. While the intrinsic unit cell for this structure will contain only one cylinder and half of every surrounding ligament, numerical electromagnetic computation demands a rectangular unit cell which can be placed on a regular (not staggered) rectangular grid in order to preserve electromagnetic fields symmetries. The rectangular unit cell is showed in figure 2, the length and width being equal to $W = 2 \cdot L$ (x direction) and $H = L \cdot \sqrt{3}$ (y direction) respectively (where L is the cylinder separation). Table 1 shows the typical dimensions used in tests when we parameterize the others.

Table 1: Typical Dimensions.

Parameter	Description	Value
D	Internal cylinder diameter	18.58 mm
L	Cylinder separation	24.72 mm
h	Height of the panel	19.75 mm
g	Ligament width	3.3 mm
ε_r	Electrical permittivity	2.5 (4)
tan δ	Loss angle tangent	0 (0.1-0.5)

The results of the simulations show the S parameters for the structure. The typical shielding parameters reflectance, transmittance and absorption are related to the S parameters by the following equations (Hong et al. 2003), as long as the surrounding medium is lossless:

$$R = |S_{11}|^2 \quad (4)$$

$$T = |S_{21}|^2 \quad (5)$$

$$A = 1 - R - T = 1 - |S_{11}|^2 - |S_{21}|^2 \quad (6)$$

III. ACCURACY OF THE RESULTS

The CST Microwave Studio frequency domain solver solves the problem for a single frequency at a time, and for a number of adaptively chosen frequency samples in the course of a frequency sweep. For each frequency sample, the linear equation system will be solved by an iterative (e.g. conjugate gradient) or sparse direct solver.

The CST Microwave Studio time domain solver calculates the development of fields through time at discrete locations and at discrete time samples. It calculates the transmission of energy between various ports and/or open space of the investigated structure.

For the hexachiral structure under test, the auxetic layer is illuminated with a plane wave, coming from the z direction, with normal incidence to the material. The polarization of the plane wave in the material is imposed by the electric/magnetic wall boundary conditions, and for correct calculations we expect the electromagnetic fields inside the structure to follow the characteristics of the incident wave. As in figure 2, we find that inside the hexachiral honeycomb, the electric field will have only E_x component, whereas the magnetic field shows only H_y component.

The final test was the comparison between the FDTD and FDFD analysis results for the same structure. The two computation methods are not related, even the mesh is different in this case (hexahedral with Perfect Boundary Approximation® - PBA for FDTD and tetrahedral for the frequency domain solver). The results are found to be essentially the same (see figure 3).

The difference between the two curves is maximum ±1dB in the 1÷10GHz range, except the frequencies around the reflection annulment, where a slight variation of the zero's frequency is detected (0.1GHz, meaning a 1.8% difference between the two minima) around 5.8GHz. The two solvers are independent even if they belong to the same software suite, so we can estimate a ±2dB general error coupled with a ±2% peak detection error for the rest of the simulations.

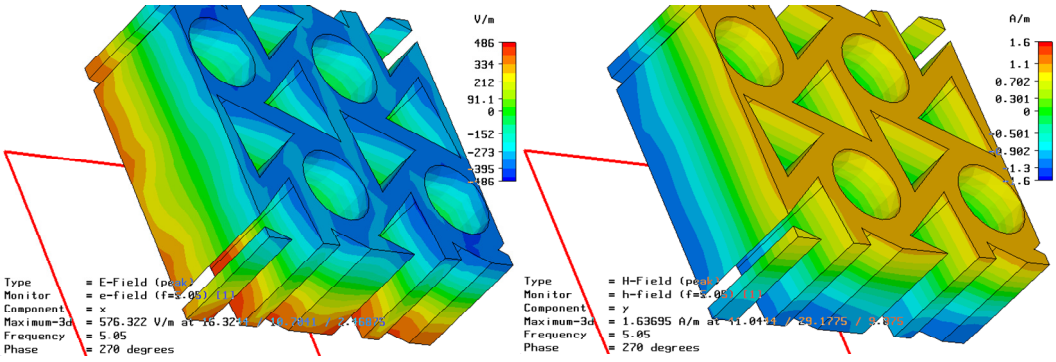

Figure 2: E_x (left) and H_y (right) Inside the Structure

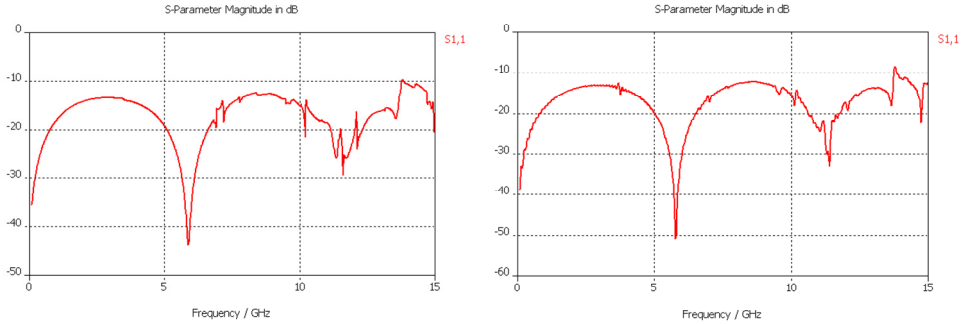

Figure 3: S_{11} for the Loseless Structure by FDFD (left) and FDTD (right) Computation

IV. RESULTS AND INFLUENCE OF CHIRALITY

Parametric studies investigated the effect of the dimensions (L, D, h, g) and material properties (ε, σ, tan δ). Figure 4 shows the influence of L, h (in this order) for the lossless dielectric over the reflection coefficient (S_{11}), and figure 5 shows the influence of ε and tan δ over reflection coefficient (S_{11}) or over the transmission coefficient (S_{21}) when losses are taken into account

Analysis shows that the chiral structure has almost identical properties (figures 4, 5) with an equivalent homogenous dielectric layer, so the mechanical and thermal advantages provided by the structure do not affect the electromagnetic properties in the bandwidth considered (0.1-10 GHz).

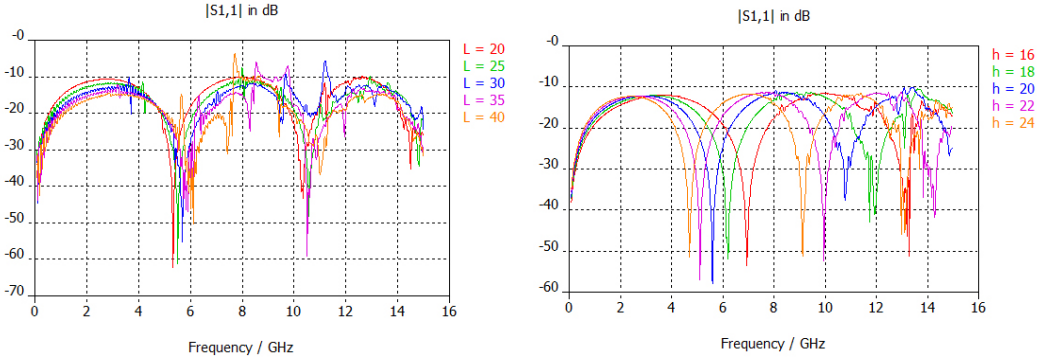

Figure 4: Cylinder Separation (L - left) and Layers' Height (h - right) Influence over S_{11}

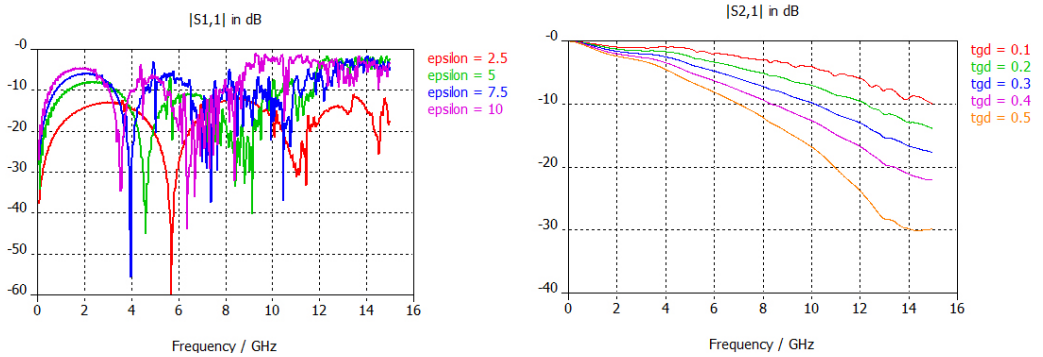

Figure 5: Electrical permittivity (ε - left) and Loss tangent (tan δ - right) influence over S_{11}/S_{22}

Figures 4-5 show that for the lossless chiral layer we have a typical half-wave reflectionless slab (Orfanidis 2008). We obtain zeroes for the reflection coefficient at the frequencies that verify the condition:

$$h = k \cdot \frac{\lambda_g}{2} = \frac{k}{2} \cdot \frac{c}{f\sqrt{\varepsilon_{eff}}} \tag{7}$$

where k must be an integer and λ_g is the guided wavelength, inside the equivalent homogenous dielectric slab. This behavior offers interesting electromagnetic applications, as radar invisibility or building wall transparency.

Equation (7) offers the possibility to use the results in figure 4 to investigate the variation of the effective electrical permittivity on the frequency. Every value for layer's height (h) generate at least two minima of the reflectivity in the bandwidth considered, corresponding to k=1, k=2 in equation (7). We can compute the effective electrical permittivity with equation (8).

$$\varepsilon_{eff}\left(f_{\min,k}\right) = \left(\frac{k \cdot c}{2 f_{\min,k} \cdot h}\right)^2 \tag{8}$$

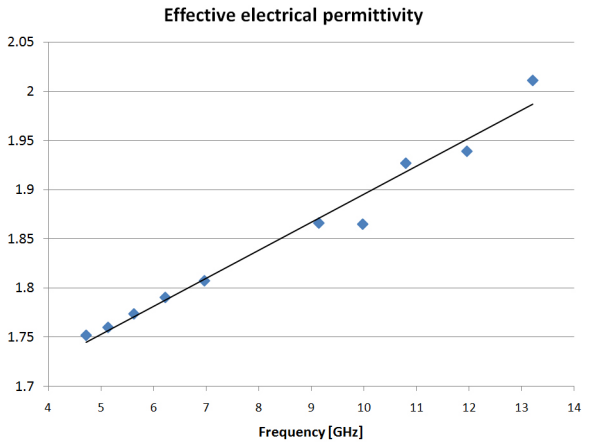

Figure 6. Effective electrical permittivity

The effective electrical permittivity increases linearly with the frequency, as the electromagnetic field is confined inside the dielectric at higher frequency. The results in figure 4 on which figure 6 is based are obtained for ε = 2.5 for the base material. In this case, we find the effective permittivity ranging from 1.61 to 2.1, depending on the frequency. In addition, as the frequency increases we notice slight variations from the predicted linear increase, as the chirality of the structure becomes more and more evident.

The effects of the chirality appear as we increase the frequency, the electrical permittivity and the cylinder separation. In the typical situation (table 1), equation (1) gives a frequency limit of about 2.37 GHz. Close inspection of the results (figure 4) shows that obvious effects of the microscopic chiral structure are visible at 8 GHz.

Condition (1) can be expressed in terms of visible influence as:

$$L \cdot f \cdot \sqrt{\varepsilon_{eff}} \approx \frac{3c}{4} \tag{9}$$

The other results verify this relationship. Increase of ε from 2.5 to 10 (figure 5) lower the frequency of appearance of chiral effects from 8GHz to 4 GHz (the square root of the permittivity factor of 4). Increase of L to 40 mm (figure 4) show the same effect starting from 5GHz.

We can conclude that regarding the hexachiral honeycomb, chirality influence becomes obvious when relation (9) applies, but while visible, this influence does not affect the macroscopic behavior of the panel under test. The hexachiral panel behaves as a homogenous dielectric, with a different effective electrical permittivity (figure 6).

V. PARAMETRIC ANALYSIS AND DESIGN MAPS

The results in figures 4, 5 offer important information regarding the behavior of the intrinsic chiral panel but are less suggestive from a macroscopic or "application" point of view. The macroscopic values of interest for a microwave shield designer are generally related to transmittance (figure 5b) at some critical frequencies (typically 0.9÷1GHz - the GSM band, 2.4 GHz - free use frequency bandwidth, and 5.8 GHz – a second free bandwidth) or reflectivity parameters (figures. 4-5a) as the frequency of the first minimum, the out of band maximum reflectivity (first and second maximum), depending on the application.

The question a designer is asked is rather an "inverse" of the answer from figures 4, 5. Usually the designer is not interested by the performance of "that" material, but instead the question is: "what material must I choose to obtain a certain transmittance or a certain reflectivity".
In the next set of analyses, the aim is to investigate the influence of the material properties (tan δ and ε) over the transmission and reflectivity properties.

Table 2: Geometric Parameters Sweep.

Parameter	Range	Step
D	20÷50 mm	5 mm
H	20÷50 mm	5 mm
L/D	1.5÷3	0.25
D/g	5÷20	2.5

In the first set of computations we maintain the same geometrical properties (D, L, h, g - Table 1) but we insert variations in material properties: tan δ = [0 , 0.5] and ε = [1.5 , 10]. S_{11} and S_{21} are computed. The parametric curves are plotted in figure 7 in order to facilitate shielding design with the hexachiral honeycomb. We represent the transmittance at the three

selected frequencies and the minima/maxima of the reflectance.

For the second set of computations we choose L/D and D/g ratios as important for the aspect ratio of the panel and with fixed dielectric parameters ($\varepsilon = 4$ and $\tan\delta = 0.01$) we make the transmission and reflection computation for geometric parameters as in Table 2. The results are plotted in figure 8.

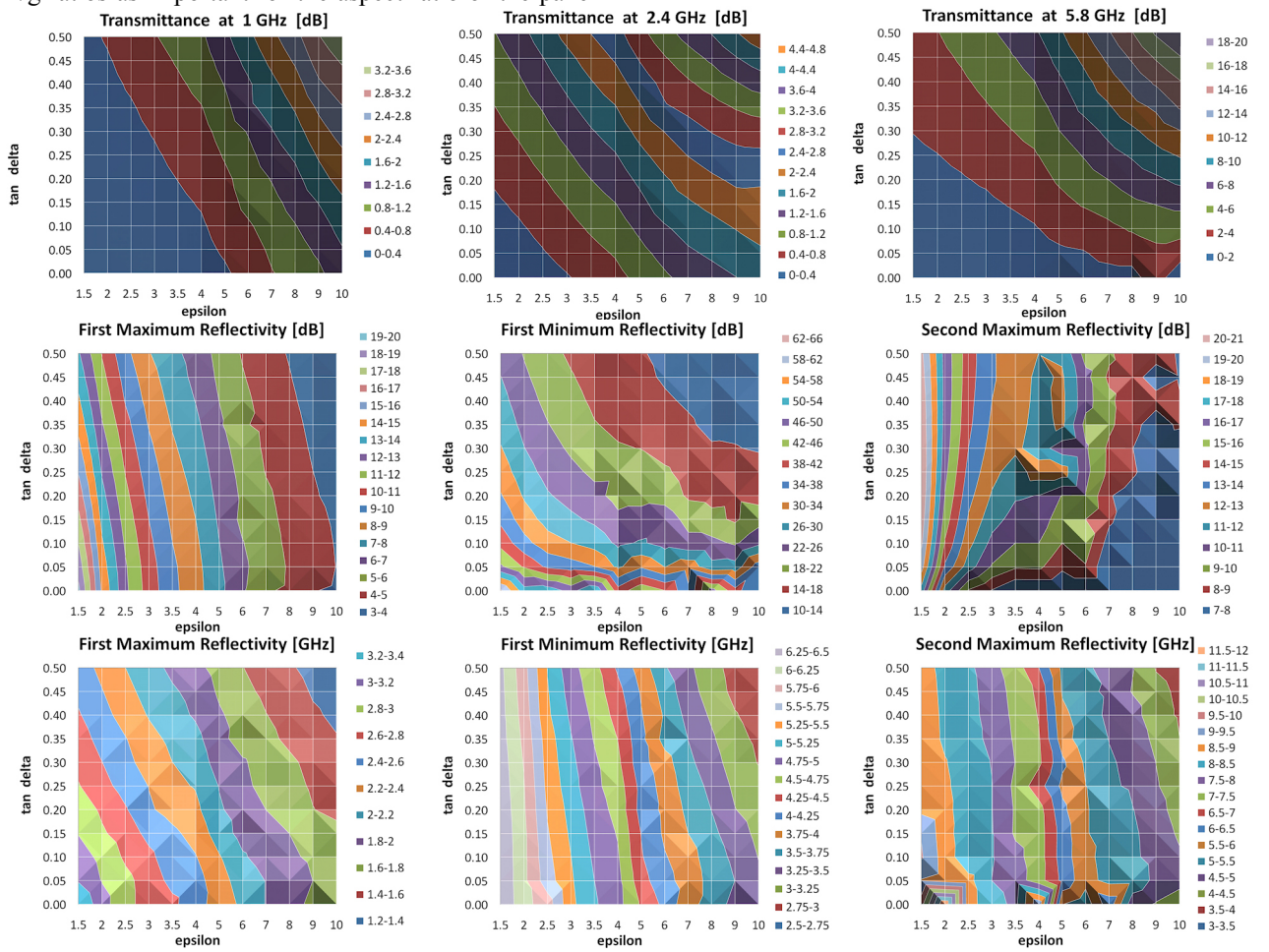

Figure 7 Dielectric Properties Design Maps.

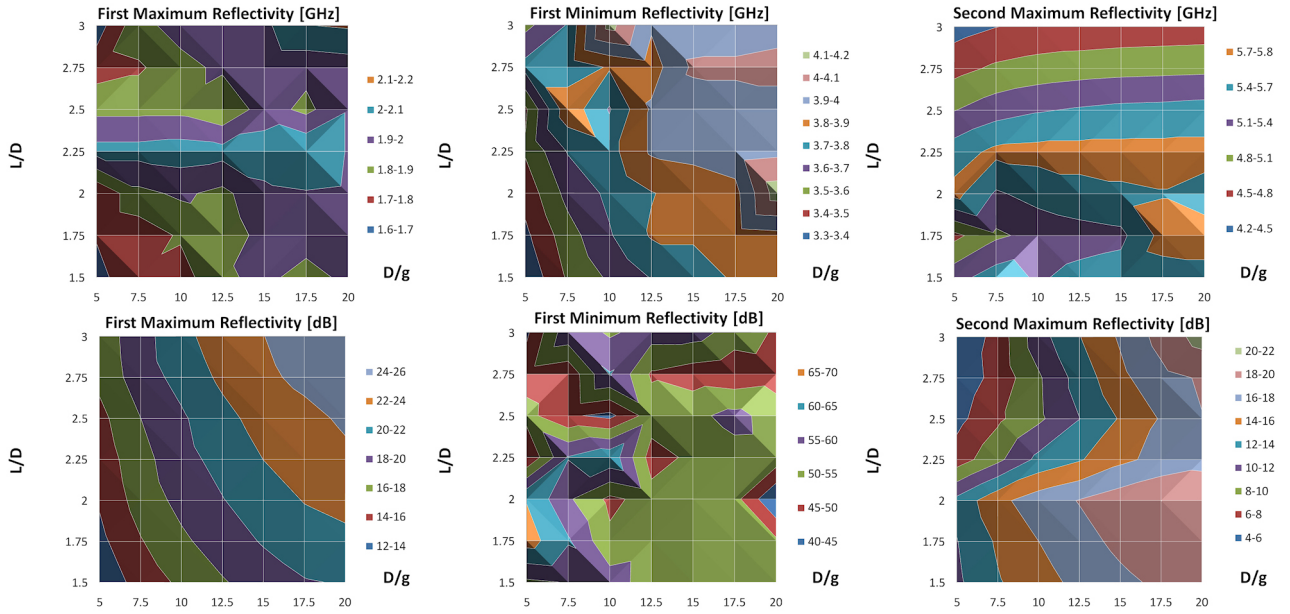

Figure 8 Geometric Properties Design Maps.

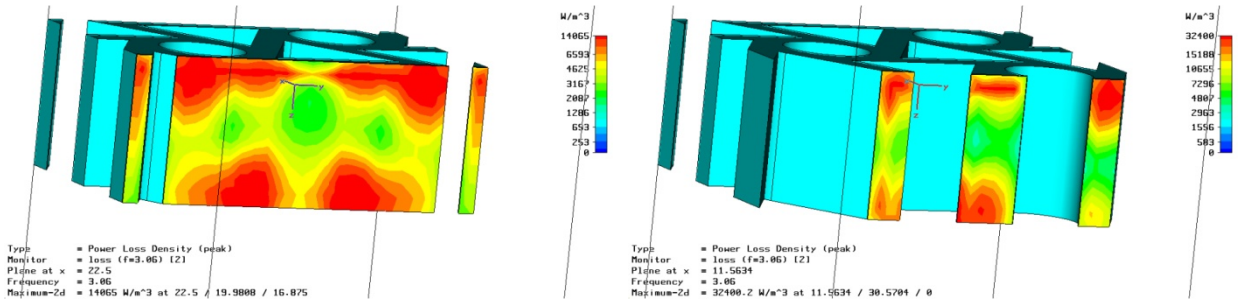

Figure 9: Power Loss Density at 3.06GHz

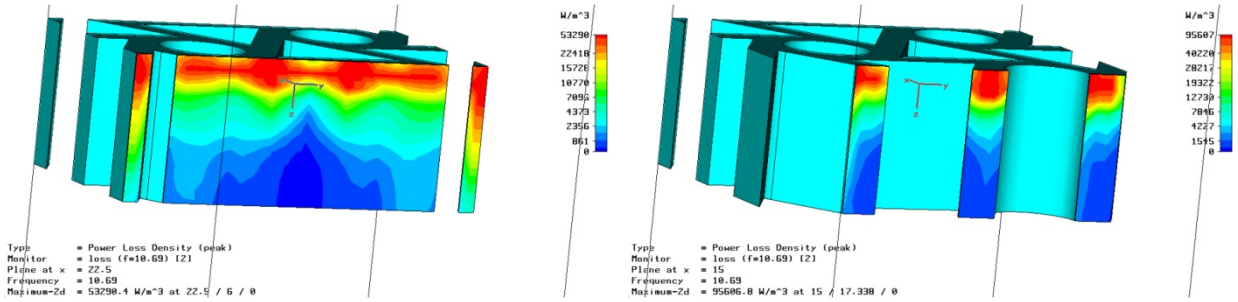

Figure 10: Power Loss Density at 10.69GHz

VI. THERMAL DISTRIBUTION

Simulations have been performed in order to identify the energy absorption characteristics inside the material. The first results emphasize an energy concentration depending solely on the hexachiral geometry. The power loss density inside the ligaments of the hexachiral honeycomb is an indication of energy dissipation inside the structure. The two frequencies chosen, 3.06GHz and 10.69GHz are those corresponding to a minimum of the reflectance (figure 9) and transmittance (figure 10) respectively, as the frequencies at which maximum thermal effect is expected.

A concentration of the energy dissipation will generate a temperature increase in certain points. However, this energy is not accumulated, the most significant heat transfer mechanism being thermal conduction (eq. 7). The speed of the heat transfer through a portion of material of transversal area A and length x depends on the steady state temperature difference.

Heat is generated differently in two points according to the electromagnetic energy concentration pattern (eq. 5). We can estimate the steady state for the thermal phenomenon when the difference between the generated heat in every point equals the heat transferred by conduction between the same points (eqs. 10-11).

$$\Delta\left(\frac{dQ}{dt}\right) = \left.\frac{dQ}{dt}\right|_1 - \left.\frac{dQ}{dt}\right|_2 = \Delta P_V \cdot dV \qquad (10)$$

$$\left.\frac{dQ}{dt}\right|_{1-2} = k \cdot A \cdot \frac{\Delta T}{x} \qquad (11)$$

We used the same software suite (CST Microwave Studio) described in section IV, with the difference that in single frequency analysis the FDFD (Finite Differences in Frequency Domain) solver was used to compute the fields inside the structure. The computation is full 3D, figures 9-10 show the power loss density in different longitudinal sections through the panel.

The power loss distribution is mainly longitudinal (in the direction of the incident wave). The incident illumination is 320W/m^2 (normalization: 1W over the surface of the input port), a rather high value if we consider that the safety limit for RF workers is 50W/m^2. While such a situation is not usually encountered, we can use eqs. (10), (11) to estimate the temperature gradient which will appear inside the hexachiral structure. At 3.06 GHz (figure 9), we have maximum $\Delta P_V \approx$ 12,000 W/m^3 and $\Delta P_V \approx$ 30,000 W/m^3 inside the cylinder and inside the ligaments respectively. The maximum temperature variation is $\Delta T \approx 4$ K and $\Delta T \approx$ 10 K respectively. As the power losses are related to transmission behavior, we expect greater effect when the transmittance reaches a minimum. At 10.69 GHz (figure 10), we have maximum $\Delta P_V \approx$ 53,000 W/m^3 and $\Delta P_V \approx$ 95,000 W/m^3 inside the cylinder and inside the ligaments respectively, the corresponding temperature variation being $\Delta T \approx 18$ K and $\Delta T \approx 33$ K respectively.

In typical applications (10 to 50 W/m^2 - safety limits) the effect is less important (up to 5K temperature differences) but the differences in temperature can reach 100K at 1kW/m^2 illumination. Wireless Power Transmission can use up to 30 ÷ 90 kW/m^2 at the space reflectors.

The simple hexachiral panel, subject to localized electromagnetic power dissipation develops thermal gradients which affect the mechanical performance thus thermal analysis in high power applications must rely on temperature gradient instead of uniformity.

CONCLUSIONS

In this paper a complete investigation of the hexachiral honeycomb by full wave electromagnetic simulation is performed. The software suite CST Microwave Studio is used, with the added benefit of the presence of multiple solvers. This allowed us to perform accuracy estimation (secton III) and extended the range of simulations we were able to perform.

The time domain solver (FDTD) was used in those situations where multiple simulations were needed and speed was an important issue (more than 10,000 different individual simulations were performed). Multiple parametric simulations were made, which allowed the investigation of the chirality in section IV and the derivation of the design maps in section V.

The frequency domain solver (FDFD) which is slower but more accurate in small bandwidths was used in order to verify the boundary conditions used (section II) and in order to investigate the microwave power distribution inside the material, which allowed the thermal analysis in section VI.

REFERENCES

Ammari H.; Laouadi M.; Nedelec J.-C.; 1998, "Low frequency behavior of solutions to electromagnetic scattering problems in chiral media", SIAM Journal. of Applied. Math, Society for Industrial and Applied Mathematics, Vol. 58, No. 3, 1022-1042, 1998

Athanasiadis C., Costakis G. 2000. "Electromagnetic scattering by a homogenous chiral obstacle in a chiral environement", IMA Journal of Applied Mathematics, Vol. 64 (2000), 245 - 258

Bornengo D.; Scarpa F.; Remillat C. 2005. "Evaluation of hexagonal chiral structure for morphing airfoil concept", Proceedings. IMechE Vol. 219 Part G: J. Aerospace Engineering, 185-192, 2005

Caloz C.; Itoh T.. 2006 "Electromagnetic metamaterials : transmission line theory and microwave applications: the engineering approach", John Wiley & Sons, Inc., Hoboken, New Jersey, 2006

Chismacomb 2008. "CHISMACOMB", FP6 Specific Target Research Project, FP6-EU-013641, http://www.chismacomb.eu/

Grima, J. 2007, "Negative, negative and more negative: systems exhibiting negative Poisson's ratio, negative thermal expansion and/or negative compressibility", 4th International Workshop on Auxetics and Related Systems, Malta, 2007, 8

Hong Y.K.; Lee C.Y.; Jeong C.K.; Lee D.E.; Kim K., Joo J. 2003 "Method and apparatus to measure electromagnetic interference shielding efficiency and its shielding characteristics in broadband frequency ranges", Review of Scientific Instruments, Volume 74, Issue 2, February 2003, 1098-1102

Jaggard D.L.; Sun X.; Engheta N. 1988. "Canonical Sources and Duality in Chiral Media", IEEE Transactions On Antennas And Propagation, Vol. 36, No. 7, July 1988, 1007-1013

Li, L.W.; You D.; Leong M.S. and Yeo T.S. 2000, "Electromagnetic scattering by multilayered chiral-media structures: a scattering-to-radiation transform , Journal of Electromagnetic Waves and Applications", Vol. 14, 401-404, 2000

Liu S.; Li L.W. 1999. "Mook-Seng Leong,Tat-Soon Yeo; "On the constitutive relations of chiral media and green's dyadics for an unbounded chiral medium", Microwave And Optical Technology Letters , Vol. 23, No. 6, 1999, 357 - 361

Oksanen M.; Koivisto P.; Tretyakov S. 1992. Vector Circuit Method Applied for Chiral Slab Waveguides, Journal Of Lightwave Technology, Vol. 10, No. 2, February 1992, 150-155

Orfanidis S.J. 2008. "Electromagnetic Waves and Antennas", Rutgers University online book, ch 5, 160-166, http://www.ece.rutgers.edu/~orfanidi/ewa/

Oussaid R.; Haraoubia B. 2004, "Behavior of a chiral material in terms of a guided wave propagation", International Journal of Applied Electromagnetics and Mechanics, vol. 19 , 2004, 631-635

Prall D; Lakes RS. 1997. "Properties of a chiral honeycomb with a poisson's ratio of - 1", Int. J. Mech. Sci. Vol. 39, No. 3, 305-314, 1997

Qiu C.W.; Yao H.Y.; Burokur S.N.; Zouhdi S., Li L.W. 2007. ."Electromagnetic Scattering Properties in a Multilayered Metamaterial Cylinder", IEICE Trans. Commun., Vol.E90–B, No.9 September 2007, 2423-2429

Wojciechowski K.W. 1989, "Two-dimensional isotropic systems with a negative Poisson ratio", Physics Letters A137, 60-64 (1989)

Electromagnetic energy harvesting by field concentration in intelligent materials

Romeo Ciobanu[1], Radu Damian[1*] and Cristina Schreiner[1]
[1] Technical University Iasi, Romania
*E-mail: rdamian@etti.tuiasi.ro

Abstract— **Electromagnetic shields are used primarily for absorption of parasitic energy. Usually a shield will consume and concentrate the energy dissipation inside himself in order to achieve his protection function. Electromagnetic energy concentration can be sometimes controlled in a certain manner, and eventual detectors or "energy harvesters" can be placed in optimum locations, with higher energy levels.**

Keywords -- metamaterials, chiral, honeycomb, microwave absorption, energy concentration

I. INTRODUCTION

In the past years, an increasing amount of effort has been invested in the development of new materials, with good mechanical properties, low weight and low cost. In particular auxetic materials benefit from their negative Poisson's ratio [1] and are investigated closely in the last decade [2], [3], [4].

In the same time, we witness an increase in the electromagnetic pollution of the spectrum especially in the free ISM bands (e.g. 2.4GHz, 5.8GHz) or in the GSM bands (900MHz, 1800MHz). Electromagnetic shielding of the buildings arises as a useful, sometimes necessary application when the interior of the building must be protected from high exterior level of radiation, for the protection of the inhabitants or other sensitive electronic equipment. As possible examples some can cite situations where inhabited buildings are placed in the immediate vicinity of high power emitters (radar, GSM base stations). While the biological effect of the electromagnetic radiation is still under strong debate, the inevitable introduction of the technology in everyday life leads to the necessity of protecting the inhabitants from outside undesired influence.

The effect on the electronic equipment is known and not subject to the same debate. Outside emitters, at certain power levels, can indeed influence the functioning of the inside equipment. Coding techniques have been developed to ensure the "peaceful" coexistence of multiple emitter/receiver pairs in the same frequency band. The situation is especially critical where the same frequency band is used for multiple applications (for example the 2.4GHz band is used by wireless networking, Bluetooth, cordless telephones, video senders, microwave ovens etc.). In some cases, these techniques are not sufficient, especially when good shielding for an enclosure is imperative (aeronautics [5], medicine etc.).

Microwave shielding structures can be used in energy harvesting applications. Usually a shield will consume and concentrate the energy dissipation inside his structure. Energy distribution can be sometimes controlled in a certain manner, and eventual detectors or "energy harvesters" can be placed in optimum locations with higher energy concentration. Even in the absence of the shielding properties, certain structures can be used only to rise the energy level in some points, where is needed.

II. COMPUTER SIMULATIONS

A. Hexachiral honeycomb

The structure used in tests was a fiber reinforced polymer (as in [6]) prototype, developed in the framework of the CHISMACOMB FP6 EU project [7] by the Italcompany (Fig. 1). The structure is a hexachiral honeycomb, each of the equally spaced cylinders being connected with strings to 6 of his neighbors.

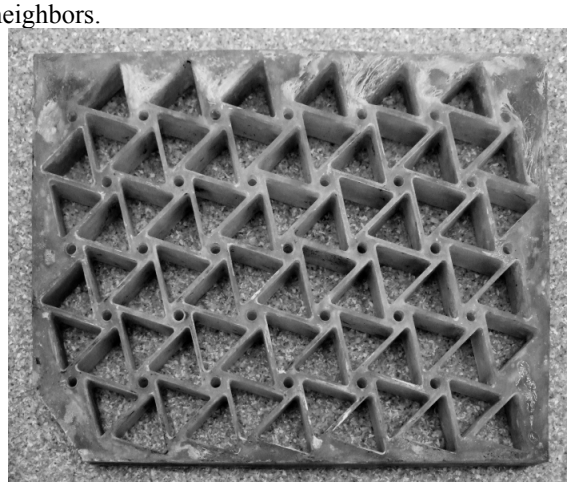

Figure 1. Hexachiral honeycomb

In order to limit the dimensions of the model, the periodicity of the structure has been investigated. While the intrinsic unit cell for this structure will contain only one cylinder and half of every surrounding ligament, numerical electromagnetic computation demands a rectangular unit cell. The rectangular unit cell is showed in Fig. 2, the length and width being equal to $2 \cdot L$ (x direction) and $L \cdot \sqrt{3}$ (y direction) respectively (where L is the cylinder separation). We investigate the interaction between a plane wave and an infinitely large sheet of auxetic material, at normal incidence. The boundary conditions are set to electric wall (both walls on x directions) and magnetic wall (y direction walls) [8]. An input wave port is placed at some space from the structure and the second

(exit) wave port is added because losses inside the structure are taken into account.

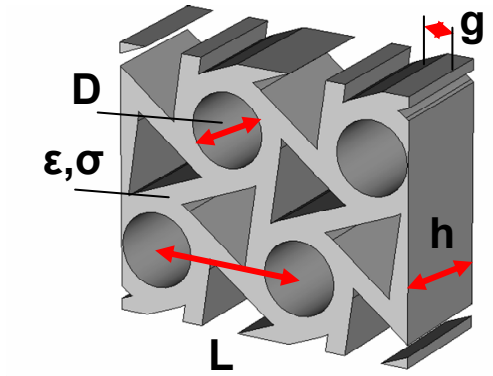

Figure 2. Rectangular unit cell

The software suite CST Microwave Studio was used for simulations. From the various solvers available, the time domain solver (FDTD) is particularly appropriate for EMC and microwave shielding problems. The CST proprietary technology Perfect Boundary Approximation® (PBA) [9] was used for structure's spatial discretization. The simulated structure and the electromagnetic fields are mapped to hexahedral mesh. PBA allows a very good approximation even of curved surfaces within the cubic mesh cells, and together with a convergence study [10] we reached the needed speed improvement - typically 5 minutes for FDTD versus over 2 days used by the frequency domain solver (FDFD) of the same software suite.

The results of the simulation show the S parameters for the structure. Reference [11] shows that the typical shielding parameters reflectance, transmittance and absorption are connected to the S parameters as in (1)-(3).

$$R = |S_{11}|^2 \quad (1)$$

$$T = |S_{21}|^2 \quad (2)$$

$$A = 1 - R - T = 1 - |S_{11}|^2 - |S_{21}|^2 \quad (3)$$

III. Power Loss Distribution Inside The Structure

Simulations have been performed in order to identify the energy absorption characteristics inside the material.

A. Dielectric Structure

The first results emphasize an energy concentration depending solely on the hexachiral geometry. The power loss density inside the ligaments of the hexachiral honeycomb is an indication of energy dissipation inside the structure. The base dielectric material used as the panel is characterized by $\varepsilon_r = 10$ and $\tan\delta = 0.1$.

The two frequencies chosen for the analysis, 3.06GHz and 10.69GHz, are those corresponding to a minimum of the reflectance and transmittance (Fig. 3) respectively, as the frequencies at which a maximum energy concentration is expected.

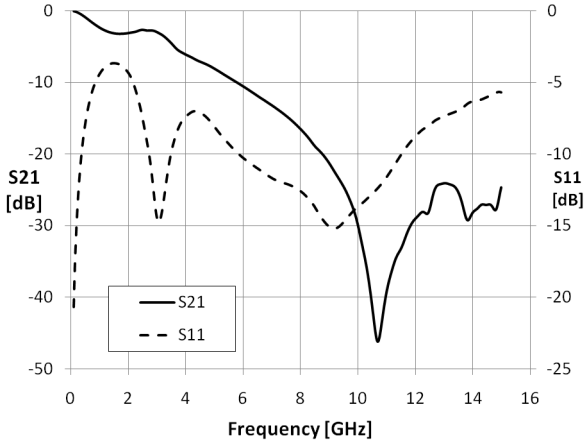

Figure 3. S_{21} and S_{11} for the pure dielectric structure

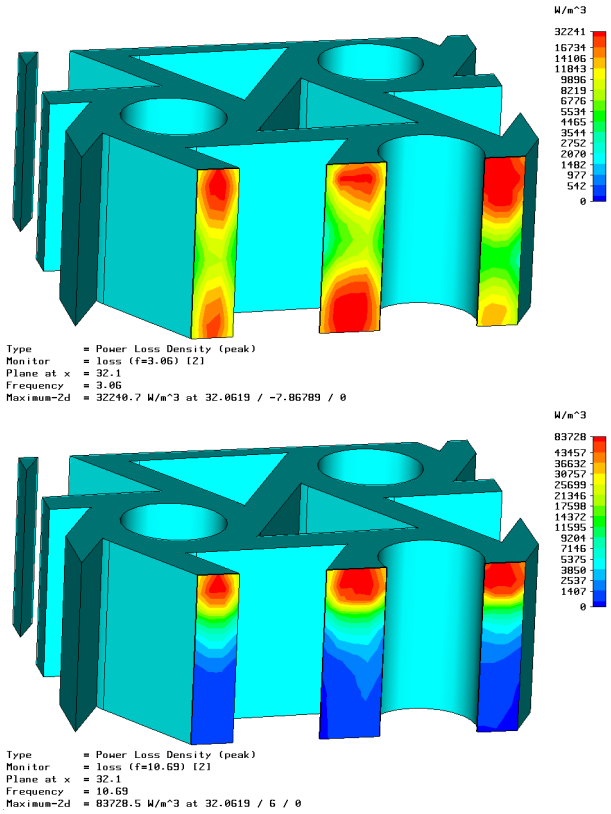

Figure 4. Power loss density inside the panel at 3.06GHz and 10.69GHz

The same software suite (CST Microwave Studio) described in section II was used, with the difference that in single frequency analysis the FDFD (Finite Differences in Frequency Domain) solver was used to compute the fields inside the structure. The computation is full 3D, and Fig. 4 shows the power loss density in the same longitudinal section through the panel at both frequencies considered.

The power loss distribution is mainly longitudinal (in the direction of the incident wave). The incident illumination is

320W/m^2 (normalization: 1W over the surface of the input port), a rather high value if we consider that the safety limit for RF workers is 50W/m^2. While such a situation is not usually encountered, we can use results in Fig. 4 to describe the energy dissipation process in relative units. At 3.06 GHz we have maximum $\Delta P_V \approx 20 \cdot 10^3$ W/m^3 inside the ligaments and $\Delta P_V \approx 32 \cdot 10^3$ W/m^3 inside the cylinder respectively. As the power losses are related to transmission behavior, we expect greater losses when the transmittance reaches a minimum (Fig. 3). At 10.69 GHz we have maximum $\Delta P_V \approx 53 \cdot 10^3$ W/m^3 inside the ligaments and $\Delta P_V \approx 95 \cdot 10^3$ W/m^3 inside the cylinder respectively.

While higher power loss density can be found inside the cylinder we can hardly say that the material concentrates the energy inside the cylinders. The energy gradient is visible rather in the longitudinal direction (normal to the panel) as it is the case with any dielectric panel subject to a plane wave incidence.

B. Metallized Structure

One of the objectives of the CHISMACOMB project [7] was to incorporate different applications, including electromagnetic shielding inside a mechanically superior panel. Fig. 1 shows a rather normal electromagnetic behavior, equivalent to a homogenous dielectric layer.

Better shielding performance can be obtained by metallization of the inner diameter of the cylinder. Thin (one tenth of the ligament thickness) aluminum foil has been deposited in two forms: a complete metallization (an aluminum tube inside the cylinder) and periodic, equally spaced metallic rings.

While the presence of the aluminum tubes has the expected effect of decrease of the transmittance, the use of the periodic rings offers supplemental longitudinal frequency selectivity. In Fig. 5, for 5 equally spaced rings, we witness a decrease with 15dB of S_{21} which corresponds with (2) to a 30dB decrease of the transmittance.

The height of the rings has no effect whatsoever on the transmission, while increasing the number of rings from 2 to 6 enlarges the stop band towards the lower frequencies.

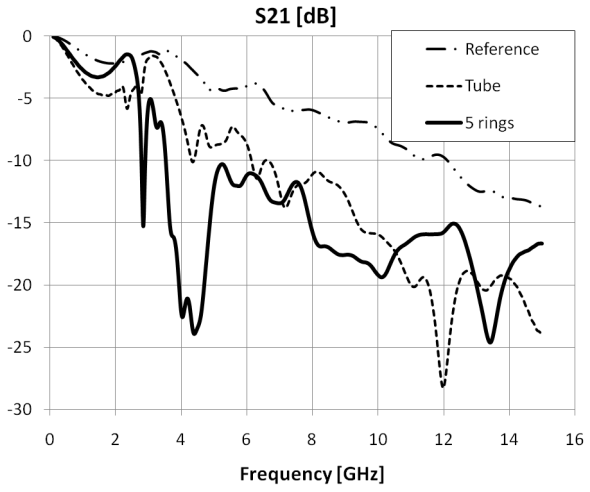

Figure 5. S_{21} and S_{11} for the metallized structure

We repeat the power loss density computation with a 5 equally spaced rings metallization of the inner cylinder, at 4GHz (in the middle of the stop band). Fig. 6 shows two interesting facts. First we find the expected increase of the losses, $\Delta P_V \approx 1.3 \cdot 10^6$ W/m^3 but further we witness a concentration of the energy dissipation around the metallic rings. Over the longitudinal gradient witnessed in Fig. 4 a transversal gradient around the rings is superposed.

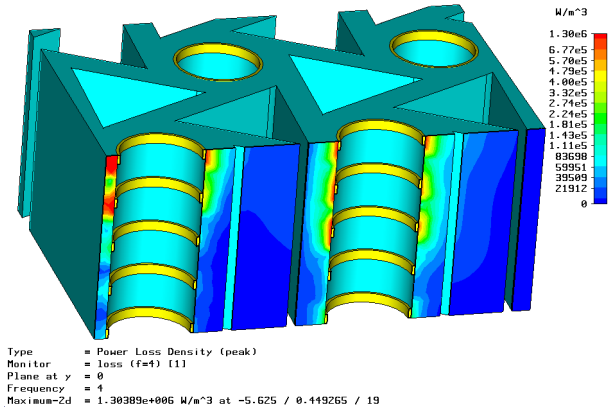

Figure 6. Power loss density inside the metallized panel at 4GHz

IV. CONCLUSIONS

The power loss density inside a hexachiral honeycomb panel has been computed with a pure dielectric structure and with different metallization on the inner diameter of the cylinder. Complete aluminum metallization of the inner cylinder diameter and deposition of periodic metallic rings have been considered.

The use of equally spaced, longitudinally placed, metallic rings offers an decrease of 40dB in transmittance (in rapport to the pure dielectric structure) in a 1GHz wide stop band making the panel useful in electromagnetic shielding applications. The technology for the exterior surface metallization of the sparse structures is not difficult to implement.

Control of the stop band can be achieved by the choice of the appropriate thickness of the panel combined with optimal "number of rings"/"distance between rings" adjustment.

Furthermore, the increased energy dissipation is concentrated around the aluminum rings, offering some "hot spots" in which the placement of an energy harvesting device is optimal. Such devices can be used to power intelligent sensors or other applications to be inserted in the intelligent materials.

ACKNOWLEDGMENT

The authors wish to acknowledge the importance of the cooperation with other members of the CHISMACOMB [7] EU FP6 research project.

REFERENCES

[1] Grima, J., Negative, negative and more negative: systems exhibiting negative Poisson's ratio, negative thermal expansion and/or negative compressibility, 4th International Workshop on Auxetics and Related Systems, Malta, 2007, pp. 8

[2] Li, L.W.; You D.; Leong M.S. and Yeo T.S., Electromagnetic scattering by multilayered chiral-media structures: a scattering-to-radiation transform, Journal of Electromagnetic Waves and Applications, Vol. 14, 401-404, 2000

[3] Ammari H.; Laouadi M. and J.-C. Nedelec, Low frequency behavior of solutions to electromagnetic scattering problems in chiral media, SIAM Journal. of Applied. Math, Society for Industrial and Applied Mathematics, Vol. 58, No. 3, pp. 1022-1042, 1998

[4] Oussaid R. and Haraoubia B., Behavior of a chiral material in terms of a guided wave propagation, International Journal of Applied Electromagnetics and Mechanics, vol. 19 , 2004, pp. 631-635

[5] Bornengo D.; Scarpa F. and Remillat C., Evaluation of hexagonal chiral structure for morphing airfoil concept, Proceedings. IMechE Vol. 219 Part G: J. Aerospace Engineering, pp. 185-192, 2005

[6] Khany I.A.; Raghavendray S.C.and Kulkarni A.B., Polyester-based chiral materials for microwave absorption applications, International Journal of. Electronics, 2003, Vol. 90, No. 3, 159-166

[7] CHISMACOMB, A FP6 Specific Target Research Project, FP6-EU-013641, http://www.chismacomb.eu/.

[8] CST GmbH, Application Note, Photonic Crystal Simulation, Article ID: 296, 2007 - http://www.cst.com

[9] CST of America, A Software Suite with Total Synergy, Microwave Journal, Vol. 49, No. 1, 2006

[10] Damian R.F., Ciobanu R., Brînzila M. and Olariu M., Stability considerations and efficient computing in chiral materials electromagnetic simulations, 15th IMEKO TC4 Symposium on Novelties in Electrical Measurements and Instrumentation, Iasi, Romania, 19-21 sept. 2007, pp. 110-114

[11] Hong Y. K.; Lee C. Y., Jeong C. K.; Lee D. E.; Kim K. and Joo J., Method and apparatus to measure electromagnetic interference shielding efficiency and its shielding characteristics in broadband frequency ranges, Review of Scientific Instruments, Volume 74, Issue 2, February 2003, pp. 1098-1102

Thermal effects of electromagnetic energy concentration inside metallic and dielectric structures

Romeo Ciobanu[1], Radu Damian[1*] and Cristina Schreiner[1]
[1] Technical University Iasi, Romania
*E-mail: rdamian@etti.tuiasi.ro

Abstract— **Structures with dielectric/metallic composition submitted to the influence of external or internal electromagnetic fields have the tendency to concentrate the electromagnetic energy, subject to their specific structure. While this phenomena can be generally neglected, when electromagnetic energy reaches high levels (as in the case of the proposed Wireless Power Transmission which can reach an illumination of up to 30 ÷ 90 kW/m^2 at the space reflectors) the corresponding heating effect associated with electromagnetic energy dissipation inside complex structures can lead to inhomogeneous thermal pattern. This situation can in turn lead to mechanical stress and failure in dielectric structures or acceleration of aging mechanisms.**

Keywords -- metamaterials, chiral, honeycomb, thermal analysis, energy concentration

I. INTRODUCTION

In the past years, an increasing amount of effort has been invested in the development of new materials, with good mechanical properties, low weight and low cost. In particular auxetic materials benefit from their negative Poisson's ratio [1] and are investigated closely in the last decade [2], [3], [4].
Microwave shielding structures can be used in energy harvesting applications. Usually a shield will consume and concentrate the energy dissipation inside his structure. Energy distribution can be sometimes controlled in a certain manner, and eventual detectors or "energy harvesters" can be placed in optimum locations with higher energy concentration. Even in the absence of the shielding properties, certain structures can be used only to rise the energy level in some points, where is needed.

II. LOCALIZED THERMAL EFFECT OF MICROWAVE ENERGY DISSIPATION

One of the important proprieties of the auxetic materials is the thermal expansion, desired to be zero or negative. In thermal expansion studies the main assumption is a homogenous increase in temperature in the entire volume of the material. In the microwave shielding applications, where high absorption of the electro-magnetic energy is desired, we may find ourselves in a certain situation where high power level waves interact rapidly with the structure. The hexachiral honeycomb interacts at microscopic level with the incident electromagnetic waves; as a result the power dissipation is not equally distributed inside the structure. One of advantages of these metamaterials in microwave shielding is their intrinsic sparse nature, giving them good heat dissipation properties but thermal phenomena are slow comparing to the electromagnetic interaction that generates them, so we can expect temporary and localized temperature increase.
The electromagnetic energy dissipation inside the structure can be expressed locally in an elementary volume, in terms of the power loss density $P_V=dP/dV$ in (1). In the same elementary volume, this energy dissipation will generate an increase in temperature (2). In these relations we use the parameters for Epoxy fiberglass which is the base material for the panel under test: density $\rho \approx 1800$ kg/m^3, and specific heat capacity $c_p \approx 1255$ J/kg·K
A concentration of the energy dissipation will generate a temperature increase in certain points. However this energy is not accumulated, the most significant heat transfer mechanism being thermal conduction (3). The speed of the heat transfer through a portion of material of transversal area A and length x depends on the steady state temperature difference. Again, the material data is for Epoxy fiberglass, the thermal conductivity in (3): $k \approx 0.29$ W/m·K.

$$dQ = \left(\frac{dP}{dV}\right)\cdot dV \cdot dt = P_V \cdot dV \cdot dt \tag{1}$$

$$dQ = dm \cdot c_p \cdot dT = \rho \cdot dV \cdot c_p \cdot dT \tag{2}$$

$$\frac{dQ}{dt} = k \cdot A \cdot \frac{\Delta T_0}{x} \tag{3}$$

Heat is generated differently in two points according to the electromagnetic energy concentration pattern (1). We can estimate the steady state for the thermal phenomenon when the difference between the generated heat in every point equals the heat transferred by conduction between the same points (4)-(5).

$$\Delta\left(\frac{dQ}{dt}\right) = \left.\frac{dQ}{dt}\right|_1 - \left.\frac{dQ}{dt}\right|_2 = \Delta P_V \cdot dV \tag{4}$$

$$\left.\frac{dQ}{dt}\right|_{1-2} = k \cdot A \cdot \frac{\Delta T}{x} \tag{5}$$

While accurate description of the thermal conductivity in the presence of inhomogeneous power dissipation would require integration of (2) and (3) in the entire structure and is beyond the scope of this paper, we can make an estimate (6) of the thermal effects, considering the situation were the thermal

conductivity and power dissipation occur in the same elementary volume, a cubic shape with edge x.
Typically, in microwave illuminated structures, the distances are in the centimeter range, so we can take $x = 10^{-2}$ m in (6) as most appropriate for the structure under test and the frequency range of interest. Field strength distributions inside the structure are found to behave correspondingly (as a longitudinal concentration) and the transversal distribution will be imposed by the geometry of the structure, again in the centimeter range.

$$\Delta T \approx \frac{x^2}{k} \cdot \Delta P_V \tag{6}$$

$$\Delta T \approx 3.45 \cdot 10^{-4} \cdot \Delta P_V \left[\mathrm{W/m^3}\right] \quad [\mathrm{K}] \tag{7}$$

Equation (7) can be used to estimate, directly in Kelvin, the temperature gradient which will appear inside the hexachiral structure we investigate at normal electromagnetic illumination.

III. Computer Simulations

A. Full Wave electromagnetic analysis

The structure used in tests was a fiber reinforced polymer prototype, developed in the framework of the CHISMACOMB FP6 EU project [5] by the Italcompany (Fig. 1). The structure is a hexachiral honeycomb, each of the equally spaced cylinders being connected to his 6 neighbors by ligaments and is based on the idea found in [6] which is a simplification of a two-dimensional molecular model studied earlier [7].
The power loss density inside the ligaments of the hexachiral honeycomb is an indication of energy dissipation inside the structure. The base dielectric material used as the panel is characterized by $\varepsilon_r = 10$ and $\tan\delta = 0.1$. Further details about the structure, choice of parameters, simulation details can be found in [8].

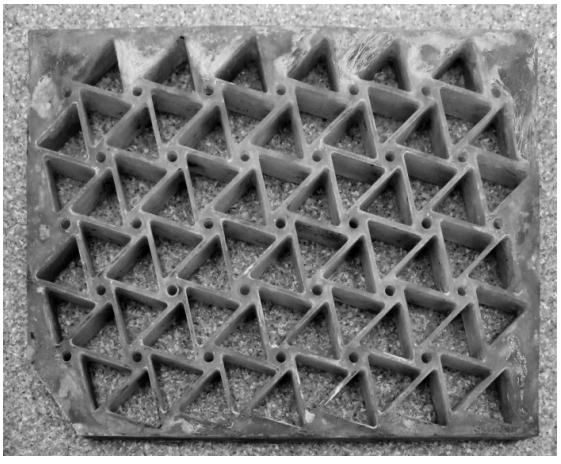

Figure 1. Hexachiral honeycomb

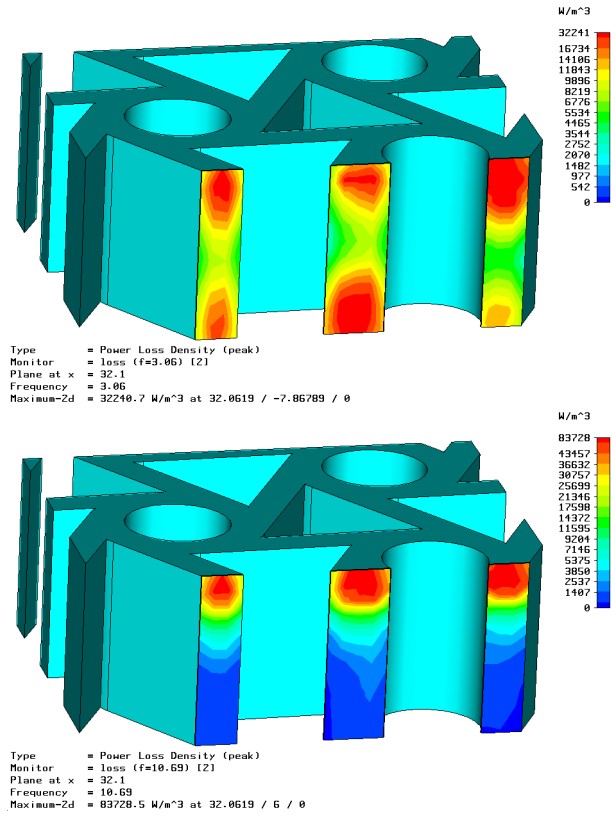

Figure 2. Power loss density inside the panel at 3.06GHz and 10.69GHz

At 3.06 GHz we have maximum $\Delta P_V \approx 20 \cdot 10^3$ W/m^3 inside the ligaments and $\Delta P_V \approx 32 \cdot 10^3$ W/m^3 inside the cylinder. We can use (7) to estimate the temperature gradient which will appear inside the hexachiral structure. The maximum temperature variation is $\Delta T \approx 7$ K and $\Delta T \approx 11$ K respectively.
As the power losses are related to transmission behavior, we expect greater losses when the transmittance reaches a minimum. At 10.69 GHz we have maximum $\Delta P_V \approx 53 \cdot 10^3$ W/m^3 inside the ligaments and $\Delta P_V \approx 95 \cdot 10^3$ W/m^3 inside the cylinder, the corresponding temperature variation being $\Delta T \approx$ 18 K and $\Delta T \approx 33$ K respectively.
While higher power loss density can be found inside the cylinder we can hardly say that the material concentrates the energy inside the cylinders. The energy gradient is visible rather in the longitudinal direction (normal to the panel) as it is the case with any dielectric panel subject to a plane wave incidence.
The incident illumination is 320W/m^2 (normalization: 1W over the surface of the input port), a rather high value if we consider that the safety limit for RF workers is 50W/m^2. While such a situation is not usually encountered, we can use results in Fig. 2 and the estimated temperatures (7) to describe the energy dissipation process relatively.

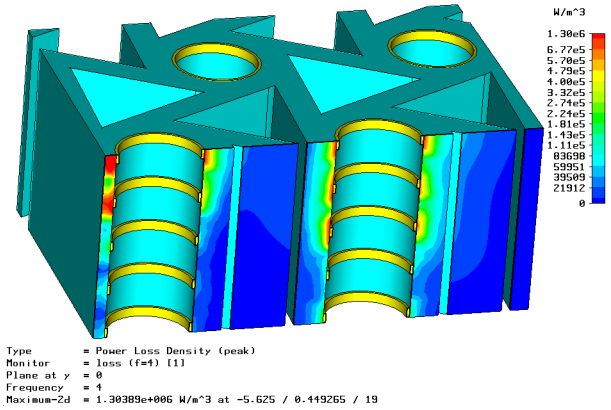

Figure 3. Power loss density inside the metallized panel at 4GHz

Better shielding performance can be obtained [8] by deposition of periodic, equally spaced metallic rings on the inner diameter of the cylinders. This offers supplemental longitudinal frequency selectivity. For 5 equally spaced rings, we witness a decrease with 15dB of S_{21} equivalent to a 30dB decrease of the transmittance.

We investigate the power loss density in this case, at 4GHz (in the middle of the stop band). We find an important increase of the peak power loss density, $\Delta P_V \approx 1.3 \cdot 10^6$ W/m^3 corresponding with (7) to a temperature gradient $\Delta T \approx 450$ K, high enough to impose thermal considerations in the design of such a panel. Also we witness the concentration of the energy dissipation around the metallic rings. Over the longitudinal gradient shown in Fig. 2 a transversal gradient around the rings is superposed.

B. Electromagnetic - Thermal Co-Simulation

The CST Design Environment offers a low frequency application beside Microwave Studio, which features a stationary thermal solver. The previous computed power loss density can be used directly by the thermal solver in EM Studio, providing the integration of (2) and (3) over the entire volume of the structure [9].

There are some advantages and disadvantages regarding this approach. First of all, with this solver we can take into account the reach of the thermal equilibrium, as the transfer of heat from the high power loss points to the lesser ones will level the expected temperature gradient. Also, some thermal transfer phenomena (as radiation and convection) are taken into account, this being especially important as the structure under test is a sparse one, and there will be a lot of air inside and around it.

The disadvantages are mainly related to the thermal boundary conditions. The 4 cylinders unit cell is the repetitive part in an infinite periodic structure. While the high frequency electromagnetic numerical recipes take into account the periodicity of the structure, in thermal computation we had to choose an open thermal boundary around the unit cell which will affect the accuracy of the computation on the edges.

Fig. 4 shows the temperature inside the Epoxy fiberglass panel, with $\Delta T \approx 12.8$ K and $\Delta T \approx 28.7$ K, in good agreement with the previously estimated values from (7).

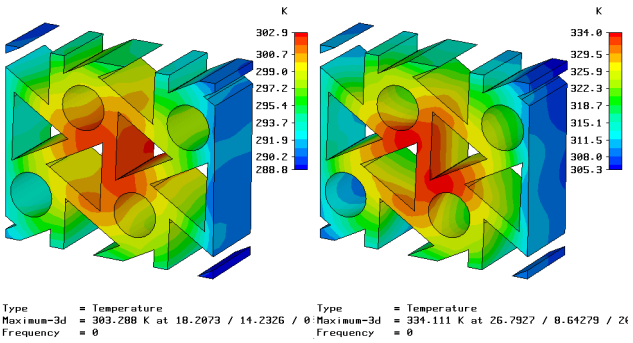

Figure 4. Temperature inside the panel at 3.06GHz and 10.69GHz

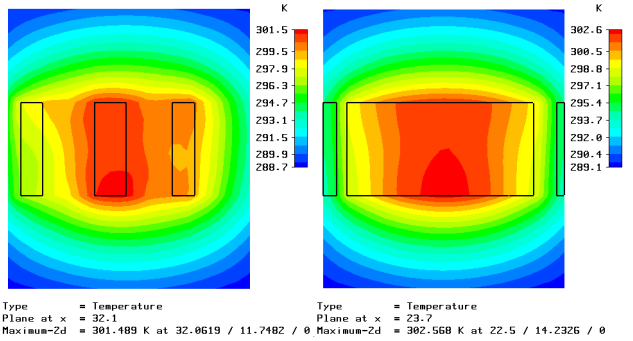

Figure 5. Temperature on the cylinder and ligament plane at 3.06GHz

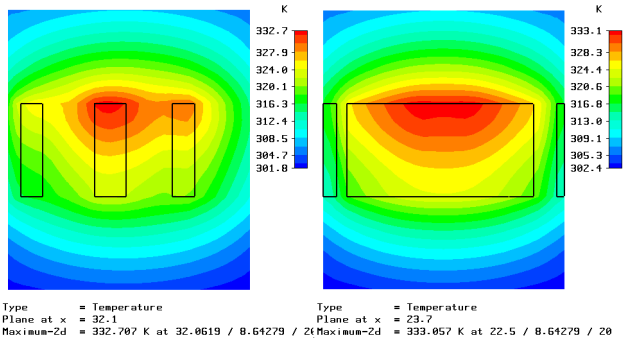

Figure 6. Temperature on the cylinder and ligament plane at 10.69GHz

The longitudinal temperature gradient is plotted in two planes, both normal to the panel, in Figs. 5 and 6. One of the planes passes through the axe of the cylinder (x=32.1 in Figs 5 and 6, exactly the same position as in Fig. 2) and the second, plotted on the right side of Figs 5,6, passes only through a ligament. The longitudinal gradient is preserved even if the lateral open thermal boundary condition lowers somehow the temperatures on the edges of the unit cell through thermal radiation.

A similar thermal analysis of the metallized panel offers a uniform temperature (not plotted) in place of the $\Delta T \approx 450$ K expected. This behavior comes from the extremely low energy dissipation, in average values, inside the panel. Fig. 7 shows the Thermal volume losses inside the pure dielectric/metallized panel and we find that the average losses are much lower (1.32 W/m^3 as opposed to $36 \cdot 10^3$ W/m^3 in the pure dielectric case). Also we can compute the total heat flow: $1.33 \cdot 10^{-7}$ W as opposed to $4.06 \cdot 10^{-1}$ W. The explanation is that the field energy is extremely concentrated in this case, with

very high peak power loss density in a very small volume around the metallic rings.

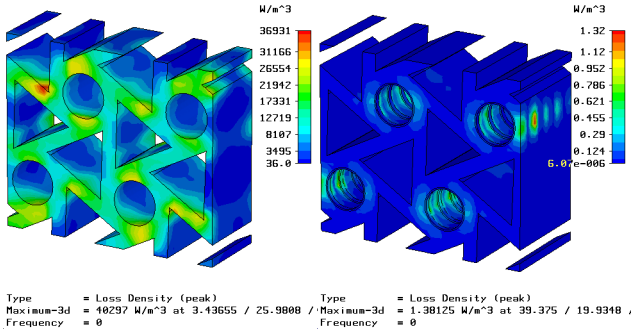

Figure 7. Thermal Volume Losses inside the pure dielectric and metallized panels

IV. CONCLUSIONS

We found relations for estimation of the temperature gradient if the power loss density can be found by full wave electromagnetic analysis. Equation (7) is plotted in Fig. 8 where we marked the positioning of the hexachiral panel we tested.

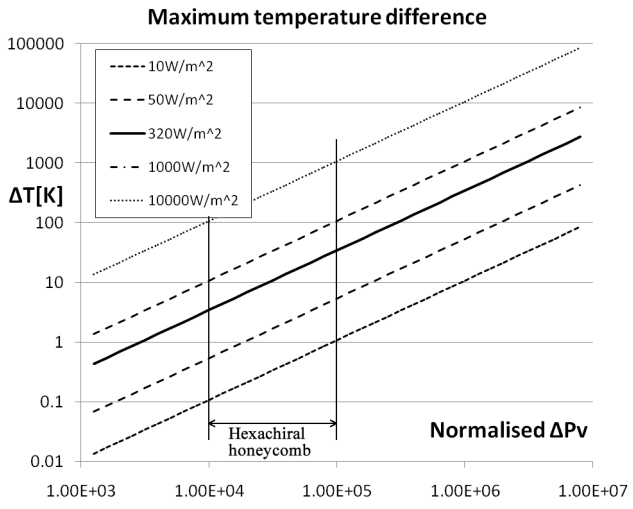

Figure 8. Dependence of the temperature gradient over the normalized power loss density

However, (7) and Fig. 8 apply only in the case of strictly dielectric structures, which rely on volume absorption of the microwave energy to implement shielding behavior. The presence of metallic insertions has been found to alter the electromagnetic fields distribution, leading to a high peak to average ratio of the power loss density and thus to a lower thermal effect, highly concentrated around the metallic insertions. Structural absorbents (Salisbury screen or Jauman layers) will offer this behavior, and generally all the electromagnetic shields which rely on destructive interference to achieve a decrease of the transmittance.

The simple hexachiral panel, subject to localized electromagnetic power dissipation develops thermal gradients which at high power levels can affect the mechanical performance of the material, thus thermal analysis in high power applications must rely on temperature gradient instead of thermal uniformity.

In typical applications (10 to 50 W/m^2 - safety limits) the effect is less important (up to 5K temperature differences) but the differences in temperature can reach 100K at 1kW/m^2 illumination (Fig. 8). Wireless Power Transmission can use up to 30 ÷ 90 kW/m^2 at the space reflectors.

The simple chiral structure as tested is not a particularly good absorbent. Better absorbents will retain more energy and thus the temperature gradient will be accentuated. However the structure has the effect of concentrating the electromagnetic energy, especially at certain frequencies, and this effect could be used in energy harvesting applications.

ACKNOWLEDGMENT

The authors wish to acknowledge the importance of the cooperation with other members of the CHISMACOMB [5] EU FP6 research project.

REFERENCES

[1] Grima, J., Negative, negative and more negative: systems exhibiting negative Poisson's ratio, negative thermal expansion and/or negative compressibility, 4th International Workshop on Auxetics and Related Systems, Malta, 2007, pp. 8

[2] Li, L.W.; You D.; Leong M.S. and Yeo T.S., Electromagnetic scattering by multilayered chiral-media structures: a scattering-to-radiation transform, Journal of Electromagnetic Waves and Applications, Vol. 14, 401-404, 2000

[3] Oussaid R.; Haraoubia B. 2004, Behavior of a chiral material in terms of a guided wave propagation", International Journal of Applied Electromagnetics and Mechanics, vol. 19 , 2004, 631-635

[4] Khany I.A.; Raghavendray S.C.and Kulkarni A.B., Polyester-based chiral materials for microwave absorption applications, International Journal of. Electronics, 2003, Vol. 90, No. 3, 159-166

[5] CHISMACOMB, A FP6 Specific Target Research Project, FP6-EU-013641, http://www.chismacomb.eu/.

[6] Prall D; Lakes RS. Properties of a chiral honeycomb with a poisson's ratio of - 1, Int. J. Mech. Sci. Vol. 39, No. 3, 305-314, 1997

[7] Wojciechowski K.W. Two-dimensional isotropic systems with a negative Poisson ratio, Physics Letters A137, 60-64 (1989)

[8] Romeo Ciobanu, Radu Damian and Cristina Schreiner, Electromagnetic energy harvesting by field concentration in intelligent materials, Conference Proceedings of CMD2010, in press

[9] CST GmbH, Application Note, Modeling Temperature Effects of RF Thermoablation in a Human Liver using the bioheat formulation in CST DE, Article ID: 387, 2009 - http://www.cst.com

Mechanics of Nano, Micro and Macro Composite Structures
Politecnico di Torino, 18-20 June 2012

A. J. M. Ferreira, E. Carrera (Editors)

http://paginas.fe.up.pt/~icnmmcs/

DIELECTRIC MEASUREMENTS AND ELECTROMAGNETIC SIMULATIONS OF MAGNETITE NANOFILLERS IN POLYMER MATRIX

Radu Damian[*], Romeo Ciobanu [†1] and Cristina Schreiner [†]

[*] Faculty of Electronics, Telecommunications and Information Technology (ETTI)
Technical University of Iasi
Bd. Carol I, 11, Iasi, Romania
e-mail: rdamian@etti.tuiasi.ro

[†] Faculty of Electrical Engineering and Industrial Informatics (EEII)
Technical University of Iasi
Bd. Dimitrie Mangeron, 21- 23, 700050, Iasi, Romania

[1] corresponding author: e-mail: rciobanu@yahoo.com

Key words: Composite structures, Electromagnetic Modeling, Thermal , Manufacturing.

Summary. *We measure the dielectric and structure properties of a polymer adhesive matrix with magnetite nanofiller. Experimental parameters are used in an electromagnetic-thermal co-simulation with application in high frequency welding applications.*

1 INTRODUCTION

For the adhesive matrix, information from suggested the use of the amorphous alfa grade polyolephinic (APAO) polymer. Dielectric properties have been measured using the Broadband Dielectric Spectrometer (Novocontrol GMBH) encompassing an Alpha frequency response analyzer and Quattro temperature controller, and have been used as so.

While it is easier in electromagnetic simulation software to work with volume ratio, manufacturing process relies on the mass ratio between the nanofiller and the adhesive matrix. In [1] the theoretical density of the nanofilled composite is calculated using equation (1). From (1) is easy to compute the volume ratio, when the mass ratio M is known (2)

$$\rho_T = (1-V)\cdot \rho_m + V\cdot \rho_f \tag{1}$$

$$V = \frac{M\cdot \rho_m}{(1-M)\cdot \rho_f + M\cdot \rho_m} \tag{2}$$

2 ELECTROMAGNETIC-THERMAL CO-SIMULATION

X ray SKYSCAN 1174 microtomograph investigation of the adhesive matrix with 8% nanofiller showed that the average particle diameter was 172μm while the average particle separation was 1093μm, the volume ratio imposed by these dimensions is V=1.64%. The

interaction between a plane wave and an infinitely large sheet of adhesive matrix with magnetite insertions (1.65% volume ratio) at normal incidence was investigated.

The power loss density inside the structure is an indication of energy dissipation. Analyses were performed at 100kHz, 1MHz and 10 MHz with the high frequency welding applications in mind.

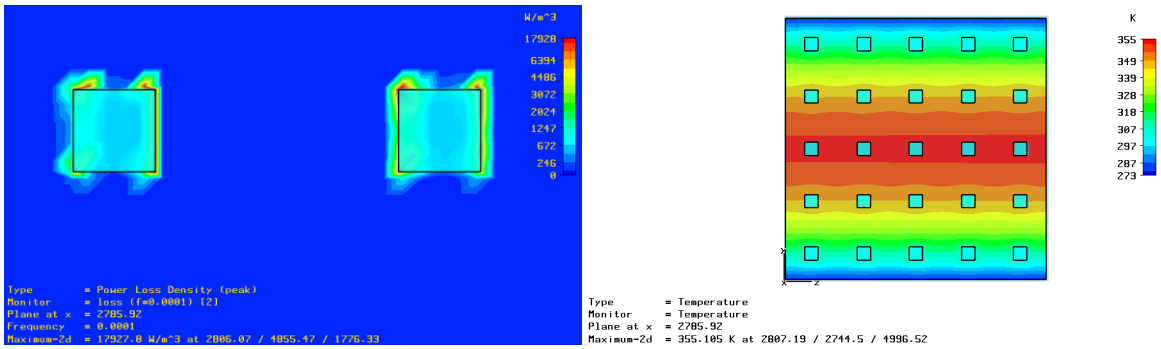

Figure 1: Power loss density inside the nanofilled adhesive matrix at 0.1MHz and Temperature distribution

The CST Design Environment offers a low frequency application beside Microwave Studio, which features a stationary thermal solver. The previous computed power loss density can be used directly by the thermal solver in EM Studio. Figure 1 shows that, while the energy is dissipated inside the magnetite insertions, it will generate increase in temperature mainly/similarly in the surrounding adhesive matrix, due to the increased thermal conductivity of the magnetite.

3 CONCLUSIONS

The power is almost entirely dissipated inside the magnetite nanofillers, with some peaks of dissipation in the vicinity of the insertions. The nanofillers act as an internal heat sources, imposing a uniformly spaced heat generators inside the adhesive matrix. This will allow reaching the critical melting temperature with lower power levels, preventing damage to the surrounding materials. Observing the 3D power loss density inside the insertions closer to the center of the structure we can observe that energy is mainly concentrated on the inner nanofillers, which also add to the protection offered to the surrounding materials. However for this protection to be effective, the material properties of the surrounding structures must be known, and some combinations of material properties might impose a different nanofiller/adhesive matrix combination.

REFERENCES

[1] L. Ramajo, A. Cristóbal, P. Botta, J. Porto López, M. Reboredo, M. Castro, ”Dielectric and magnetic response of Fe3O4/epoxy composites”, *Composites: Part A* 40 (2009) 388–393

INTERPRETAREA EVOLUŢIEI DATELOR STATISTICE CU IMPACT SOCIAL

Simona Irina Damian[1], Diana Mihai[1], Radu Florin Damian[2]

1. Universitatea de Medicină şi Farmacie "Gr. T. Popa", Iaşi

2. Universitatea Tehnică "Gh. Asachi" Iaşi

INVESTIGATION OF STATISTIC DATA EVOLUTION WITH SOCIAL IMPACT (Abstract) – Usually statistical analysis of medical and social data consists the final product of the research activity, the mean values, percentages, deviations etc. being an important information to share with other researchers. This paper shows the alternate possibility, using the statistical analysis to discover conclusions not so obvious from the available data. We use this method to analyze couples evolution towards marriage or towards divorce. Age influenced tendency is determined from official referendum and statistical data regarding both married and cohabiting couples. **Key Words**: STATISTIC EVOLUTION, MARRIAGE, DIVORCE.

INTRODUCERE

De multe ori prelucrarea statistică a datelor medicale şi/sau sociologice este folosită ca produs finit al activităţii de cercetare în domeniu. Desori concluziile lucrărilor ştiinţifice medico-sociale determină procentaje, valori medii, abateri maxime etc. ca rezultate finale, afirmaţii purtătoare de informaţii valoroase în domeniul medical. Această lucrare îşi propune să arate un mod alternativ de utilizare a prelucrărilor statistice şi anume ca material primar pentru obţinerea unor rezultate care nu sunt foarte evidente din datele disponibile.

Metoda prelucrărilor statistice este aplicată în acest caz analizei evoluţiei cuplurilor, pe grupe de vârstă, în Romania.

MATERIAL ŞI METODĂ

Se prezintă în tabelul I structura demografică a cuplurilor din România, rezultată în urma recensământului din anul 2002 [1]. În acest an, cu ocazia recensământului au fost contorizate cuplurile după starea civilă legală (cupluri soţ/soţie) şi de asemenea starea civilă de fapt (partener/parteneră), cupluri care trăiesc împreună fără a fi legal căsătoriţi. Date similare există şi pentru aceste cupluri dar nu sunt trecute aici din motive de spaţiu.

Tabelul I.
Cuplurile legale (soţ/soţie) în funcţie de grupele de vârstă (în anul 2002)

2002		Soţie									
		Sub 20 ani	20-24 ani	25-29 ani	30-34 ani	35-39 ani	40-44 ani	45-49 ani	50-54 ani	55-59 ani	60 ani +
Soţ	Sub 20 ani	2914	1003	138	38	12	10	0	0	0	0
	20-24 ani	20332	61672	14456	1619	188	74	24	3	3	3
	25-29 ani	16159	160161	192497	30651	1993	415	125	114	9	1
	30-34 ani	3007	55991	264542	319937	27071	3557	749	245	81	12
	35-39 ani	341	6478	46656	242593	131356	18220	2844	599	131	99
	40-44 ani	76	1557	10814	97781	217023	193246	30008	4268	655	397
	45-49 ani	9	367	2495	19351	67767	268257	230286	29054	3226	1182
	50-54 ani	1	68	537	3457	9668	66677	270374	187819	19073	4646
	55-59 ani	3	22	87	697	1565	8310	65446	210921	104719	23940
	60 ani +	0	15	63	192	599	2708	14926	101849	249881	1019589

O reprezentare a acestor date (în figurile 1 şi 2) arată o distribuţie normală în funcţie de vârstă a cuplurilor existente [2] şi anume preferinţa statistică pentru cuplurile apropiate ca vârstă, în care vârsta bărbatului este mai mare decât cea a femeii cu aproximativ 5 ani (aproximaţia provenind din faptul ca vârsta este indicată prin intervale de câte 5 ani).

La nivelul cuplurilor căsătorite există un vârf foarte pronunţat (1019589 căsnicii) pentru perechile în vârstă de peste 60 de ani, în parte datorită îmbătrânirii populaţiei, în parte datorită faptului că acest interval este cel mai întins. Cuplurile caracterizate de diferenţe mari de vârstă între cei doi parteneri (”60 ani şi peste”/”Sub 20 ani”) sunt practic inexistente.

Distribuţia cuplurilor de parteneri (concubini) este asemănătoare, numărul lor fiind redus, un maxim mai pronunţat existând în zona 20-39 ani la bărbaţi şi 15-35 ani la femei, reprezentând intr-un fel „reticenţa” cuplurilor tinere de a-si legaliza o legătură stabilă.

Se reprezintă în figura 3 raportul între numărul de cupluri de fapt (parteneri) şi cele legale (soţi). Acest raport arată preferinţa cuplurilor de o anumită structură a vârstelor de a aprecia concubinajul ca stare socială faţa de căsătorie. Şi în acest caz rezultatele sunt cele aşteptate, cuplurile care se înscriu în diferenţa de vârstă de 1-10 ani între bărbat şi femeie preferând legalizarea situaţiei (raport minim, sub 0,1 peste 25-30 de ani) deci mai puţin de 10% din cupluri aleg concubinajul. Cuplurile cu diferenţă mare de vârstă preferă de asemenea în mod clar (raport supraunitar) cuplurile de concubini întâlnite în majoritatea cazurilor. Un minim local neaşteptat se întâlneşte la cuplurile „bărbat

25-29 ani"/„femeie 50-54 ani" situaţie care nu corespunde cu tendinţa grupelor de vârstă apropiate. Acest lucru ar putea fi atribuit numărului redus de cupluri aflate în această situaţie, deci a erorilor relativ mari generate.

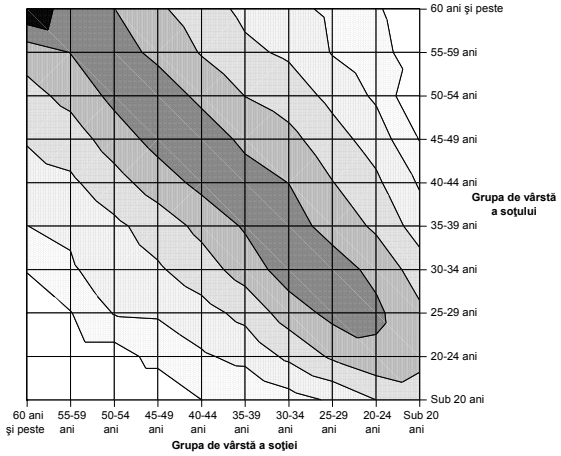

Fig. 1. Distribuţia cuplurilor soţ/soţie în funcţie de vârstă

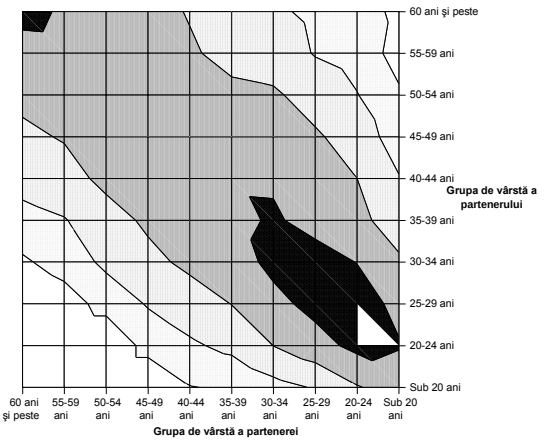

Fig. 2. Distribuţia cuplurilor partener/parteneră în funcţie de vârstă

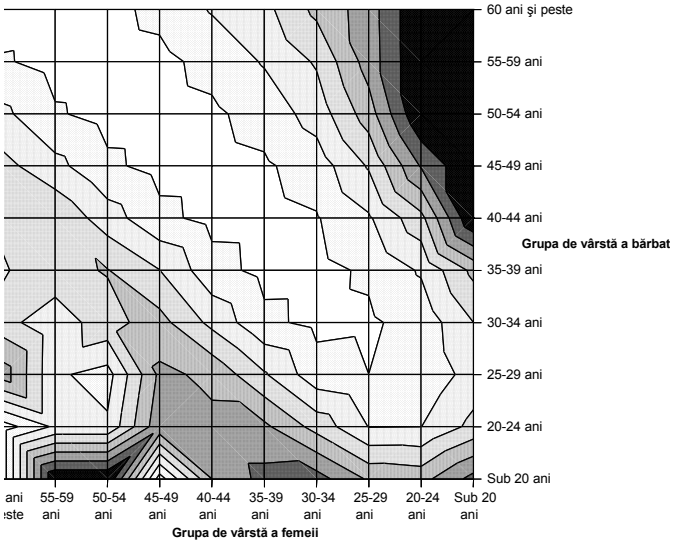

Fig. 3. Raportul între cuplurile de fapt şi cele legale în funcţie de vârstă

REZULTATE

Mişcarea naturală a populaţiei poate fi analizată în cadrul aceloraşi grupe de vârstă. Analiza evoluţiei cuplurilor poate fi estimată conform datelor referitoare la căsătoriile şi divorţurile din anul 2003, date cuprinse în Anuarul Statistic al României din anul 2004 [3] - sursa: Institutul Naţional de Statistică al României). Din nou din motive de spaţiu datele corespunzătoare divorţurilor nu sunt prezentate aici dar sunt public accesibile (http://www.insse.ro)

Tabelul II.
Căsătorii în anul 2003 în funcţie de grupele de vârstă

2003		Soţie									
		Sub 20 ani	20-24 ani	25-29 ani	30-34 ani	35-39 ani	40-44 ani	45-49 ani	50-54 ani	55-59 ani	60 ani +
Soţ	Sub 20 ani	946	465	69	21	8	4	1	1	0	0
	20-24 ani	10835	20370	4683	473	101	22	5	4	2	0
	25-29 ani	7204	24759	17718	2678	507	95	27	7	2	0
	30-34 ani	1216	5623	8174	4615	1216	218	77	10	2	1
	35-39 ani	166	1179	2596	2770	1473	351	116	23	11	2
	40-44 ani	61	293	709	1196	1136	684	286	89	11	2
	45-49 ani	13	145	316	590	657	723	637	212	48	10
	50-54 ani	14	52	120	236	285	396	670	389	103	25
	55-59 ani	2	16	41	64	79	142	286	330	131	49
	60 ani +	3	11	34	42	61	110	226	377	317	678

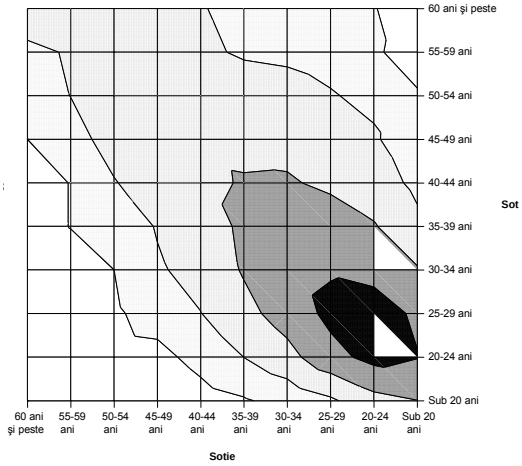

Fig. 4. Distribuţia căsătoriilor în 2003 în funcţie de vârstă

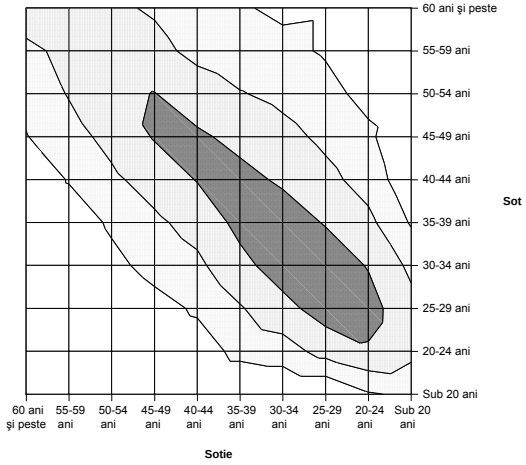

Fig. 5. Distribuţia divorţurilor în 2003 în funcţie de vârstă

Reprezentarea grafică din figurile 4-5 arată că şi căsătoriile şi divorţurile respectă tendinţa prezentă la cuplurile existente: diferenţă între 1 şi 10 ani între soţ şi soţie. Din cauza structurii demografice a cuplurilor (tabelul I) cele mai multe divorţuri (valorile absolute) respectă aceeaşi distribuţie în funcţie de vârstă. Maximul incidenţei căsătoriilor se întâlneşte în grupa de vârstă „bărbat 25-29 ani”/„femeie 20-24 ani” iar în cazul divorţului incidenţa maximă s-a întâlnit în grupa de vârstă „bărbat 30-34 ani”/„femeie 25-29 ani” în 2003.

În figura 6 se reprezintă tendinţa de evoluţie spre divorţ a cuplurilor legale calculată ca raport între numărul de divorţuri consemnate în 2003 şi număr de cupluri existente în 2002, în aceeaşi grupă de vârstă, valoarea obţinută fiind caracteristică pentru stabilitatea cuplurilor existente.

Se observă de asemenea o probabilitate ridicată de apariţie a divorţului în cuplurile

cu diferenţă mare de vârstă între soţi. Un alt fapt important este că probabilitatea divorţului scade pe măsura înaintării în vârstă a cuplurilor, posibil datorită apariţiei obişnuinţei sau datorită apariţiei copiilor. Spre 50-60 ani incidenţa divorţurilor scade de până la 10 ori.

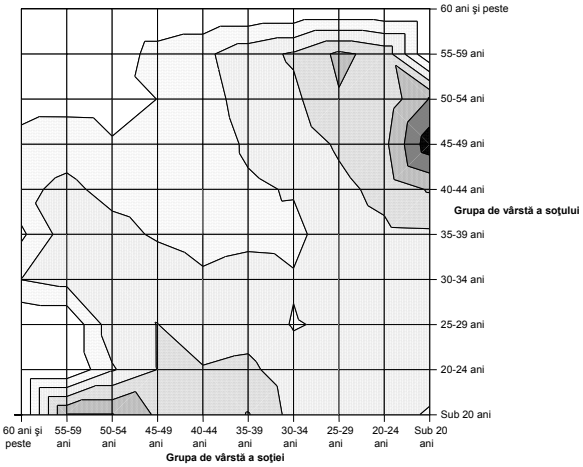

Fig. 6. Distribuţia raportului divorţuri(2003)/cupluri legale(2002)

Valorile obţinute sugerează o „viteză” mai mare de transformare a cuplurilor de fapt în căsătorii în cazul bărbaţilor tineri (20-25 de ani) cu un maxim în cazul cuplurilor realizate cu femei în vârstă de 50-54 de ani. Într-o măsură mai mică, dar tot cu „viteză” crescută, se oficializează şi cuplurile bărbaţi în vârstă cu femei foarte tinere (până în 24 de ani). Variaţia din figura 7. sugerează o evoluţie mai lentă a cuplurilor de fapt spre căsnicii în cazul partenerilor de vârste apropiate (cu excepţia celor foarte tineri: 20-29 ani).

Un rezultant interesant este de asemenea faptul că evoluţia spre căsătorie

În figura 7 este reprezentat raportul între numărul de căsătorii consemnate în 2003 şi numărul de cupluri de fapt existente în 2002, în aceeaşi grupă de vârstă. În condiţiile generalizării „căsătoriei de probă” aceste valori pot estima probabilitatea evoluţiei concubinajului spre căsătoria legală.

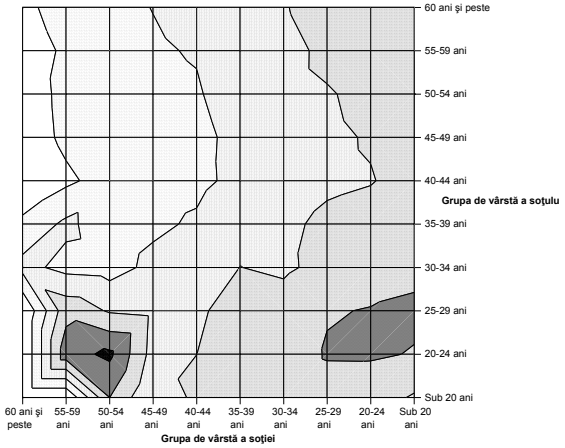

Fig. 7. Distribuţia raportului căsătorii(2003)/cupluri de fapt(2002)

depinde preponderent de vârsta femeii (ca factor determinant) şi mai puţin de cea a bărbatului.

CONCLUZII

Uneori rezultatele numerice sunt evidente şi aşteptate, alteori atrag atenţia asupra unor tendinţe sociale care scapă la prima vedere. Distribuţia cuplurilor existente în funcţie de vârstă respectă configuraţia tradiţională [2] (vârsta soţului cu 4-5 ani mai mare decât a soţiei în căsătorie, sau a bărbatului cu 1-10 ani mai mare decât a femeii în cuplurile de parteneri).

În schimb analiza dinamicii cuplurilor, ca evoluţie spre divorţ sau căsătorie, arată nişte lucruri neaşteptate. Cu toate că în valori absolute căsătoriile şi divorţurile respectă aceleaşi structuri din punctul de vedere al vârstei partenerilor implicaţi, tendinţele procentuale, deci într-o oarecare măsură viteza de evoluţie, sunt mai mari la cuplurile cu diferenţă mare de vârstă. Dacă se cunoştea instabilitatea cuplurilor căsătorite, se pare că şi reversul este adevărat, şi anume cuplurile echivalente de parteneri evoluează mai repede spre căsătorie.

O altă observaţie interesantă este că în timp ce divorţul poate fi atribuit în egală măsură partenerilor (simetrie aproximativ diagonală), tendinţa spre căsătorie este proprie în general femeii: raportul din figura 7 depinde în general de vârsta femeii şi mai puţin de cea a bărbatului (excepţia fiind cazul bărbaţilor tineri până în 25 de ani).

BIBLIOGRAFIE

[1] Institutul Naţional de Statistică al României - *Recensământul Populaţiei şi al Locuinţelor*, 2002

[2] Bestard-Camps J. *Marriage* în Smelser N.J., Baltes P.B. *International Encyclopedia of the Social & Behavioral Sciences*, Ed. Elsevier, Berlin, ISBN: 0-08-043076-7, pp. 9258-9261.

[3] Institutul Naţional de Statistică al României - *Anuarul Statistic al României* din anul 2004